ULTRAFAST OPTICAL STUDIES OF PHONON POLARITONS, SQUEEZED MODES AND HIGH FREQUENCY DIAMAGNETISM IN METAMATERIALS

by

Andrea Bianchini

A dissertation submitted in partial fulfillment
of the requirements for the degree of
Doctor of Philosophy
(Applied Physics)
in The University of Michigan
2012

Doctoral Committee:

Professor Roberto D. Merlin, Chair
Professor Leonard M. Sander
Professor Herbert G. Winful
Assistant Professor Jennifer P. Ogilvie

The mermaids were fascinating and demonic inhabitants of an island to the West of the Great Sea. Half women and half birds, they were said to seduce, by the irresistible charm of their voice, the sailors who navigated those sea straits, all of whom perished, crushed against the rocks.

Ulysses, on his journey home, plugged his companions ears with wax to prevent them from hearing and being overwhelmed by the mermaids song. As for himself, he commanded that he be securely tied to the mainmast so he could hear their voices without undergoing the deadly consequences.

Orpheus instead sang a poem so soothing that it enchanted the mermaids and left them amazed, and silent.

(Silvano Fausti)

Al Professor Mauro Lasagna

che piú di ogni altro mi ha insegnato ad amare il sapere.

ACKNOWLEDGEMENTS

At the end of my PhD journey I feel profoundly indebted to a lot of people that have helped me along the way. I am certainly grateful to my advisor Prof. Roberto Merlin who trusted me to join his group despite my somehow "atypical" background. His deep understanding of condensed matter physics and his experimental competence were pivotal in my research endeavor. Roberto has always been very understanding and available to discuss with me any matter, scientific and not. I would also like to thank Prof. Duncan Steel who stirred my interest in Quantum Mechanics and strongly supported me during my transition from Engineering to Physics. A special mention goes to the members of my defense committee: Prof. Sander who provided much guidance especially at the beginning of my PhD, Prof. Ogilvie who let me use her kHz amplifier for a few months and Prof. Winful. I cannot forget Prof. James Liu who taught me Classical Electrodynamics I and II (i.e. Jackson): his competence, commitment and great skills were always very inspiring.

I would like to express my gratitude to many friends and colleagues who supported me in different circumstances. Jingjing Li has been my labmate for my entire PhD duration and has greeted me with a smile every morning throughout the years. She has always preceded me in both the two research groups I have worked in providing much help through her expertise and experimental skills. Brendan O'Connor has also been a good friend and I have really enjoyed hanging out with him. Jessica Ames has been an invaluable companion in my daily struggles against unstable lasers, malfunctioning chillers, faulty translation stages, temperature and humidity drifts. I like to believe that, in the end, we won. She has always been willing to lend a hand, taught me how to operate the OPA, and, especially, has made sure that my sometimes reckless attitude to deal with problems did not result in any major damage. I would like to thank Alex Toulouse for helping me with

the GaSe samples' preparation, the fun time at the gym, his constant concern to improve my English vocabulary and, not last, his assistance in the formulation of the canonical approach. I am also grateful to all my other labmates: Paul Jacobs, Ilya Vugmeyster, Prashant Padmanabham, Steve Young, Ibrahim Boulares, Ben Isaacoff and Greg Affeldt. I am indebted to students from other groups as well: Franklin Fuller, Vladimir Stoica who shared with me his vast knowledge of experimental techniques, Vladka Tomeckova and Scott Rudolph with whom I collaborated on the spherical particle project. I am especially thankful to Vladka and her family for their friendship. I think I owe a big thanks to both Steve Katnik who took care of our lasers and taught me how to align them and Julian Broad who trained me to work in the machine shop.

Many other people outside the Physics Department accompanied me throughout these years and deserve to be acknowledged. Francesco Andriulli has been a good friend and has always advised me wisely both on science and private matters. Thanks to Teresa Murano and Dave Anderson for their great generosity and for reminding me that Italians are strong people. I really enjoyed the interesting conversations about physics, life and much more with Lei Jiang. I deeply appreciate all the support received from Saint Mary's staff, especially Fr Thomas McClain and Fr Dennis Dillon. I would also like to thank Don and Marylou Murray and their entire family for their hospitality and all the Thanksgiving and Christmas spent together. Many other friends made me feel more at home in Ann Arbor, among them I should mention: Giovanna Paolone, Mariella Mecozzi and Gastón Tudury, who also helped me read proving this dissertation, Silvia Giorgini and Fabio Albano.

A very special thanks deserves Sarah Szymanski for helping me since the very beginning of this PhD enterprise, for cheering me up when I felt discouraged and especially for teaching me to never give up. The last mention goes to my family, my parents, Amleto and Marisa, and my sisters, Anna and Chiara. Their constant trust in me has always been a tremendous source of motivation and strength.

TABLE OF CONTENTS

LIST OF FIGURES

Figure

LIST OF TABLES

Table

CHAPTER I

Introduction

The work presented in this dissertation is composed of three separate and rather independent sections: the first one dealing with phonon polariton and plasmon phonon coupled modes in semiconductors; the second one discussing a novel phenomenon occurring when squeezed phonon states are excited; and the last one focused on the study and development of high frequency diamagnetic materials.

Spontaneous Raman scattering and impulsive stimulated Raman scattering (ISRS) have been extensively employed to study phonon modes in a wide variety of materials. For some time it was thought that coherent phonons in absorptive materials were excited through a mechanism (DECP) different than stimulated Raman scattering [1]. Stevens et al. [2] were able to prove that, in both transparent and opaque materials, the generation mechanism is ISRS. Particularly, by introducing two distinct Raman tensors (Chap. II), one for generation and one for detection, they showed that the scattering intensities extracted from frequency domain and time domain experiments were the same. More recently, the two Raman tensor theory was expanded to account for the fact that in absorptive materials the force driving coherent phonons is no longer impulsive but rather exponentially decaying with a decay rate Γ_R [3]. Up to this point, the theoretical predictions have been exclusively validated on absorptive materials (mainly semi metals). The experiments described in the first part of this dissertation were aimed to explore both the transparent and the opaque regime in the same material (a semiconductor with the gap in the visible range). In addition to that, the theoretical model was tested on vibrational modes of different symmetry (A and E) and polarization (TO and LO). The experimental measurements displayed several anomalies,

namely inconsistencies both in spontaneous Raman and ISRS when varying the excitation wavelength or measuring longitudinal phonons. To make sense of the new data, another aspect needed to be considered: the interaction of the electromagnetic field with polar lattice vibrations and free carriers. In Chap. IV the new observed features were interpreted within the framework of phonon polaritons and plasmon phonon modes. In particular, it was shown that, when the hybrid nature of a polariton mode is taken into account, the new results were still consistent with the ISRS and two Raman tensor theory.

Squeezed phonon states are introduced in Chap. V, highlighting similarities and differences with coherent phonon modes. The chapter focuses primarily on a novel phenomenon associated with squeezed phonon modes and named "phonon echo". Both a classical and quantum mechanical analysis revealed that when a squeezed phonon state is excited in a double pump experiment a new oscillatory signal arises at twice the time delay between the pump beams. It should be noted that this novel phenomenon takes place in a harmonic system, as opposed to the photon or spin echo case. Numerical simulations were provided to confirm the validity of the theoretical predictions. The feasibility of experimental measurements aimed at detecting the echoes is discussed at the end of the chapter.

The search for negative refraction and the recent developments in the metamaterial field have motivated the interest in high frequency diamagnetism, discussed in Chap. VI. Natural materials exhibit extremely weak diamagnetic character: the highest magnetic susceptibility is $\chi \simeq 10^{-4}$ (SI units) [4]. Following the work of Lewin [5], the magnetic properties of a particular structure, a matrix of spherical particles embedded in a host material, were investigated theoretically. Numerical simulations carried out on this particular structure predicted an enhanced diamagnetic character around 10GHz. Samples made up of different size copper spheres were built and measured in the microwave range using a Gaussian beam telescope. The extracted effective parameters confirmed the theoretical estimates. The novel metamaterial featured a magnetic susceptibility ($\chi \simeq 0.5$) three orders of magnitude higher than any natural material and fairly constant in the $\simeq$ 4GHz measured range.

CHAPTER II

Spontaneous and Impulsive Stimulated Raman Scattering by Lattice Vibrations

The first part of this dissertation is entirely devoted to the study of lattice vibrations and, in particular, of their interaction with coherent light. The intent of this chapter is to remind the reader of the necessary theoretical background needed to interpret the experimental results and appreciate the significance of the conclusions reached thereafter, especially in Chap. III.

Sec. 2.1 provides a rigorous review of the theory of lattice vibrations: the initial approach, based on classical mechanics, is successively developed into a fully quantum mechanical treatment of the subject. Particular attention is paid to identifying the normal modes of vibration and to show their connection with the relevant physical quantities such as energy and momentum. The phonon-photon interaction is discussed in Sec. 2.2 and employed to introduce spontaneous Raman scattering. The theoretical analysis is accompanied by a description of the experimental details of Raman experiments, i.e. scattering cross section and detection geometry. The last part of the chapter, Sec. 2.3, addresses the broad topic of coherent phonons and Impulsive Stimulated Raman Scattering (ISRS): the generation and detection processes are examined in the case of both transparent and opaque materials. The section is concluded by a short mention of the two-Raman tensor theory [2] and its implications for pump probe experiments.

2.1 Lattice Vibrations

The usual physical setting to properly describe lattice vibrations is a crystal of volume V with r atoms per unit cell, spanned by lattice vectors $\mathbf{a_n}$. Since the atoms can depart from their equilibrium sites, it is customary to indicate by $\mathbf{u}_{\mathbf{n},j}$ the displacement of the j^{th} ion in the $\mathbf{n}$ unit cell from its rest position. If the potential energy of the lattice at equilibrium is U_0, the change in energy due to the ions' movement can be Taylor-expanded in the following way:

$$U - U_0 = \sum_{j,j'} \sum_{\mathbf{n},\mathbf{n'}} \frac{1}{2} \mathbf{A}_{j,\mathbf{n};j',\mathbf{n'}} \mathbf{u}_{\mathbf{n},j} \mathbf{u}_{\mathbf{n'},j'} + \sum_{j,j',j''} \sum_{\mathbf{n},\mathbf{n'},\mathbf{n''}} \frac{1}{6} \mathbf{B}_{j,\mathbf{n};j',\mathbf{n'};j'',\mathbf{n''}} \mathbf{u}_{\mathbf{n},j} \mathbf{u}_{\mathbf{n'},j'} \mathbf{u}_{\mathbf{n''},j''} + ... \tag{2.1}$$

As expected, the linear term in the Taylor expansion, $\propto \mathbf{u}_{j,\mathbf{n}}$, is missing because the equilibrium state is an energy minimum. Since the energy of the crystal does not vary due to a rigid translation of all the atoms, the $\mathbf{A}$ tensor must depend only on $\mathbf{a_n} - \mathbf{a_{n'}}$ and not on $\mathbf{a_n}$ and $\mathbf{a_{n'}}$ separately. The equation of motion for $\mathbf{u}_{\mathbf{n},j}$ can be deduced using standard classical mechanics procedures [6]:

$$M_j \ddot{\mathbf{u}}_{j,\mathbf{n}} = - \sum_{j'} \sum_{\mathbf{n'}} \mathbf{A}_{j,j'}(\mathbf{a_n} - \mathbf{a_{n'}}) \mathbf{u}_{\mathbf{n'},j'} \tag{2.2}$$

The general expression for $\mathbf{u}_{j,\mathbf{n}}$ can be arrived at by searching first for a harmonic solution of the type:

$$\mathbf{u}_{j,\mathbf{n}} = e^{-i\omega t + i\mathbf{k}\cdot\mathbf{a_n}} \mathbf{v}_j \tag{2.3}$$

where $\mathbf{v}_j$ is the displacement of the j^{th} atom in the $\mathbf{n} = 0$ cell at time $t = 0$. In the end, Eq. 2.3 and its complex conjugate will be added together to ensure that the ion displacement is a real quantity. After replacing $\mathbf{u}_{j,\mathbf{n}}$ with Eq. 2.3, Eq. 2.2 becomes:

$$M_j \omega^2 \mathbf{v}_j = \sum_{j'} \sum_{\mathbf{n}} \mathbf{A}_{j,j'}(\mathbf{a_n}) e^{i\mathbf{k}\cdot\mathbf{a_n}} \mathbf{v}_{j'} \tag{2.4}$$

Since j ranges from 1 to r and $\mathbf{v}_j$ is a vector, Eq. 2.4 associates to each value of $\mathbf{k}$ a system of $3r$ equations, each one related to a different phonon mode. The solutions can thus be labeled by two indexes $s = 1, 2, ...3r$ and $\mathbf{k}$, and be written as $\omega(\mathbf{k}, s)$. Imposing periodic

boundary conditions [7] at the edges of the crystal (L_1, L_2, L_3) the $\mathbf{k}$ vector becomes:

$$\mathbf{k} = \frac{2\pi}{L_1} n_1 \hat{\mathbf{x}} + \frac{2\pi}{L_2} n_2 \hat{\mathbf{y}} + \frac{2\pi}{L_3} n_3 \hat{\mathbf{z}} \tag{2.5}$$

where n_1, n_2, n_3 are three integer indexes. In the case of a $1D$ chain with only one atom per unit cell [8], Eq. 2.4 simplifies into a more tractable expression:

$$M\omega^2 = \sum_n A(n) e^{ikna} \tag{2.6}$$

where a is the distance between adjacent atoms. When only the interaction between nearest neighbors is taken into account, the simplest possible phonon dispersion relation is retrieved:

$$\omega = \sqrt{\frac{2A(0)}{M}} \left| sin\left(\frac{ka}{2}\right) \right| \tag{2.7}$$

Eq. 2.7 is plotted in Fig. 2.1-A with k confined within the first Brillouin zone ($\frac{\pi}{a} \leq k \leq \frac{\pi}{a}$) [8].

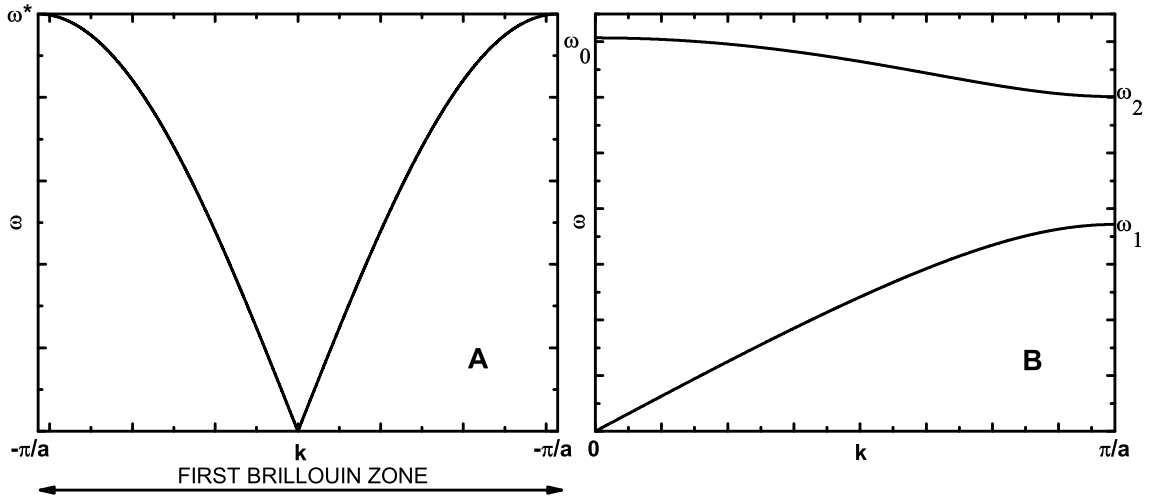

Figure 2.1: (A) Phonon dispersion relation of a one dimensional chain with one atom per unit cell, $\omega^* = \sqrt{\frac{2A(0)}{M}}$ (B) Phonon dispersion relation of a one dimensional chain with two atoms per unit cell (M_1 and M_2 with $M_2 > M_1$), $\omega_0 = \sqrt{A(0)(\frac{1}{M_1} + \frac{1}{M_2})}$, $\omega_1 = \sqrt{\frac{A(0)}{M_2}}$, $\omega_2 = \sqrt{\frac{A(0)}{M_1}}$.

Analogously, it is possible to solve Eq. 2.4 when two atoms, with masses M_1 and M_2 ($M_2 > M_1$), are present in the unit cell. In this case two distinct branches arise, as shown

in Fig. 2.1-B: an acoustic branch ($\omega = 0$ at the center of the Brillouin zone) and an optical branch ($\omega = \omega_0$ at the center of the Brillouin zone).

The general solution of Eq. 2.2 is obtained by writing a linear combination of all possible vibrational modes given by Eq. 2.3:

$$\mathbf{u}_{j,\mathbf{n}} = \sum_{\mathbf{k},s} q_{\mathbf{k},s}(t) e^{-i\omega(\mathbf{k},s)t + i\mathbf{k}\cdot\mathbf{a_n}} \mathbf{v}_j(\mathbf{k},s) \tag{2.8}$$

$q_{\mathbf{k},s}$ are called normal coordinates and satisfy an equation similar to Eq. 2.2:

$$\ddot{q}_{\mathbf{k},s} + \omega^2(\mathbf{k},s) q_{\mathbf{k},s} = 0 \tag{2.9}$$

In Eq. 2.8 the branch index, s, has been introduced. It is worth noting that $q_{\mathbf{k},s}$, with the corresponding $\mathbf{v}_j(\mathbf{k},s)$, and $\mathbf{u}_{j,\mathbf{n}}$ carry the same amount of information: they just represent displacement in different spaces (direct or reciprocal). Hence, the normal coordinates can be adopted to express any relevant physical quantity like, for instance, kinetic and potential energy:

$$\begin{aligned} T &= \tfrac{1}{2} M^{(N)} \sum_{\mathbf{k},s} |\dot{q}(\mathbf{k},s)|^2 \\ U - U_0 &= \tfrac{1}{2} M^{(N)} \sum_{\mathbf{k},s} \omega(\mathbf{k},s)^2 \, |q(\mathbf{k},s)|^2 \end{aligned} \tag{2.10}$$

if $M^{(C)}$ is the unit cell mass and N the number of cells in the volume V, $M^{(N)} = N \cdot M^{(C)}$ is the total mass of the crystalline solid.

Since $\mathbf{u}_{j,\mathbf{n}}$ is a real quantity, $q(\mathbf{k},s)$ satisfies:

$$q(-\mathbf{k},s) = q(\mathbf{k},s)^* \tag{2.11}$$

Using the so far developed formalism, the lattice vibrational problem can now be treated in purely quantum mechanical terms, namely it can be proved [9] that $q(\mathbf{k},s)$ obeys the following commutation relationship:

$$[q(\mathbf{k},s), q(\mathbf{k}',s')^*] = \frac{\hbar}{2M^{(N)}\omega(\mathbf{k},s)} \delta_{\mathbf{k},\mathbf{k}'} \delta_{s,s'} \tag{2.12}$$

It is now possible to appreciate the close similarity with the creation and annihilation

operator ($a^\dagger$ and a^-) adopted to describe a quantum harmonic oscillator [10]. The analogy can be brought even further realizing that, if $\langle N|$ represents the quantum state characterized by the presence of N phonons, then:

$$\langle N|Q(\mathbf{k},s)|N+1\rangle = \langle N+1|Q(\mathbf{k},s)^*|N\rangle = \sqrt{\frac{\hbar}{2M^{(N)}\omega(\mathbf{k},s)}(N+1)} \tag{2.13}$$

All the results so far achieved can thus be rephrased in the quantum mechanical formalism using the new quantum operators. An example is that of the total energy of the crystal, $T+U$, given by Eq. 2.10:

$$E = \sum_{\mathbf{k}}\sum_{s}\left[N(\mathbf{k},s)+\frac{1}{2}\right]\hbar\omega(\mathbf{k},s) + U_0 \tag{2.14}$$

2.2 Spontaneous Raman Scattering

Lattice vibrations in a crystal can be studied by different techniques including but not limited to *Raman scattering*, *Infrared Spectroscopy*, effective only to investigate infrared active modes and *Neutron Scattering*. Neutrons have energies of a few meV and, as opposed to electrons, are uncharged and can consequently penetrate deeply into most materials. As a result, neutron scattering is a valuable probe to study low energy, bulk excitations like lattice vibrations. In fact, it is widely employed to retrieve phonon dispersion relations. Since the work carried on in this dissertation relies heavily on Raman scattering, it will be useful to review the fundamental cornerstones of Raman spectroscopy, particularly when applied to crystal lattices.

In this spirit, the goal of this brief section is to utilize the mathematical tools developed in the previous section to describe the process of light scattering by phonons. This will be accomplished in two steps: first the calculation of the Raman tensor and secondly the definition of the Raman scattering cross section.

2.2.1 The Raman tensor

Since phonons have much lower energy than infrared and visible photons, the interaction of light with lattice vibrations has to be mediated by a third particle: free carriers (electrons

and holes). This ultimately implies that the scattering process takes place through three different steps. The Feynman diagram in Fig. 2.2-B illustrates these steps for the case of Stokes scattering (see section 2.2.2): the incident photon creates an electron (or hole), the electron (or hole) scatters and generates/annihilates a phonon, the electron (or hole) emits the outgoing photon. Momentum (Fig. 2.2-A) and energy (Fig. 2.2-B) are conserved:

$$\begin{aligned} \omega_S &= \omega_I - \Omega \\ \mathbf{k}_S &= \mathbf{k}_I - \mathbf{q} \end{aligned} \tag{2.15}$$

the subscripts S and I stand for "incident" and "scattered", Ω and $\mathbf{q}$ are the phonon frequency and momentum.

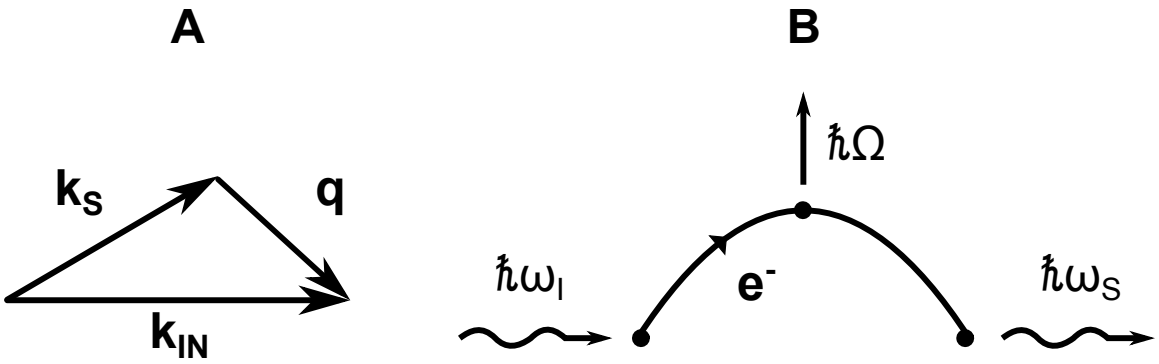

Figure 2.2: Raman scattering: conservation of momentum (A) and conservation of energy (B), ω_I ($\mathbf{k}_I$) and ω_S ($\mathbf{k}_S$) are the incident and scattered electric field frequencies (momenta), Ω ($\mathbf{q}$) is the phonon field frequency (momentum).

The physical variable that most properly characterizes a scattering process is the scattering probability: the probability, usually per unit time, that a photon with energy $\hbar\omega_I$ scatters into a photon with energy $\hbar\omega_S$. This quantity can be calculated using the total Hamiltonian of the lattice:

$$H = H_0 + H_{ER} + H_{EL} \tag{2.16}$$

Here, H_0 is the Hamiltonian of the unperturbed system:

$$H_0 = H_L + H_E = U_0 + \sum_{\mathbf{k}} \sum_{s} \left[N(\mathbf{k}, s) + \frac{1}{2} \right] \hbar\omega(\mathbf{k}, s) + \sum_{\alpha, \mathbf{k}} \epsilon_{\alpha,\mathbf{k}} c^{\dagger}_{\alpha,\mathbf{k}} c_{\alpha,\mathbf{k}} \tag{2.17}$$

which includes the phonon energy, H_L, given by Eq. 2.14 and the electron energy, H_E. $\epsilon_{\alpha,\mathbf{k}}$

is the energy of an electron located in the α band and having momentum $\mathbf{k}$, $c_{\alpha,\mathbf{k}}$ and $c^{\dagger}_{\alpha,\mathbf{k}}$ are the electron creation and annihilation operators. On the other hand, H_{ER} and H_{EL} are the electron-radiation and the electron-phonon Hamiltonian respectively. After introducing the creation ($a^{\dagger}_{\mathbf{k}}$) and annihilation ($a^{-}_{\mathbf{k}}$) operators for photons with wave vector $\mathbf{k}$:

$$\langle n_{\mathbf{k}} - 1|a^{-}_{\mathbf{k}}|n_{\mathbf{k}}\rangle = \langle n_{\mathbf{k}}|a^{\dagger}_{\mathbf{k}}|n_{\mathbf{k}} - 1\rangle = \sqrt{n_{\mathbf{k}}} \tag{2.18}$$

where $n_{\mathbf{k}}$ indicates the number of photons, it is possible [11] to derive the electron-radiation Hamiltonian:

$$H_{ER} = \frac{e}{m}\sum_{j}\sum_{\mathbf{k}}\left(\frac{2\pi\hbar}{\epsilon V\omega_{\mathbf{k}}}\right)\frac{1}{2}[a^{-}_{\mathbf{k}}e^{i\mathbf{k}\cdot\mathbf{r}_j} + a^{\dagger}_{\mathbf{k}}e^{-i\mathbf{k}\cdot\mathbf{r}_j}]\boldsymbol{\epsilon}_{\mathbf{k}}\cdot\mathbf{p}_j \tag{2.19}$$

where $\mathbf{p}_j$ and $\mathbf{r}_j$ are the electron momentum and position, ϵ is the dielectric constant, V the volume of the crystal and $\boldsymbol{\epsilon}_{\mathbf{k}}$ the polarization of the photon with wave vector $\mathbf{k}$. The matrix elements of H_{ER} are non zero only when the initial ($|\alpha>$) and final ($|\beta>$) state differ by a single electron or hole; in both cases the momentum matrix element is written like $\mathbf{p}_{\alpha\beta} =< \alpha|\mathbf{p}_j|\beta >$.

The electron-optical phonon interaction can be easily described in the simple case of a crystal with two atoms, with masses M_1 and M_2, per unit cell. The relative displacement at position $\mathbf{R}$ of the two ions produced by a phonon belonging to the s branch and with wave vector $\mathbf{q}$ can be written, analogously to Eq. 2.8, as [12]:

$$\mathbf{U}(\mathbf{R}) = \left(\frac{\hbar}{2MN\omega_{s\mathbf{q}}}\right)^{\frac{1}{2}}\mathbf{v}_{s\mathbf{q}}e^{i\mathbf{q}\cdot\mathbf{R}}(b^{\dagger}_{s-\mathbf{q}} + b^{-}_{s\mathbf{q}}) \tag{2.20}$$

where $b^{\dagger}_{s\mathbf{q}}$ and $b^{-}_{s\mathbf{q}}$ are related to $Q^{*}(s,\mathbf{q})$ and $Q(s,\mathbf{q})$ by:

$$\begin{aligned} b^{\dagger}_{s\mathbf{q}} &= q^{*}(\mathbf{q},s)\sqrt{\tfrac{2M^{(N)}\omega(\mathbf{q},s)}{\hbar}} \\ b^{-}_{s\mathbf{q}} &= q(\mathbf{q},s)\sqrt{\tfrac{2M^{(N)}\omega(\mathbf{q},s)}{\hbar}} \end{aligned} \tag{2.21}$$

and $M = \frac{M_1M_2}{M_1+M_2}$ is the effective mass of the unit cell. In [13] it is shown that the matrix elements of the electron phonon interaction are a function of the deformation potential which accounts for the change in the lattice energy produced by an excited phonon $\mathbf{q}$,

$\Xi \equiv \frac{\partial H}{\partial \mathbf{q}}$:

$$\langle \alpha | H_{EL} | \beta \rangle = \Xi^i_{\alpha\beta} \frac{\bar{U}_i}{a} \tag{2.22}$$

where $\bar{U}_i$ is just Eq. 2.20 without the exponential term and a is the lattice constant.

The probability that, within time T, a photon $(\omega_1, \mathbf{k}_1)$ will be scattered into a photon $(\omega_2, \mathbf{k}_2)$ generating a phonon $(\Omega, \mathbf{q})$ can be computed employing time dependent perturbation theory [12, 14]:

$$W(T) = \frac{4\pi^3 T e^4}{\hbar^3 m^4 \epsilon^2 a^2 MN} \sum_{\mathbf{q},\mathbf{k_2}} \frac{n_1(n_0+1)}{\Omega\omega_1\omega_2} \qquad \left| v^i_{0\mathbf{q}} R^i_{12}(-\omega_1, \omega_2, \Omega) \right|^2 \times \frac{(2\pi)^3}{V} \delta(\mathbf{k_1} - \mathbf{q} - \mathbf{k_2})\, \delta(\omega_1 - \Omega - \omega_2) \tag{2.23}$$

where n_1 and n_0 represent the number of photons and phonons present. R^i_{12} is given by summing over all possible electronic states α and β:

$$\begin{aligned} R^i_{12}(-\omega_1, \omega_2, \Omega) = & \frac{1}{V} \sum_{\alpha\beta} \left\{ \frac{p^2_{0\beta} p^1_{\beta\alpha} \Xi^i_{\alpha 0}}{(\omega_\beta + \Omega - \omega_1)(\omega_\alpha + \Omega)} + \frac{p^1_{0\beta} p^2_{\beta\alpha} \Xi^i_{\alpha 0}}{(\omega_\beta + \Omega + \omega_2)(\omega_\alpha + \Omega)} \right. \\ & + \frac{p^2_{0\beta} \Xi^i_{\beta\alpha} p^1_{\alpha 0}}{(\omega_\beta + \Omega - \omega_1)(\omega_\alpha - \omega_1)} + \frac{p^1_{0\beta} \Xi^i_{\beta\alpha} p^2_{\alpha 0}}{(\omega_\beta + \Omega + \omega_2)(\omega_\alpha + \omega_2)} \\ & \left. + \frac{\Xi^i_{0\beta} p^2_{\beta\alpha} p^1_{\alpha 0}}{(\omega_\beta + \omega_2 - \omega_1)(\omega_\alpha - \omega_1)} + \frac{\Xi^i_{0\beta} p^1_{\beta\alpha} p^2_{\alpha 0}}{(\omega_\beta + \omega_2 - \omega_1)(\omega_\alpha + \omega_1)} \right\} \end{aligned} \tag{2.24}$$

The superscripts 1 and 2 on the elements of the p matrix indicate that the component of p along the direction of polarization of ω_1 or ω_2 has to be taken. R^i_{12} is the "Raman tensor" and its subscripts refer to the polarization of the incident and scattered photon while the signs in front of the frequencies in parenthesis (left hand side of Eq. 2.24) are chosen so that a positive frequency corresponds to creation and a negative frequency to destruction of the corresponding photon or phonon. Each of the six terms making up R^i_{12} can give rise to a resonance in the scattering process [15, 16]; in practice, this happens, for example, when the energy of the incident photon matches the material band gap. It is also important to notice that in Eq. 2.23 the two delta functions guarantee the conservation of momentum and energy as depicted in Fig. 2.2. As suggested by the name, R is a second-order tensor whose structure is subject to the crystal symmetry transformations. Using group theory [17], it is possible to construct the tensors for the modes (irreducible representations) of all

existing point groups [18]. It turns out that the Raman tensor can be alternatively defined as $R^i_{mn} = \frac{\partial \chi_{mn}}{\partial q_i}$ [19], where χ_{mn} is the electric susceptibility and $q_i = q_{\mathbf{k},s}\mathbf{v}_i(\mathbf{k}, s)$, following Eq. 2.8 notation.

2.2.2 Scattering cross section

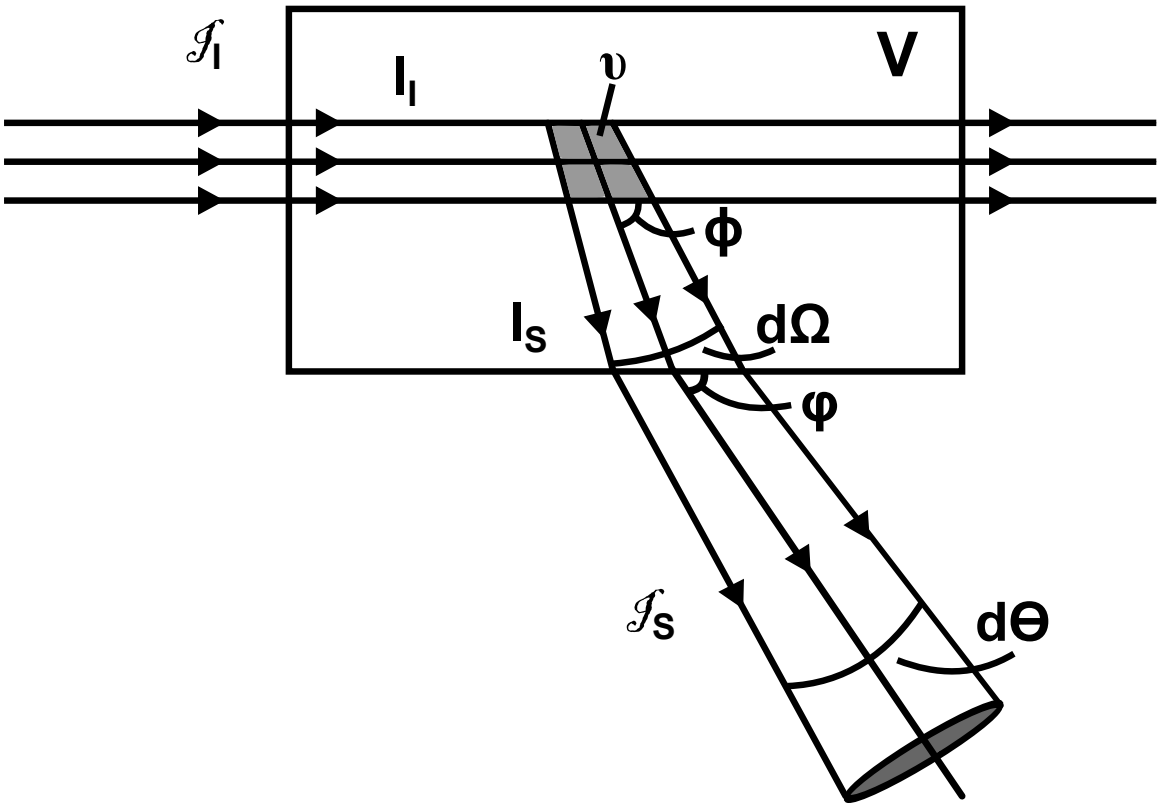

Figure 2.3: Raman scattering experiment, from [20].

The Raman tensor defined in Eq. 2.24 is usually included into another physical quantity, the *Raman scattering cross section*, which is particularly appropriate to characterize Raman scattering from an experimental viewpoint. In order to introduce this new function, it is necessary to briefly outline the main features of a standard Raman scattering experiment, see Fig. 2.3. The incident laser light with intensity $\mathfrak{I}_I$ is shined against a sample of volume V. Only a fraction of it, I_I, penetrates the sample and excites a smaller volume υ so that part of it, I_S, is scattered by an angle ϕ into a solid angle $d\Omega$. The scattered light is then transmitted outside the sample, $\mathfrak{I}_S$, and collected by a lens which is at an angle φ from the incident light direction and covers the solid angle $d\Theta$. In general, it is rather

involved to calculate the relationship between $\mathfrak{I}_I$ and I_I, $\mathfrak{I}_S$ and I_S, ϕ and φ. Hence, it is usually preferable to treat the scattering experiment "inside" the sample in order to avoid the intricacies caused by taking refraction into account.

The traditional approach to identify a particular scattering geometry is through the use of Porto notation [21]: $x_1(y_1y_2)x_2$. x_1 and x_2 indicate respectively the incident and scattered beam propagation direction, whereas y_1 and y_2 label the incident and scattered beam electric field polarization with respect to crystal axes. This compact notation fully defines a Raman scattering experiment and allows using the Raman tensors to calculate the selection rules of a particular mode.

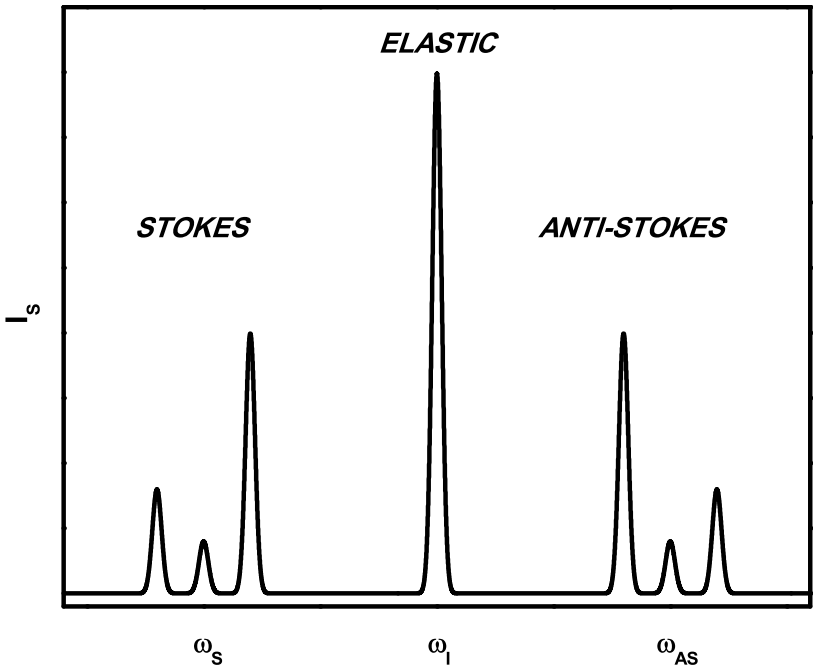

Figure 2.4: Raman scattering spectrum, from [20].

A typical Raman spectrum looks like Fig. 2.4; the different features present can be grouped into three different categories: elastic scattering at the same frequency, ω_I, as the incident laser; Stokes scattering at a lower frequency, ω_S, than the incident laser frequency; and anti-Stokes scattering a higher frequency, ω_{AS}, than the incident laser frequency. Stokes scattering corresponds to the excitation of a new particle (in this work usually a phonon) with consequent loss of energy by the incident light and has already been discussed in the previous section, see in particular Eq. 2.15. On the other hand, anti-Stokes scattering corresponds to the annihilation of an existing particle, so that the scattered radiation has

a higher frequency than the incident radiation. In analogy with Eq. 2.15:

$$\begin{aligned} \omega_{AS} &= \omega_I + \Omega \\ \mathbf{k}_{AS} &= \mathbf{k}_I + \mathbf{q} \end{aligned} \tag{2.25}$$

where again Ω is the frequency of the absorbed phonon.

Within the Raman scattering experiment context so far illustrated, the concept of a scattering cross section can now be introduced:

$$\sigma = \frac{Power\ Removed}{I_I} \tag{2.26}$$

defined as the rate at which energy is removed from the incident beam divided by the incident intensity. The rate of scattering into a solid angle $d\Omega$ with scattering frequency between ω_S and $\omega_S + d\omega_S$ is then given by $I_I \frac{d^2\sigma}{d\Omega d\omega_S} d\Omega d\omega_S$. $\frac{d^2\sigma}{d\Omega d\omega_S}$ quantifies the scattering efficiency of a particular excitation inside the sample and can be exactly derived following a standard electromagnetic approach [20] and invoking the fluctuation-dissipation theorem [22]. In the Stokes case, the differential scattering cross section is:

$$\frac{d^2\sigma}{d\Omega d\omega_S} = \frac{\hbar\omega_I\omega_S^3 v V n_S |\epsilon_0 x_S^i x_I^j R_{ij}(-\omega_I, \omega_S, \Omega)|^2 (n(\Omega)+1)}{(4\pi\epsilon_0)^2 2c^4 n_I \Omega} g_\Omega(\omega_S) \tag{2.27}$$

where n_I and n_S are refractive index of the sample at the incident and scattered light frequency, $R_{ij}(-\omega_I, \omega_S, \Omega)$ is the Raman tensor defined in Eq. 2.24 and x_I^i and x_S^j are the i^{th} and j^{th} component of unit vectors parallel to the incident and scattered field. Eq. 2.27 is valid solely for a non-degenerate phonon mode, hence the omission of the superscript (R^l) present in Eq. 2.24. In the general case, R_{ij} should be replaced by $\sum_l v_{s,\boldsymbol{\kappa}}^l R_{ij}^l$, see Eq. 2.23. The shape of the Raman line, in the specific case of scattering by a phonon, can be described by a Lorentzian [20]:

$$g_\Omega(\omega) = \frac{\Gamma/2\pi}{(\Omega-\omega)^2 + (\Gamma/2)^2} \tag{2.28}$$

where Γ is the phonon decay rate. $n(\Omega)$ is the Bose-Einstein factor:

$$n(\Omega) = \frac{1}{e^{\hbar\Omega/k_B T} - 1} \tag{2.29}$$

and is what is mainly responsible for the $\frac{d^2\sigma}{d\Omega d\omega_S}$ dependence on temperature. The scattering cross section remains unchanged in the case of anti-Stokes scattering except for the $n(\Omega)+1$ term which is replaced by $n(\Omega)$. The ratio of the anti-Stokes and Stokes cross sections for the same mode is given by:

$$\frac{n(\Omega)}{n(\Omega)+1} = e^{-\hbar\Omega/k_B T} \tag{2.30}$$

It is obvious that Stokes scattering is always dominant except at very high temperature when the two phenomena have comparable strength. For this reason, Stokes scattering has always been preferred to anti-Stokes in all the experiments discussed later on.

2.3 Impulsive Stimulated Raman Scattering (ISRS)

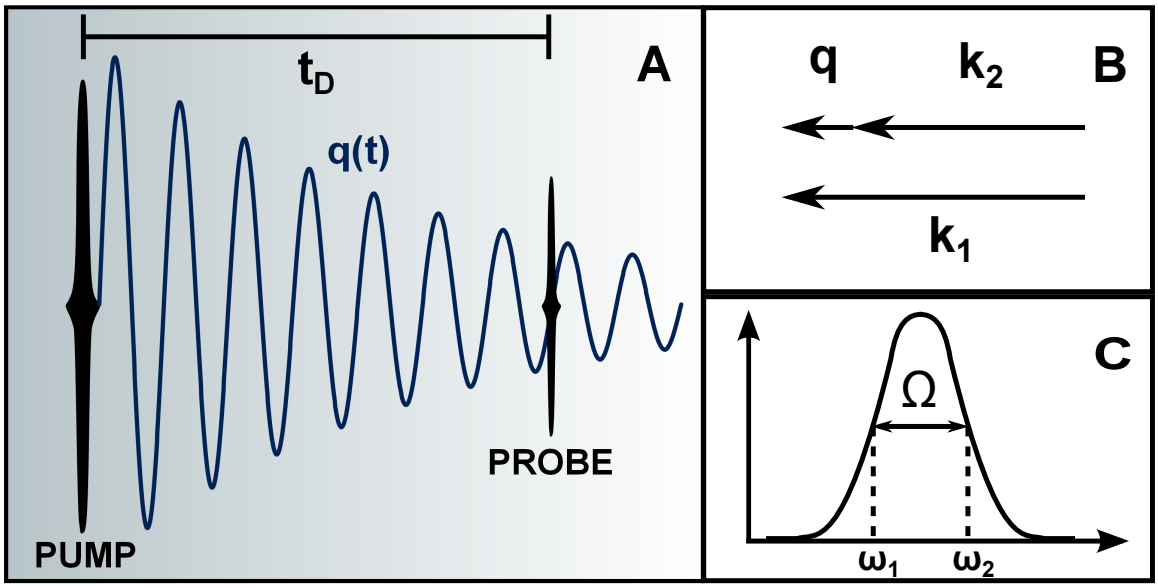

Figure 2.5: (A) Temporal profile of the phonon amplitude, $q(t)$, in a pump probe experiment (B) Momentum conservation (C) Energy conservation. $(\mathbf{k_1}, \omega_1)$ and $(\mathbf{k_2}, \omega_2)$ are the "incident" and "scattered" field (both part of the pump pulse), $(\mathbf{q}, \Omega)$ is the phonon field.

Spontaneous Raman scattering is fundamentally an incoherent process: there is no correlation between the phase of each quantum of vibration and the generated phonons are emitted in all directions. The consequent difficulty in the collection of the scattered radiation has substantial repercussions on the signal to noise ratio which is sometimes already jeopardized by the presence of strong interferences (elastic scattering from surface roughness or fluorescence in the sample).

Similarly to what happens in the stimulated emission of photons process in a laser, phonons can also be excited coherently. Since two beams, with wave vector $\mathbf{k}_1$ and $\mathbf{k}_2$, are involved in the generation process of a coherent phonon, its wave vector is uniquely determined: $\mathbf{q} = \mathbf{k}_1 - \mathbf{k}_2$. Consequently, the phonon amplitude, $q(t)$, oscillates with a very well defined phase. Coherent Raman spectroscopy takes care of a lot of the issues affecting spontaneous Raman: the signal achieved is orders of magnitudes higher than in the spontaneous Raman case and can be easily detected and, if needed, spatially filtered. Coherent Raman scattering is implemented in several different experimental geometries whose names and features are given, for example, in Levenson's review paper [23]. With the advent of pulsed lasers a new technique, Impulsive Stimulated Raman Scattering, has imposed itself on the scene of Raman spectroscopy thanks to the enormous peak power achievable and the consequent potential for even higher intensity signals. Fig. 2.5 portrays an intuitive picture of a typical ISRS experiment: the pump beam, whose pulse width is significantly shorter than the phonon frequency, excites a coherent phonon, $q(t)$, which is then detected by the probe beam, delayed by a time t_D with respect to the pump. In this way, adjusting t_D by means of a translation stage, it is possible to follow the time evolution of the phonon amplitude. The rest of the chapter substantiates this qualitative description with a more rigorous analysis culminating in the expression for the differential transmission or reflection.

2.3.1 ISRS in transparent materials

In transparent materials coherent phonons give rise to a bulk contribution and to boundary effects as well; moreover, given the absence of absorption inside the sample, it is possible to detect the phonon field measuring either the transmitted or the reflected probe. Thus, ISRS will be discussed first in the case of transparent materials. The results obtained will be then extended to the case of absorbing materials, where only the boundary effects on reflection have to be taken into account.

2.3.1.1 Generation of coherent phonons

To describe the generation of coherent phonons process, two coupled equations have to be solved: the lattice vibration normal mode equation (see Eq. 2.9) and Maxwell's equation for the pump electric field. Including damping in Eq. 2.9 and assuming that the incident and scattered field propagate along z and are linearly polarized along y, the two equations are given by [24]:

$$\begin{aligned} \frac{d^2q}{dt^2} + 2\gamma\frac{dq}{dt} + \Omega^2 q &= \frac{1}{2}RE^2 \\ \frac{d^2E}{dz^2} - \frac{n^2}{c^2}\frac{d^2E}{dt^2} &= \frac{4\pi}{c^2}R\frac{d^2}{dt^2}(qE) \end{aligned} \tag{2.31}$$

E is the electric field and Ω is just one of the $\omega(\mathbf{k}, s)$ defined by Eq. 2.4 evaluated at the center of the Brillouin zone, i.e. $\mathbf{k} = 0$. Since both the incident and scattered electric field are polarized along y, R in Eq. 2.31 is just R_{22} as defined in Eq. 2.24. The two equations in 2.31 are usually solved in the case of a Gaussian-like laser pulse:

$$E_L = Ae^{(t-zn/c)^2/2\tau_L^2} cos[\omega_L(t - zn/c)] \tag{2.32}$$

where ω_L is the laser frequency and τ_L its temporal width. Under the assumption of undepleted electric field, i.e. $|E_L(t)|$ constant, the phonon amplitude can be written as:

$$q(z > 0, t > 0) = Q_0 e^{-\gamma(t-zn/c)} sin[\Omega(t - zn/c)] \tag{2.33}$$

where Q_0 is given by:

$$Q_0 = \frac{\sqrt{\pi}}{4\Omega} RA^2\tau_L e^{-\Omega^2\tau_L^2/4} = \frac{2\pi I}{\Omega nc} Re^{-\Omega^2\tau_L^2/4} \tag{2.34}$$

I is, in this case, the pump beam intensity:

$$I = \frac{ncA^2\tau_L}{8\sqrt{\pi}} \tag{2.35}$$

Eq. 2.33 and Eq. 2.34 highlight some of the most important aspects shared by any pump probe experiment. The phonon field oscillates like a sine. As will be discussed later, this is the expected response in the case of impulsive excitation. The phonon amplitude is a linear

function of the pump intensity (I): the linear regime is exited only whenever the pump power is so high to drive some kind of higher order process. $q(t)$ depends exponentially on $(\Omega\,\tau_L)^2$, therefore the laser pulse width has a very pronounced impact on the amplitude of the coherent phonon oscillations.

2.3.1.2 Detection of coherent phonons: bulk contribution

In order to detect the coherent phonons launched by the pump, it is necessary to probe the sample with another pulsed laser beam. This beam tracks the impact of the lattice vibrations on the sample optical parameters at different instants subsequent to the pump arrival (normally called time zero). The change induced in the probe intensity and spectrum can be quantitatively calculated solving again Maxwell's equations in the presence of a coherent phonon oscillation. If t_D is the time delay between pump and probe beam (see Fig. 2.5), it is convenient to rewrite Eq. 2.33 as:

$$q(t') = Q'_0 e^{-\gamma t'} sin[\Omega(t' + t_D)] \tag{2.36}$$

where $t' = t - zn/c$, $Q'_0 = Q_0 e^{-\gamma t_D}$ and the pump beam is assumed to hit the sample at time $t = -t_D$. The differential equation governing the probe electric field is [24]:

$$\frac{\partial^2 E}{\partial z^2} - \frac{2n}{c}\frac{\partial^2 E}{\partial z \partial t'} = \frac{4\pi}{c^2} R \frac{\partial^2}{\partial t'^2}\left[q(t')E_L(t')\right] \tag{2.37}$$

As in Eq. 2.31, E_L is the incident pulse whose temporal profile is defined in Eq. 2.32. For a sample of thickness l, the Fourier Transform of the solution of Eq. 2.37 reads:

$$E(z,\omega) = E_L(\omega) + B\omega[e^{i\Omega t_D} E_L(\omega + \Omega) - e^{-i\Omega t_D} E_L(\omega - \Omega)] \tag{2.38}$$

with $B = \frac{\pi}{cn} R\, l\, Q'_0$. It is important to notice that the transmitted electric field contains three different components, see Fig. 2.6-A: the unperturbed probe, $E_L(\omega)$, and two out of phase terms shifted in frequency by $\pm\Omega$ with respect to $E_L(\omega)$. It is immediate to recognize in these extra components the Stokes and anti-Stokes fields already discussed in Sec. 2.2.2. Since photo detectors are usually only sensitive to the field power, it is necessary to calculate

the spectrum of the transmitted field intensity:

$$I_T(\omega) \simeq ae^{-(\omega-\omega_L)^2\tau_L^2} + 2aB\omega e^{-\Omega^2\tau_L^2/4} cos(\Omega t_D) \left\{ e^{-[\omega-(\omega_L-\Omega/2)]^2\tau_L^2} - e^{-[\omega-(\omega_L+\Omega/2)]^2\tau_L^2} \right\} \tag{2.39}$$

where $a = ncA^2\tau_L^2/16\pi$. Eq. 2.39 is graphed in Fig. 2.6-B together with the intensity of the incident probe field, $I_0(\omega) = \frac{nc}{4\pi}|E_L(\omega)|^2$.

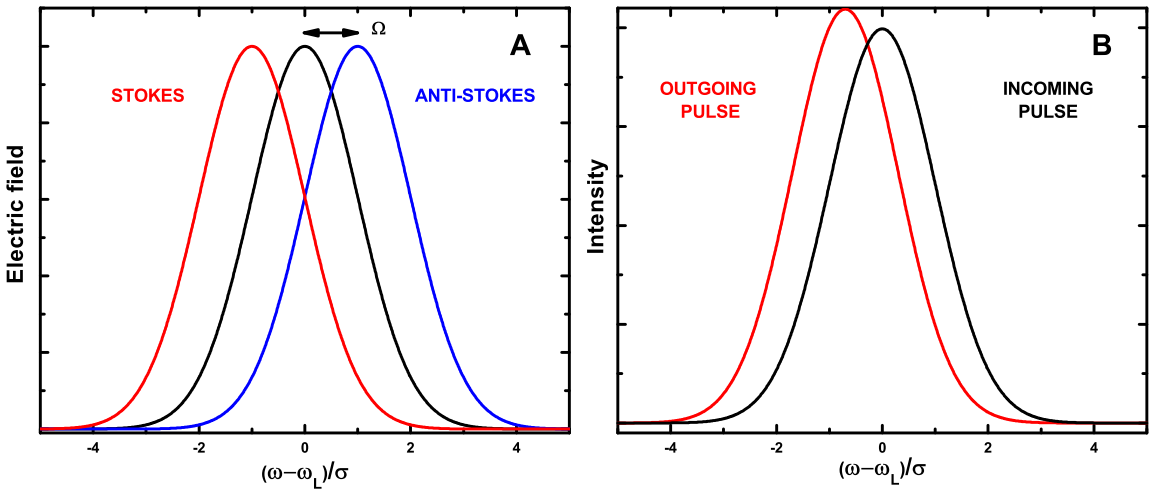

Figure 2.6: (A) Different spectral components present in the probe transmitted electric field (see Eq. 2.38): unperturbed probe (black), Stokes term (shifted by $-\Omega$), anti-Stokes term (shifted by Ω) (B) Spectrum of the incident and transmitted probe intensity: the outgoing pulse is distorted and shifted to lower or higher frequencies depending on the value of t_D. σ is the FWHM of the laser spectrum.

When $cos(\omega_0 t_D) > 0$, the phonon field shifts in frequency the probe spectrum by adding low frequency components (Stokes) and subtracting high frequency components (anti-Stokes), in accordance with the expression within brackets in Eq. 2.39. Since the shift is in the opposite direction when $cos(\omega_0 t_D) < 0$, the red Gaussian in Fig. 2.6-B oscillates back and forth around the black one at frequency Ω. If I_0 is the unperturbed transmitted probe intensity, the differential transmitted probe $\frac{\Delta I_T}{I_0} = \frac{I_T - I_0}{I_0}$, which is the physical quantity measured in a pump probe experiment, can be obtained subtracting $I(\omega)$ from Eq. 2.39 and integrating in $d\omega$:

$$\frac{\Delta I_T}{I_0} = -l\, I_{pump}\, e^{-\Omega^2\tau_L^2/2}\, e^{-\gamma t_D}\, cos(\Omega t_D) \left(\frac{2\pi}{cn}\right)^2 R^2 \tag{2.40}$$

At this point, it ought to be noticed that when the intensity is measured by a photon counting detector, I_T and I_0, obtained integrating the spectrum divided by $\hbar\omega$, do not differ from each other: the presence of a coherent phonon does not modify the number of photons but only their frequency. This poses a serious experimental issue since it would not be possible to measure effectively ΔI_T employing a semiconductor photo diode or a PMT [19, 25]. To overcome this difficulty it is common practice to spectrally resolve the probe, i.e. to band pass filter the transmitted probe so that the photo detector integration is performed only in the range where the difference between the number of transmitted and unperturbed probe photons is the largest.

2.3.1.3 Detection of coherent phonons: Boundary effects

The probe beam can be affected by the presence of a coherent phonon in a way different than the one described by Eq. 2.37. Whenever light encounters an interface between media with different refractive index, it experiences reflection and refraction (or transmission). Since both phenomena depend on the value of the refractive index, any physical process affecting n will automatically leave a mark on the reflected and transmitted field. The relationship between a phonon, $q(t)$, and the dielectric constant, ϵ, in general can be written, in first order, as:

$$\epsilon = \epsilon_0 + 4\pi \frac{\partial \chi}{\partial q} q(t) + ... \tag{2.41}$$

where χ is the electrical susceptibility. As pointed out at the end of Sec. 2.2, it is possible to write:

$$\frac{\partial \chi}{\partial q} = R = \sum_{ij} e_i e_j R_{ij} \tag{2.42}$$

where e_i and e_j are the direction cosines of the probe field and R_{ij} is defined in Eq. 2.24. Recalling that $n(\omega) = \sqrt{\epsilon(\omega)}$ and using the Fresnel coefficients for transmission and reflection in the case of normal incidence [26], leads to:

$$\frac{\Delta I_R}{I_0} = \frac{-4\pi}{n_0(n_0^2 - 1)} R\, Q_0\, e^{-\gamma t_D}\, sin(\Omega t_D) \tag{2.43}$$

for reflection and:

$$\frac{\Delta I_T}{I_0} = \frac{4\pi(n_0 - 1)}{n_0^2(n_0 + 1)} R\, Q_0\, e^{-\gamma t_D}\, sin(\Omega t_D) \tag{2.44}$$

for transmission. Eq. 2.40 is different from Eq. 2.43 and Eq. 2.44 in two respects: the length of the sample l does not enter the expression of the differential transmission and reflection when the boundary effects are considered; the bulk signal has a sine dependence while the boundary one has a cosine dependence. This latter aspect has been discussed and experimentally verified in the case of $LaAlO_3$ by Liu et al. [27].

2.3.2 The two Raman tensors

The generation equation, Eq. 2.31, and the detection equation, Eq. 2.37, contain the Raman tensor which, so far, has been assumed to be the same in both cases. However, a more careful examination of the two processes [2] reveals that the tensor involved in the equation of motion driving term (right hand side of Eq. 2.31) is profoundly different from the one that accounts for the impact of the lattice vibration on the dielectric constant, see Eq. 2.41. In 2002 Stevens and coworkers published a comprehensive work that analyzed in detail the nature of the two tensors and provided an analytical expression for both of them. The final result will be reported here in the case of a two band process, assuming a constant deformation potential ($\Xi_{mn} = \Xi_0$) and retaining only the most resonant terms in the fractions in Eq. 2.24. The non zero elements of the generation Raman tensor are:

$$\pi_{ij}^R \approx \frac{\Xi_0}{4\pi\hbar}\left[\frac{\mathrm{d}Re(\epsilon)}{\mathrm{d}\omega} + 2i\frac{Im(\epsilon)}{\Omega}\right] \tag{2.45}$$

while the detection Raman tensor components are:

$$\chi_{ij}^R \approx \frac{\Xi_0}{4\pi\hbar}\left[\frac{\mathrm{d}Re(\epsilon)}{\mathrm{d}\omega} + i\frac{\mathrm{d}Im(\epsilon)}{\mathrm{d}\omega}\right] \tag{2.46}$$

Hence R^2 in Eq. 2.40, Eq. 2.43 and Eq. 2.44 is actually:

$$R^2 = \left(\sum_{ij} e_i \pi_{ij}^R e_j\right) \cdot \left(\sum_{ij} \bar{e}_i \chi_{ij}^R \bar{e}_j\right) \tag{2.47}$$

where e_i and $\bar{e_i}$ are respectively the pump and probe direction cosines. The distinction between the two Raman tensors manifests itself almost exclusively in the case of absorbing materials, $Im(\epsilon) >> Re(\epsilon)$, when $\chi^R_{ij} \propto \frac{dIm(\epsilon)}{d\omega}$, while $\pi^R_{ij} \propto \frac{Im(\epsilon)}{\Omega}$. When there is no absorption, i.e., when the laser frequency is below the material band gap in the case of semiconductors, χ^R and π^R are equal and coincide with the Raman tensor defined in Eq. 2.24 and Eq. 2.27. Hence, in transparent materials spontaneous and stimulated Raman scattering are governed by the same tensor.

2.3.3 ISRS in opaque materials

In Eq. 2.31 the driving term, $F(t)$, has been treated as a replica of the electric field intensity, $F(t) \propto |E|^2$. Yet, this is not always the case as can be seen looking at the expression of the driving force [2, 28]:

$$F(t) \propto \sum_{kl} \int_{-\infty}^{+\infty} \int_{-\infty}^{+\infty} e^{-i\Omega t}\, E_l(\omega)\, \pi^R_{kl}\, E^*_k(\omega - \Omega)\, \mathrm{d}\omega \mathrm{d}\Omega \tag{2.48}$$

Adopting the simplified form for π^R_{kl} reported in Eq. 2.45, it is instructive to calculate the temporal profile of $F(t)$ in the two different conditions so far considered: transparent material ($\pi^R_{kl} \propto \frac{dRe(\epsilon)}{d\omega}$) and absorbing material ($\pi^R_{kl} \propto \frac{Im(\epsilon)}{\Omega}$). Assuming for simplicity a delta-like field intensity, in the former case $F(t) \propto |E(t)|^2$ and thus the force exhibits an impulsive character, in the latter $F(t) \propto \int_{-\infty}^{t} |E(t')|^2\, \mathrm{d}t'$ and the force behaves more like a step function, whence the term "displacive". The time evolution of the phonon amplitude can be computed in the case of displacive excitation, similarly to what done for the impulsive case, see Eq. 2.33. If the right hand side of Eq. 2.33 is replaced by:

$$F(t) = F_0 \Theta(t) \tag{2.49}$$

where $\Theta(t)$ is the Heaviside step function and F_0 is a coefficient that depends on π^R_{kl}, $q(t)$ becomes:

$$q(t) = \frac{F_0}{\Omega^2 + \gamma^2} - \frac{F_0 e^{-\gamma t} \cos(\Omega t + \varphi)}{\Omega \sqrt{\Omega^2 + \gamma^2}} \tag{2.50}$$

with

$$\varphi = -\text{atan}\left(\frac{\gamma}{\Omega}\right) \tag{2.51}$$

Eq. 2.50 clearly shows that in absorptive materials $q(t)$ exhibits a predominant cosine dependence (if $\Omega >> \gamma$) as opposed to the pure sine present in Eq. 2.33. A step like driving force generates also a DC term which physically corresponds to a rigid displacement of all the lattice ions from their equilibrium position. Moreover, the oscillatory part in Eq. 2.50 depends on $\frac{1}{\Omega^2}$, while in Eq. 2.33 is proportional to $\frac{1}{\Omega}$

Although it may seem that Eq. 2.48 is encompassing all the conceivable scenarios, it has recently been shown [3] that, in the displacive excitation case, it is necessary to contemplate another possibility: a decay in the step-like force exciting the lattice vibrations. It is in fact natural to expect that, even in opaque materials, the driving term gradually vanishes, concomitantly for instance with the recombination of the excited carriers generated in the conduction and valence band. Introducing a new decaying constant (Γ_R), $F(t)$ can be written as:

$$F(t) = F_0 e^{-\Gamma_R t}\Theta(t) \tag{2.52}$$

Following the same procedure that led to Eq. 2.50, a new expression for $q(t)$ is found:

$$q(t) = \frac{F_0 e^{-\Gamma_R t}}{\Omega^2 + (\Gamma_R - \gamma)^2} - \frac{F_0 e^{-\gamma t}\cos(\Omega t + \varphi)}{\Omega\sqrt{\Omega^2 + (\Gamma_R - \gamma)^2}} \tag{2.53}$$

with

$$\varphi = \text{atan}\left(\frac{\Gamma_R - \gamma}{\Omega}\right) \tag{2.54}$$

Eq. 2.50 and Eq. 2.53 are very similar but not identical: the presence of a non zero decay Γ_R affects both the amplitude and the phase of the phonon mode. Performing both stimulated and spontaneous Raman scattering on the same material, it is possible to extract experimentally the value of the decaying constant for a specific phonon mode and to identify its connections with the semiconductor properties and the particular vibrational mode group symmetries [3].

CHAPTER III

Experimental Procedures

Despite the involved concepts underlying the coherent phonon theory introduced in Chap. II and the intricacies of the data analysis and interpretation, the greatest hindrance to the completion of this dissertation turned out to be the series of experimental challenges faced in the lab and, sometimes, only partially overcome. This chapter is aimed at introducing the optical equipment and the principal techniques adopted during the course of the experiments with a special emphasis on their impact on the collected data quality. Since the laser sources, both pulsed and CW, have been amply discussed elsewhere [29, 30], they will not be described here but just mentioned in passing whenever needed in the context of the different topics. The chapter is structured to follow the laser path through a standard pump probe setup: the beam, loaded with different kinds of noise (Sec. 3.1), undergoes phase or amplitude modulation (Sec. 3.4), is focused onto the sample, transmitted through or reflected by it (Sec. 3.5), collected by a photo detector (Sec. 3.2) and finally amplified and filtered by a lock-in amplifier (Sec. 3.3). The last section (Sec. 3.6) is dedicated to another major experimental issue in ultrafast optics: pulse width measurement techniques.

3.1 Noise

The most established index for evaluating the reliability of any experimental measurement is probably the signal to noise ratio (SNR), a thorough review of SNR employment in various scientific fields can be found, for instance, in [31]. When the SNR falls below a certain threshold it is no longer possible to meaningfully analyze the data collected or to fit it satisfactorily with an appropriate mathematical function. The signal intensity often

times depends on parameters that are not fully controllable: sample properties (thickness, purity, defect concentration, etc.) and intrinsic limitations of the experimental equipment (e.g. laser bandwidth and fluence). It is thus natural, when attempting to optimize the SNR, to mainly try to reduce the noise. Minimizing disturbances is a far from trivial task and requires an accurate knowledge of the sources to which the noise can be ascribed. This first section addresses therefore the issue of noise reduction in optical measurements presenting first a characterization of the noise spectrum and successively outlining all the feasible strategies adopted to improve the SNR.

3.1.1 Noise spectrum

The noise present in optical measurements can almost always be attributed to three sources:

- mechanical noise
- laser noise
- electronic noise

Mechanical noise is directly related to any vibration that can couple to the optical table and potentially trigger one or multiple resonances. As can be observed in Fig. 3.1, the resonances are relatively narrow band and are confined to a very low frequency range ($< 1kHz$): attention should consequently be paid, when choosing the reference frequency in any heterodyne detection scheme, to avoid exciting any of them. Laser noise is a fairly complicated phenomenon and to be properly explained would require a long discussion which is beyond the scope of this dissertation. Oversimplifying, it can be broken down into amplitude noise (fluctuations in the power of the laser beam), phase noise (instability in the laser line frequency location) and, as in the case of mode-locked lasers, timing jitter, i.e. random variation in the time separation of the laser pulses. The primary remedy adopted to mitigate amplitude noise is to resort, whenever possible, to balanced detection techniques. Before directing the laser to the sample under test the beam can be split into two components of equal power, one is focused onto the sample and then steered to a photo diode, the other one is sent directly to a second photo diode with the same responsivity: if the outputs of

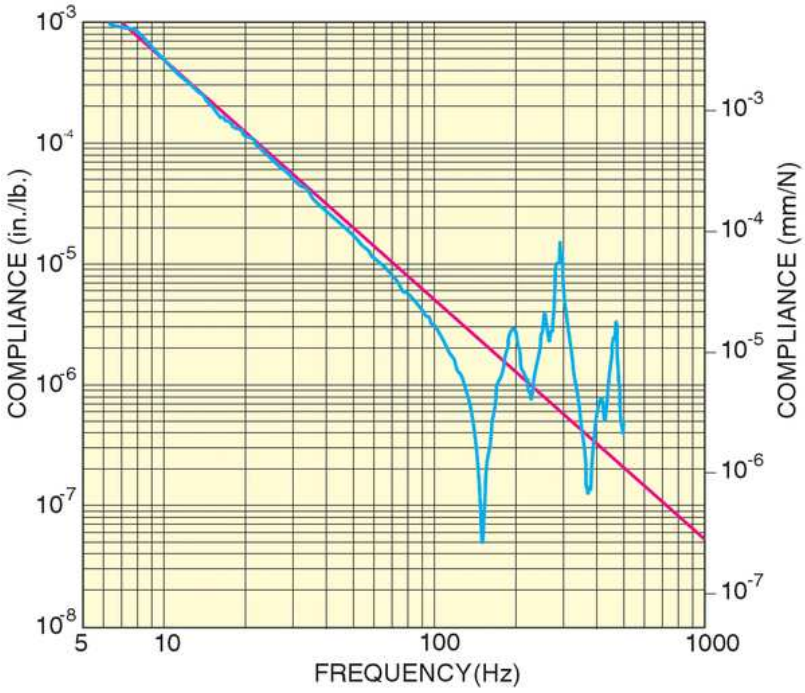

Figure 3.1: Compliance (displacement of a loaded unit per unit load) for the *Newport 2000 Optical Table*, from [32].

the two diodes are subtracted electronically the laser noise features shared by both beams are canceled out. In order to test the effectiveness of the just described method the noise spectrum of a *Coherent Regenerative Amplifier* (*RegA*) was recorded through a *HP3561A* Signal Analyzer. A $\approx$ 5mW beam centered at 800nm was split into two beams: one was transmitted through a 5mm thick $KTaO_3$ sample and then directed to the "signal" port of a balanced silicon photo detector, while the other was sent first through a neutral density filter, necessary to zero the photo detector output voltage, and then to the "reference" port of the detector. A sample was included in this test setup to gain a better insight into what the noise in a realistic experiment looks like. The noise spectral density in the balanced and unbalanced configuration was measured by the Signal Analyzer connected to the output port of the detector (see Fig. 3.2). The benefit of using a balanced detection scheme is quite evident and results in about one order of magnitude reduction of the noise floor over the entire frequency range measured. It is curious to notice how the balanced spectrum in Fig. 3.2 is not simply an attenuated duplicate of the unbalanced case. The new features, clearly noticeable, are most likely due to the sample that, as noted above, is itself a source of noise. Along this line, it should be pointed out now that the choice of some of the noise

controlling settings (integration time, number of average scans, dynamic reserve) has always been very dependent on the specific sample under test.

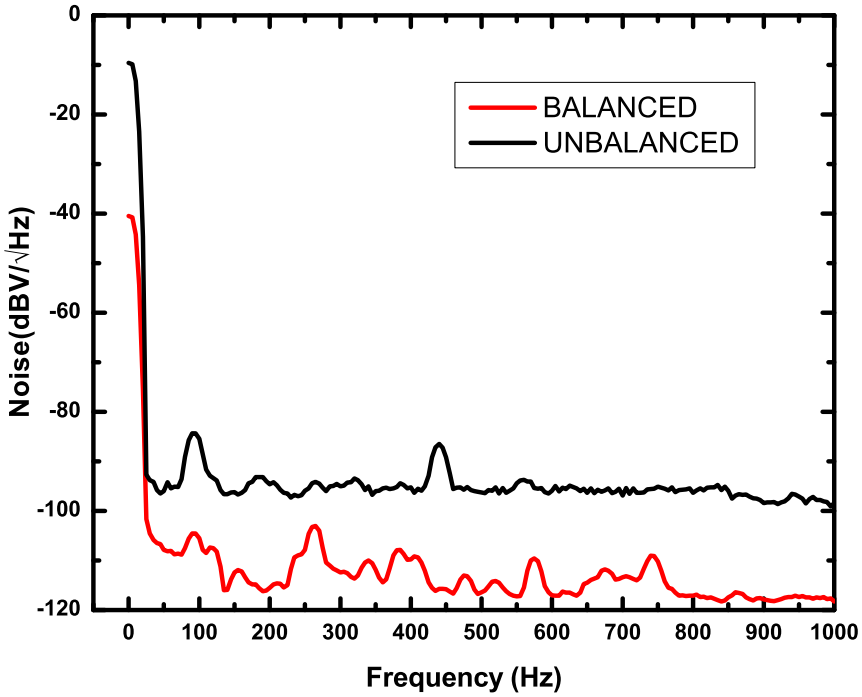

Figure 3.2: Noise spectral density in balanced and unbalanced detection.

The noise arising from the electronic devices making up our detection setup is the last one to be addressed. In the noise spectrum shown in Fig. 3.3 three different components can be identified: flicker or $1/f$ noise, dominant at low frequencies; white noise kicking up once the $1/f$ noise fades; and the power line harmonics at integer multiples of 60Hz [33]. The $1/f$ noise is in great part attributable to the laser and can be, at least partially, reduced through balanced detection (see Fig. 3.2). In a passive circuit the electronic noise can usually be classified into two categories: shot noise (or Schottky noise) and thermal noise (or Johnson noise). Shot noise is due to the randomness in the number of carriers that flow through a photodiode p-n junction and is characterized by the following current spectral density [34]:

$$S_I = 2qI = 2q(R \cdot P) \tag{3.1}$$

here q is the electronic charge while I is the diode current, i.e. the product of the diode responsivity (R) and the incident power (P).

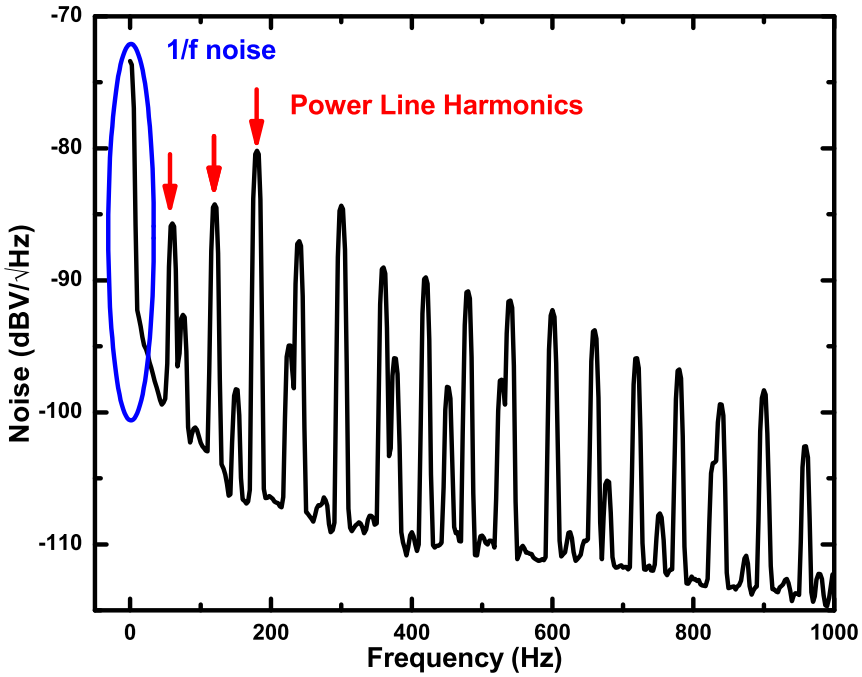

Figure 3.3: Noise spectrum of the *Coherent Regenerative Amplifier*.

Thermal noise, on the other hand, is caused by the thermal fluctuations of carriers inside a conductor and is defined, for a resistor of value R, by the following current spectral density:

$$S_T = \frac{4k_B T}{R} \tag{3.2}$$

k_B is the Boltzmann constant, T the temperature in degrees Kelvin. There is a fundamental difference in the two power densities just introduced: the shot noise is directly affected by the signal power (I), while the thermal noise is just an intrinsic property of a specific electronic component. In order to develop an effective noise reduction strategy, it is key to determine what is the predominant nature of the electronic noise and this is easily accomplished studying the spectral density dependence on the laser intensity. In Fig. 3.4 the power density at 800Hz (far away from the $1/f$ region and from any of the power line harmonics) is shown for five different values of the laser power in a very simple case: resistor (10kΩ) and silicon photo diode (see Fig. 3.5-A). As the incoming beam intensity changes the noise power is neither constant (consistent with Eq. 3.2) nor is it a linear function of the laser power (in accordance with Eq. 3.1). The experimental data are then affected conjunctively by thermal and shot noise and hence both of them have to be taken into

account.

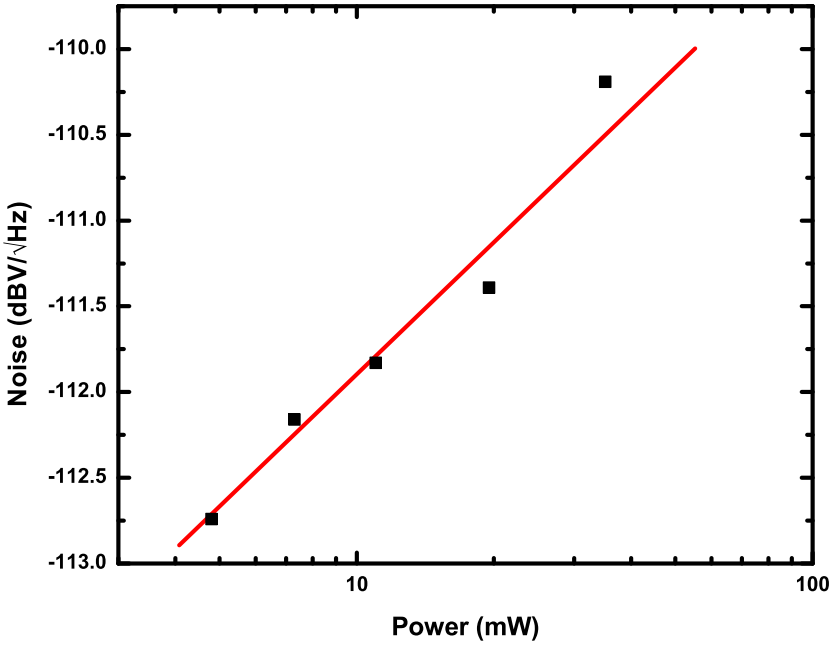

Figure 3.4: Noise Power Density dependence on the laser beam power.

3.2 Detector

Getting acquainted with the noise features allows us to define the guidelines followed when building the photo detectors used in our experiments. Since the photo diodes were always operated in current mode, from a circuit viewpoint our detectors functioned as current to voltage converters, i.e. they acted like a resistor. Fig. 3.5-A shows the most basic type of this kind of detector: a photodiode in parallel with a resistor of value R. The resistor value was chosen to minimize the SNR, computed with the aid of the noise equivalent circuit shown in Fig. 3.5-B, where I_S is the current generated by the photo diode, I_N the shot noise current density (see Eq. 3.1) and $I_R = 4k_BT/R$ is the thermal noise produced by the resistor. The SNR can be written by gathering all the different contributions:

$$SNR = \frac{I_S^2}{(2qI_S + 4k_BT/R) * \Delta f} \tag{3.3}$$

where Δf is the bandwidth of the circuit.

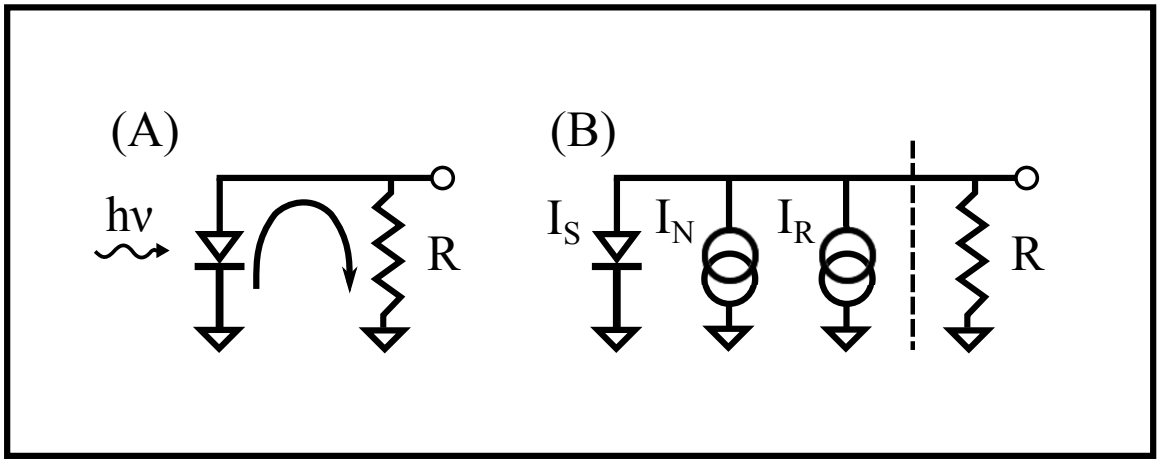

Figure 3.5: (A) Passive current to voltage converter. (B) Noise equivalent circuit.

According to Eq. 3.3 the SNR can be boosted both by increasing I_S and making R larger. As already noted in the previous section, I_S is proportional to the laser power which is limited by the damage threshold of the samples under test or by the specific nature of the experiment performed (too much power can, for instance, drive a phonon mode out the linearity range, see Chap. II). In general, provided that these limits are not exceeded, it is always a good policy to use as much power as possible. There are limitations on the maximum value of R as well since, if the voltage drop across the resistor gets too high, the diode will start working in forward mode and consequently V_{OUT} will no longer be linearly related to the incident power [35]. To optimize the SNR within the just mentioned constraints two different designs were developed. The first kind of detector, see Fig. 3.6-A, was assembled employing only passive elements: two silicon PIN photo diodes, *FDS100*, purchased from *Thorlabs* [36] were connected back to back and the difference current was injected into a $9.2k\Omega$ resistor. The *FDS100* featured the largest sensor area in a *TO-5* can and granted a $\simeq 0.5A/W$ responsivity at $800nm$. The chosen resistor value extended the detector linear range to about $400mV$ so that a reasonable compromise between gain and linearity was achieved. Since only passive components were employed in the scheme shown in Fig 3.6-A, this circuit turned out to be practically noise free and hence it was always the preferred choice whenever dealing with a signal surrounded by a strong noise background. It worked especially well when operated in a fully balanced configuration: zero average

voltage across the resistor.

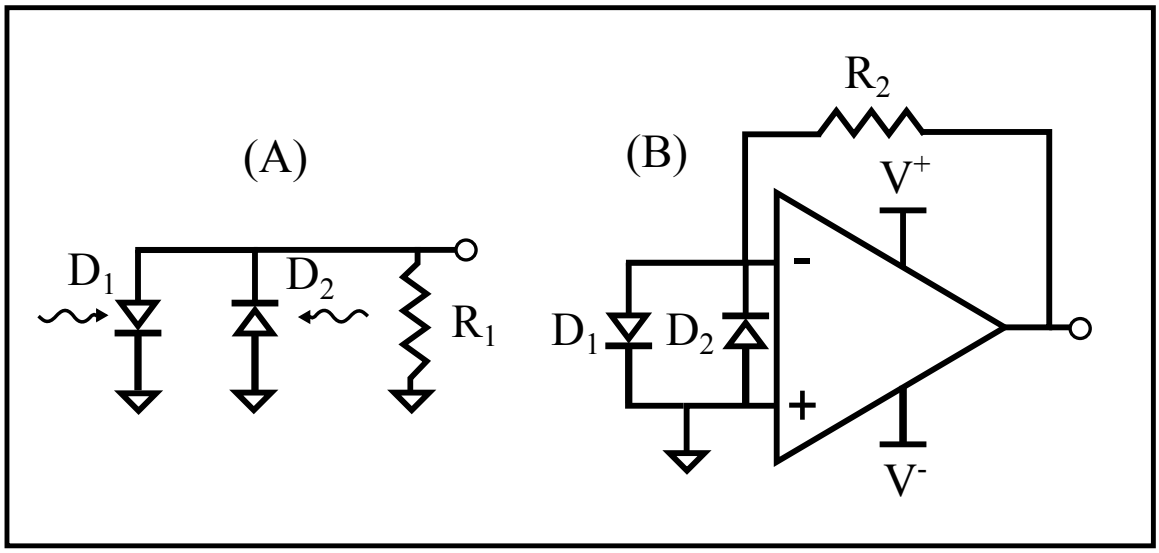

Figure 3.6: (A) Passive balanced detector (B) Transimpedance amplifier.

In order to improve even further the SNR without running up against the non linearity issue, a transimpedance amplifier [37] was used. Fig 3.6-B shows the standard layout of this circuit: two photo diodes (S6775 from *Hamamatsu*) were connected to a virtual ground pin (the negative OpAmp pin) so that the change in the voltage across R_2 did not affect the diode voltage bias. A TLO82 Dual BiFet OpAmp was used as a gain stage: this amplifier has a JFET (rather than a MOSFET) input stage and thus a better performance in terms of noise. The OpAmp was internally compensated and differentially biased through a power supply ($\pm$9V). To gain some extra flexibility, a $2\Omega - 2\text{k}\Omega$ potentiometer was used in place of R_2. Irrespective of the value of the feedback resistor the high Gain Bandwidth Product ($GBWP$) of the OpAmp (4MHz) guaranteed a large enough bandwidth to handle any kind of audio frequency modulation. The circuit in Fig. 3.6-B suffered from a higher noise floor than its passive counterpart due to the presence of the OpAmp, but could adapt to different signal intensity levels thanks to the variable gain and maintained an excellent linearity even when only one photodiode was illuminated.

3.3 Lock in amplifier

Detection constitutes only the first stage in the signal processing chain. This section is entirely dedicated to discussing the different techniques adopted to filter the noise and

amplify the signal measured by the photo detector. From Fig. 3.2 and Fig. 3.3 it is quite evident that the noise is more intense in the DC region of the spectrum (where the $1/f$ contribution dominates) and decreases significantly moving to higher frequencies. Since the signal of interest is also in the DC region this is particularly detrimental: any disturbance accompanying the signal can easily saturate the amplifying circuits leading to a forced choice between distortion and lower gain. The most suitable method to overcome this issue is heterodyne detection. The main idea behind this particular technique is rather simple: the useful signal is transferred away from the $1/f$ area to a lower noise region (through some kind of modulation technique), it is amplified and then brought back to DC through a digital or analog mixer where a final filtration and amplification takes place. Separating the signal from the $1/f$ noise makes it possible to selectively amplify the former and attenuate the latter so that only the white noise (shot and thermal) present around the modulating frequency affects the final output signal. Heterodyne detection is practically implemented by lock-in amplifiers. Rather than embarking into a lengthy technical discussion about lock-ins, a brief overview will be given of the instrument's different components [38], see Fig. 3.7, trying to highlight the impact that each one has on the overall SNR.

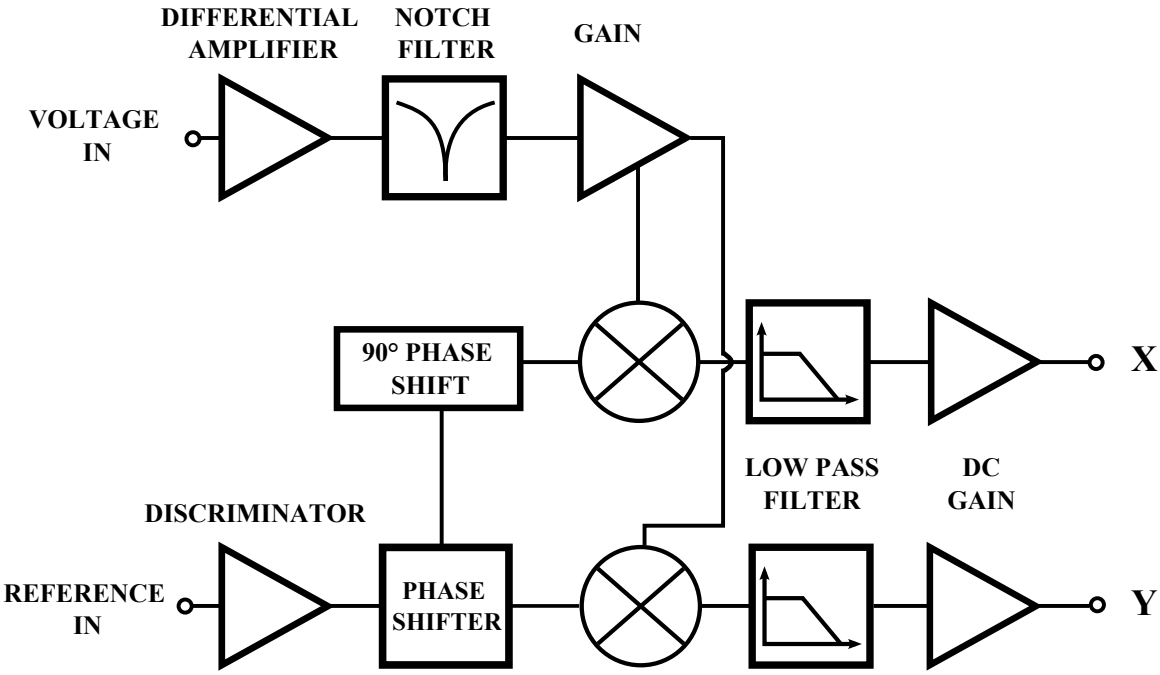

Figure 3.7: Lock in amplifier schematic diagram, from [38].

The lock-in circuit is split into two separate arms: the signal and the reference. As already

anticipated, the signal, in our case the laser beam, is somehow modulated upstream before getting into contact with the noise sources. The reference signal is generated by the same device that modulates the signal (a chopper, for instance) and the lock-in records the frequency and phase of the modulating signal for use in the down conversion stage. Focusing first on the signal side, it can be observed that the amplification is performed via three separate stages: two of them located before the mixer, when the signal is still modulated and one after, when the signal has already been converted back to DC. The lock-in available in our lab (*SR830* by Stanford Research System) allows one to set both the overall gain of the amplifier (the product of the gain of the individual blocks) and the distribution of the gain before and after the mixer (dynamic reserve). In general it is good practice to keep the dynamic reserve LOW so that the signal is mostly amplified before the mixer: delaying the amplification too much can make the internal lock-in noise no longer neglectable. However, sometimes the noise floor at the lock-in input is so high that it would cause the first two gain stages to saturate unless their gain is reduced. In this case it is only possible to raise the signal amplitude to the desired value after the low pass filter, when the noise is significantly attenuated. This shift in amplification stage is accomplished by raising the dynamic reserve to a higher setting. In general, the dynamic reserve was kept on LOW unless the laser was malfunctioning or the sample surface was damaged.

The first block encountered in the reference signal arm is a phase shifter. This device, connected to the mixers, controls the phase of the demodulating sinusoidal signal and thus regulates the amount of signal transfered to the X output (component of the input signal in phase with the reference) and the Y output (component of the input signal in quadrature with the reference). It is crucial to identify in each experiment the value of the reference phase that minimizes disturbances; the useful signal is, in fact, often accompanied by slowly decaying backgrounds associated with various perturbing phenomena (e.g. recombination of photo excited electrons) that take place in the sample under test. Through a careful choice of the phase value, the useful signal can be locked to one channel (typically X) and all the additional interference signals moved to the other one (typically Y). Even in the complete absence of interference signals, the reference phase should be used to make sure that the signal is entirely transfered to only one channel: if this were not the case, in order

to recover the full signal amplitude, both channels should be processed ($R = \sqrt{X^2 + Y^2}$) doubling the noise content of the final output.

The last functional block to be addressed is the low pass filter: this stage is responsible for eliminating the high frequency components of the spectrum once the signal has been shifted back to DC. This operation is equivalent to a time domain integration and the low pass filter bandwidth coincides approximately with the inverse of the integration time: narrow bandwidth is equivalent to longer integration time. Since the signal has been translated to high frequency and then moved back to DC, the low pass filter acts effectively as a band pass filter centered at the modulation frequency and this is, in some sense, the key signature of a lock-in: filtering and amplifying a very narrow band at high frequency by means of a low pass filter. Needless to say, it is critical to carefully choose the integration time according to the specific experimental conditions. A long integration time averages out a consistent fraction of noise but increases the time required to complete a scan: drifts in the laser power, temperature and humidity can induce a signal change within the same scan introducing distortion and making it more challenging to recover the desired features. Hence, a single scan should never exceed a few minutes: the higher noise level can be reduced by averaging out multiple scans.

3.4 Amplitude and phase modulation

As pointed out at the beginning of this section, heterodyne detection requires that the signal is somehow modulated before it reaches the sample and is detected by the photo diodes. There are basically two ways of doing this: modulate the amplitude [39] or the phase [40] of the laser beam. Amplitude modulation is easily performed through any kind of device that modifies the laser intensity in a periodic fashion. The most common choice is usually a mechanical chopper (a rotating wheel with equally spaced blades), capable of modulating the signal from a few Hz up to about 3kHz. Phase modulation, in contrast, is commonly attained by varying the laser pulses arrival time at the sample. It turns out that, by doing so, the signal fed into the lock-in is the derivative of the original signal. In order to elucidate this concept, let's imagine that the measured signal has an amplitude (A) dependent on the relative time delay between the pump and the probe beam (δ), as

depicted in Fig. 3.8. The probe path length can be adjusted, for instance, by moving one of the mirrors in the probe path back and forth at frequency ω_M in such a way that the pump probe-delay becomes an oscillatory function:

$$\delta = \Delta cos(\omega_M t) \tag{3.4}$$

here Δ is the shaker stride divided by the speed of light. If Δ is much shorter than any of the signal features, $A(\delta)$ can be expanded in a Taylor series truncated at the first order:

$$A(\delta) \simeq A(\delta_0) + \left.\frac{dA}{d\delta}\right|_{\delta=\delta_0} \Delta cos(\omega_M t) + O(\delta) \tag{3.5}$$

where δ_0 is the delay between pump and probe when the moving mirror is at rest. If the lock in reference frequency is set to ω_M, the output will be proportional to the signal derivative computed at δ_0.

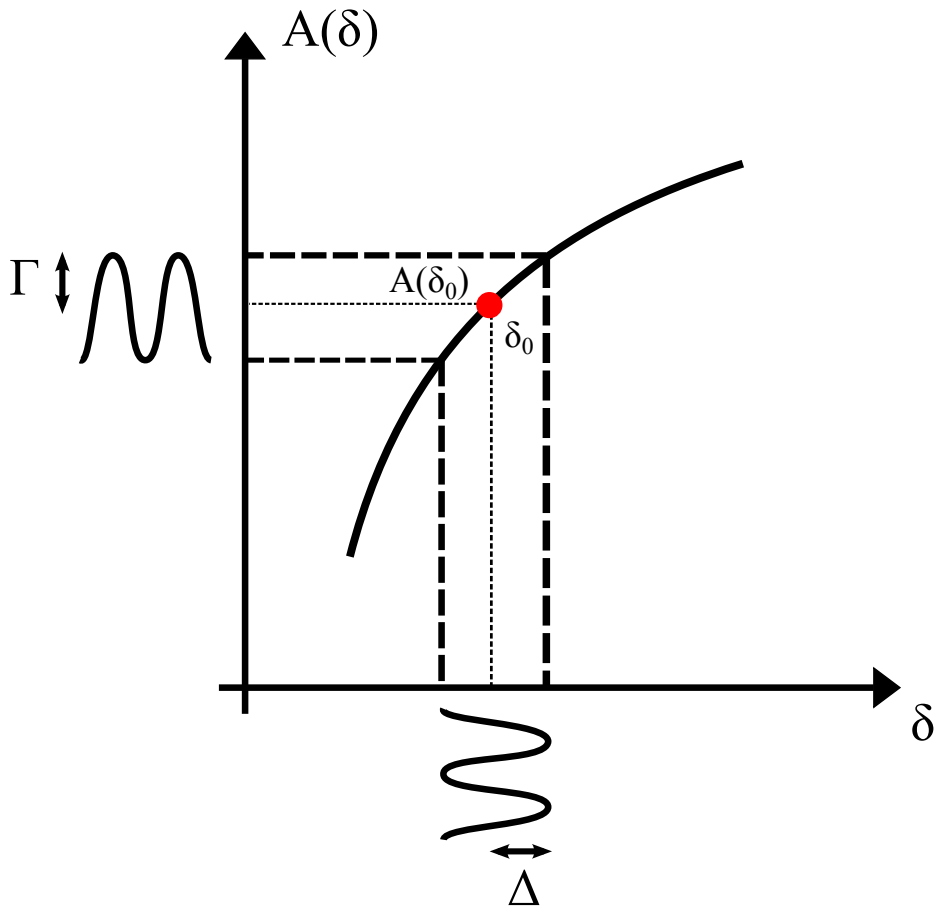

Figure 3.8: Phase modulation.

To better appreciate the peculiarities of these two approaches, their advantages and drawbacks will be compared. The main benefit of phase modulation lays in its offset cancellation capability. This is especially advantageous when the signal of interest is mixed with a spurious, slowly decaying interference: computing the derivative will remove any low frequency component in the spectrum and deliver a background free signal, see Fig. 3.9.

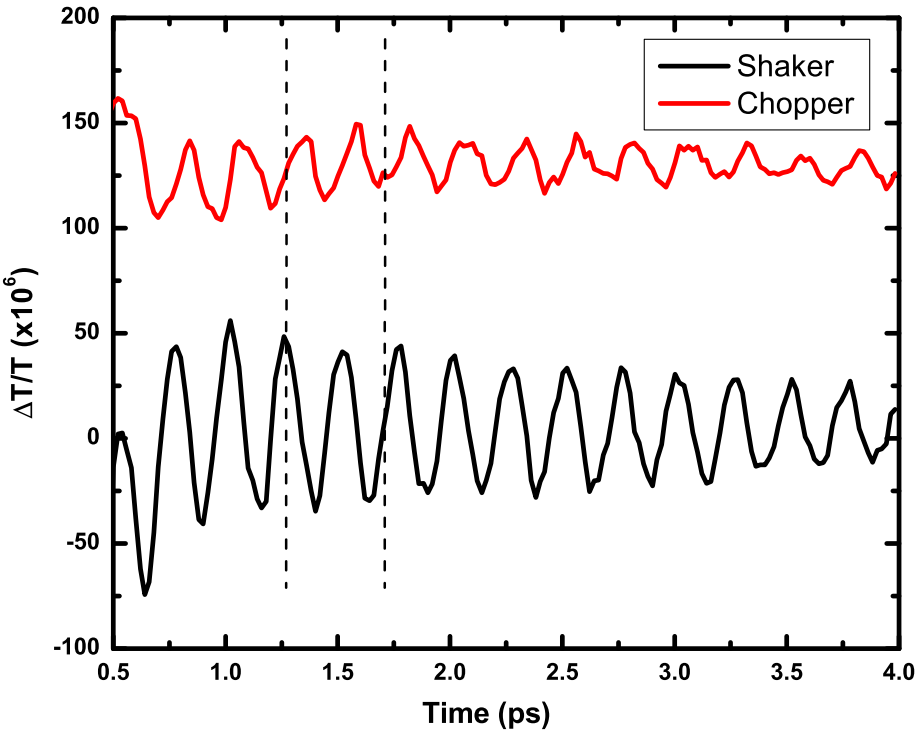

Figure 3.9: Differential transmittance through a $\simeq 50\mu m$ thick GaSe sample at $514nm$ measured by amplitude and phase modulation techniques.

It could be objected that the same result can be accomplished by numerically differentiating the digitized signal trace. Yet, if the derivation is not performed in real time, any DC offset enters the lock-in and tends to saturate it unless the gain is reduced with substantial repercussions on the SNR. In addition, once the signal is hidden underneath a very large background, the optimization process becomes very cumbersome because the effect of any change in the setup or the alignment is barely noticeable on the signal amplitude. The great potential of the phase modulation technique is fully expressed in another recurrent

experimental context: a weak signal superimposed onto other stronger, lower frequency sinusoids. As already pointed out in Chap. II, the amplitude of a vibration decreases exponentially with its frequency ($e^{-\Omega^2\tau_L^2/2}$), hence the higher frequency modes are usually the most difficult to measure. Since the derivative of a sinusoid is proportional to its angular frequency, a phase modulation approach will favor high frequency modes at the expense of slowly varying oscillations. The drawbacks of this technique are related to the mechanical handicap of the shaker used to change the beam path: namely the fact that the shaking frequency cannot exceed a few hundred Hertz. With such a low carrier frequency the rejection of the $1/f$ noise can be very poor unless the time constant is increased significantly at the price of a longer measurement time. An additional potential complication deserves a mention: the shaker vibrations can couple to the table mechanical resonances, see Fig. 3.1, and degrade the SNR considerably. Amplitude modulation does not suffer from these limitations: a mechanical chopper can modulate the signal up to 3kHz, does not couple mechanically to the optical table and is not as bulky as a shaker (and its mount) so it can be accommodated even in very crowded setups. This technique's main drawback resides in the inability to reduce high backgrounds and, for this reason, falters whenever the desired signal is buried into a much stronger, slowly drifting offset.

3.4.1 Special techniques

Before concluding this section, it is worth adding a quick note about possible variations on some of techniques so far described. Since the shaker can be driven by a square or triangle wave rather than a sine wave it is possible to lock the amplifier to one of the harmonics rather than to the fundamental frequency fed into the reference channel. In this way, the modulation frequency can be increased way above the noisy $1/f$ region. The price to pay is a reduced signal intensity due to the smaller amplitude of the harmonics compared to the fundamental frequency as indicated in Eq. 3.6 for the case of a square wave of period $2L$ [41]:

$$S(x) = \frac{4}{\pi} \sum_{n=1,3,5,\ldots}^{\infty} \frac{1}{n} sin\left(\frac{n\pi x}{L}\right) \tag{3.6}$$

Relying on the fact that it is possible to selectively lock to the harmonics of the reference signal, in some experiments the pump was chopped and the probe shaken. In order to do so,

the sync signal, at frequency ω_M, provided by the signal generator controlling the shaker, was used to drive the chopper at frequency $n \cdot \omega_M$, n being just an integer number. Since the ISRS signal depends on the product of the pump and probe intensity, it contains both the sum and the difference of the chopper and shaker frequencies:

$$Y(t) \propto I_{PROBE} \cdot I_{PUMP} \propto cos[\omega_M t] \cdot cos[n\omega_M t] = \frac{cos[(n-1)\omega_M t] + cos[(n+1)\omega_M t]}{2} \quad (3.7)$$

The signal at the frequency sum can be retrieved by setting the lock-in reference to the $(n+1)^{th}$ harmonic. Besides increasing the carrier frequency, this approach offers the additional advantage of making the lock-in insensitive to those signals that contain only the pump or the probe modulation, a trenchant strategy to immunize the detection scheme from any scattered pump beam that may leak into the detector.

3.5 Experimental setups

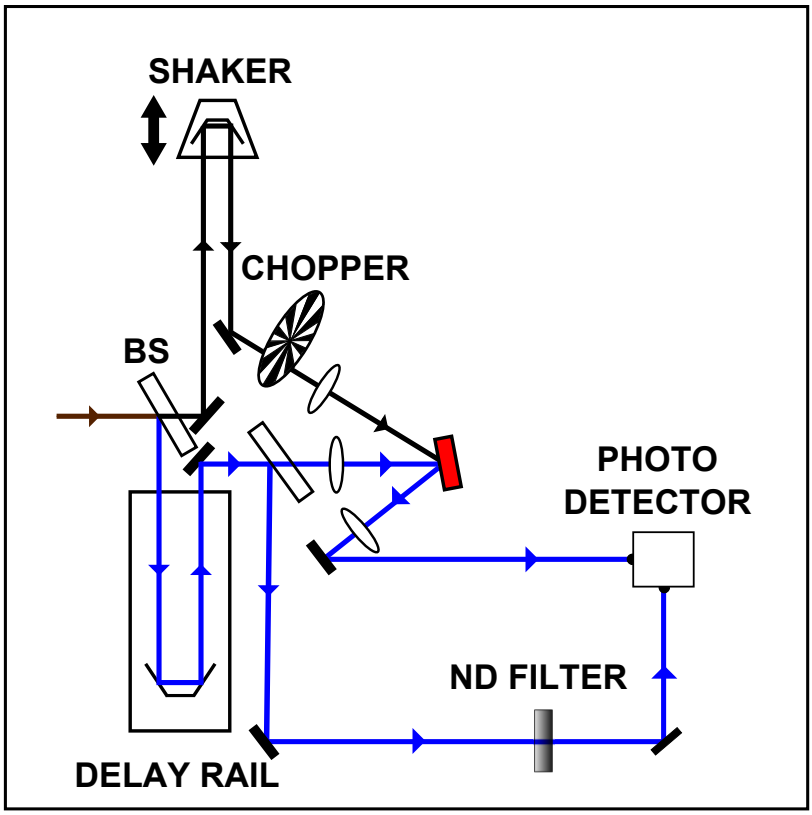

Figure 3.10: Reflection pump-probe setup with standard balanced detection.

This section is intended to briefly describe the different setups I employed to collect the pump-probe data presented in this dissertation. The experiments performed can be divided into two groups: reflection, Fig. 3.10 and transmission, Fig. 3.11. In both cases the pump and the probe beams were focused on the sample through a 125mm and a 100mm double-convex lens respectively. This choice of the focal lengths resulted in corresponding spot sizes of $\simeq 25\mu$m and $\simeq 15\mu$m. The two beams converged at the sample at $\simeq 20°$ and were about 10° off from normal incidence, so that, accounting for the refraction taking place at the interface, they propagated almost collinearly inside the sample.

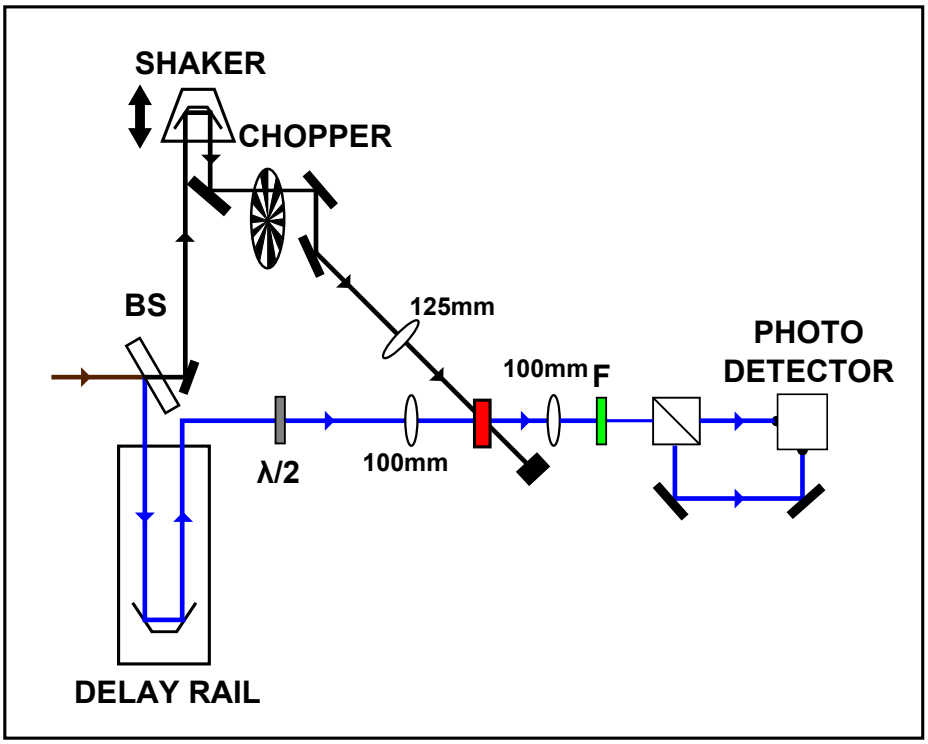

Figure 3.11: Transmission pump-probe setup with polarization sensitive detection.

The reflection signal was sent straight to the detector, while the transmitted beam was filtered by an interference band pass filter (labeled F in Fig. 3.11) to spectrally resolve the probe and enhance the pump induced signal [19].

Two detection schemes, i.e., the setup part following the sample, were adopted and referred to here as standard balanced detection (Fig. 3.10) and polarization sensitive detection (Fig. 3.11). In the former, the probe is split into two beams, one is sent to the sample and then to the "signal" port of the detector while the other is sent directly to the "reference"

port of the detector. The neutral density filter (label ND in Fig. 3.11) is needed to equalize the intensity of the two beams and maximize the benefits of balanced detection. The polarization sensitive setup [42, 43] is particularly useful when the signal to measure contains two components (e.g. two phonon modes): a weaker mode whose intensity is dependent on the angle ϕ between the pump and probe electric field polarization and a stronger mode unaffected by the polarization of either beam. If the difference in the modes strengths is pronounced, the weak mode is completely obscured by the strong one.

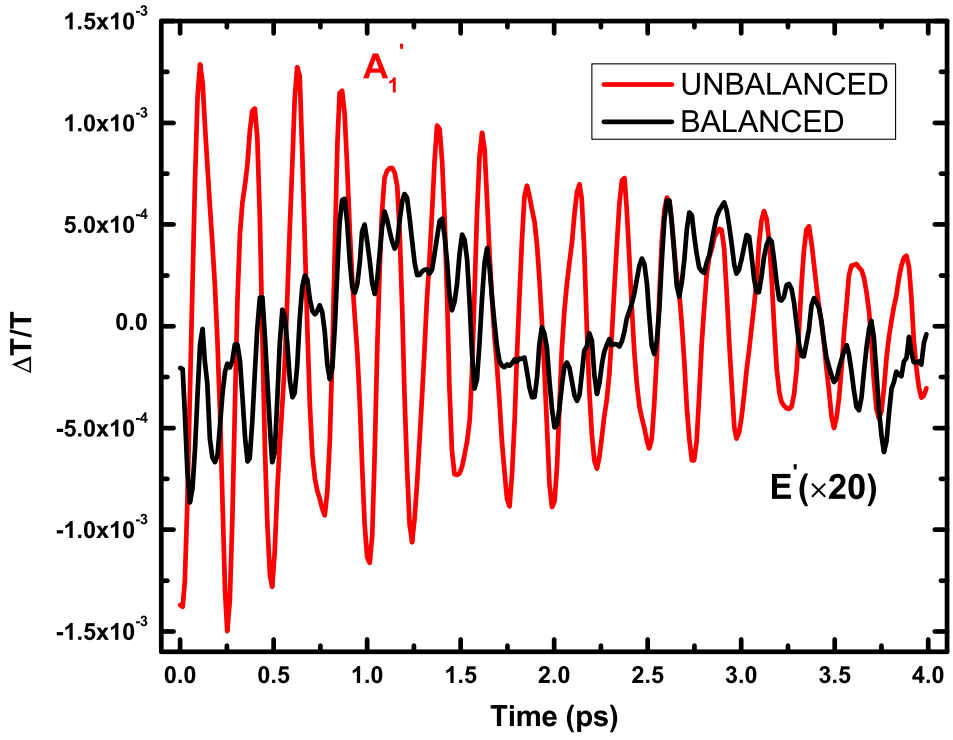

Figure 3.12: $A_1^{'}$ and $E^{'}$ modes in GaSe measured at $800nm$ using the polarization sensitive setup, Fig. 3.11. The $A_1^{'}$ mode is the only one visible when one detector port is blocked (red line), while it is almost completely canceled when both ports are open (black line).

If the non isotropic mode intensity is proportional to $\cos(2\phi)$, as it happened in several of the samples presented in this dissertation, the $\phi = 0$ and $\phi = 90°$ components have the same intensity but opposite sign. In order to measure the weaker mode, ϕ should be set to 45° using a half wave plate so that the $\phi = 0°$ and $\phi = 90°$ components can be separate after the sample through a cube beam splitter (see Fig. 3.11) and electronically subtracted one from

the other via the balanced detector. This approach does not ultimately affect the intensity of the weaker mode, but completely cancels out the isotropic one. To better appreciate the advantages offered by the detection scheme shown in Fig. 3.11, it was tested on a GaSe sample. GaSe is the ideal candidate since its phonon spectrum includes two optical phonon modes that can be measured by pump-probe: $A_1^{'}$, 6.3THz, isotropic and $E^{'}$, 0.6THz, whose intensity depends on $\cos(2\phi)$. Fig. 3.12 shows the signal measured when $\phi = 45°$ and only one detector port or both are open: in the first case there is no cancellation effect and only the $A_1^{'}$ mode is evident, in the second the cancellation can take place and the predominant frequency is the $E^{'}$. It is worth mentioning that the effectiveness of the just described scheme is heavily dependent on the birefringence of the sample: if the probe polarization is scrambled or rotated by the sample the isotropic mode leakage may be considerable and the cancellation is only partial.

3.6 Pulse width measurement

A crucial parameter to constantly monitor in any ultrafast time domain experiment is the width of the laser pulses. The duration of the individual pulses, in fact, ultimately determines the achievable resolution which, in the case of optical excitation of coherent phonons, defines the highest detectable frequency. Yet, this is not the only reason why it is vital to accurately measure the laser pulse width. Since in our setups there are inevitably dispersive elements (lenses, filters, polarizers) it is necessary to compress the pulse width [44, 45] in order to compensate for the added chirp: a reliable pulse measurement device is required to properly adjust the settings of the pulse compression apparatus (prism pair or gratings). Moreover, even when the pulse width is short enough to observe the desired phenomenon, it is still critical to know the exact width value to correctly interpret the experimental data and to compare them with the theoretical predictions. To this regard, an instructing example is the dependence of a coherent phonon amplitude on the laser pulse width [46], already discussed in Chap. II. Three main techniques were employed to measure the pulse width: Sum Frequency Generation (SFG), Two Photon Absorption (TPA) and Frequency Resolved Optical Gating (FROG); each one will be shortly described throughout the rest of the chapter.

3.6.1 Sum Frequency Generation

When two beams at frequency ω_1 and ω_2 are focused on a crystal exhibiting second order non linearity, $\chi^{(2)} \neq 0$, a non linear polarization, P, is generated [47]:

$$P(\omega_1 + \omega_2) = 2\epsilon_0 \chi^{(2)} E_1 E_2 \tag{3.8}$$

where E_1 and E_2 are the electric fields of the two incident beams. Hence, when two sufficiently energetic beams with the same frequency ($\omega_1 = \omega_2 = \omega$) propagating along $\mathbf{k_1}$ and $\mathbf{k_2}$ travel through a second order non-linear crystal a third beam emerges from the sample. Its frequency and wave vector are forced by the conservation of energy and momentum (see Fig. 3.13) to be:

$$\begin{aligned} \omega &= 2\omega \\ \mathbf{k} &= \mathbf{k_1} + \mathbf{k_2} \end{aligned} \tag{3.9}$$

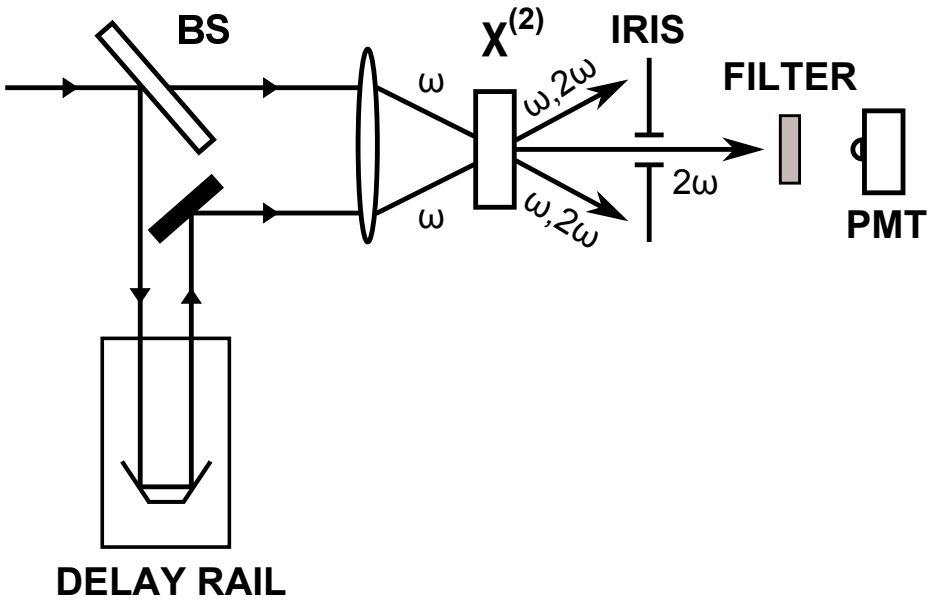

Figure 3.13: Autocorrelator.

As opposed to the two rays, at ω and 2ω, that exit the sample parallel to the incident ones, the $\mathbf{k} = \mathbf{k_1} + \mathbf{k_2}$ beam is generated only if the incident beams overlap on the crystal both spatially and temporally, hence the insertion of a translation stage that can adjust the time delay between the beams. The setup in Fig. 3.13, commonly known as an autocorrelator,

is also equipped with an iris to select only the frequency sum beam, a short pass filter to attenuate any residual radiation at ω and a Photo Multiplier (PMT), especially necessary when the second harmonic frequency falls in the UV range. Naming t' the time delay introduced by the translation stage, the intensity of the detected beam is given by [48]:

$$I(t') \propto \int I_1(t) I_2(t - t')\, \mathrm{d}t \tag{3.10}$$

where I_1 and I_2 are the intensities of the beams incident on the second harmonic crystal. Since the temporal profile of I_1 and I_2 is the same, Eq. 3.10 just constitutes the convolution of the laser pulse with itself. In the case of a Gaussian pulse with standard deviation σ:

$$I_1(t) = I_2(t) \propto e^{-\frac{t^2}{2\tau^2}} \tag{3.11}$$

the convoluted pulse is:

$$I(t) \propto e^{-\frac{t^2}{4\tau^2}} \tag{3.12}$$

Using Eqs. 3.11 and 3.12 the actual pulse width, τ_p, can be related to the autocorrelation width, $\tau_{AC} = 2\tau\sqrt{ln2}$:

$$\tau_p = \frac{\tau_{AC}}{\sqrt{2}} \tag{3.13}$$

Eq. 3.13 is rigorously correct only in the case of a Gaussian beam. Despite the uncertainty about the real pulse shape, the correction indicated in Eq. 3.13 has always been preferred to other options (e.g. $0.315\tau_{AC}$ coming from a Sech^2 approximation of the pulse).

The intensity of the signal generated in an autocorrelation experiment depends on the sample thickness (ΔL) and phase matching $|\mathbf{k_1} + \mathbf{k_2} - \mathbf{k}|\Delta L \sim 0$. Phase matching is usually met by exploiting birefringence and, hence, requires the non linear crystal axes to be oriented properly relative to the incident radiation [49]. Even though a thicker sample (i.e. a greater volume of active material) would, in principle, generate a stronger signal, phase matching is more easily achieved in thin samples $\frac{\Delta L}{L} << 1$. Given the difficulties in accurately orienting a second order crystal, phase matching is usually the most stringent constraint. As a result, a $\sim 50\mu$m thick $\beta - \mathrm{BaB_2O_4}$ (BBO) crystal was used when measuring the weak output (< 80mW) of the visible Optical Parametric Amplifier, whereas a ~ 0.5mm

thick BBO crystal was preferred when measuring the Coherent RegA amplifier, capable of generating up to 1.1W. Both the BBOs were glued on a rotation mount so that they could be oriented to meet the proper phase matching angles. The most obvious disadvantage that an autocorrelator presents is its relative complexity, due mainly to the number of optical components needed and the consequent alignment involved, see Fig. 3.13. In addition to that, since the only physical parameter measured is the intensity, no information is recovered about the phase of the electric field and thus the type of chirp affecting the laser pulses.

3.6.2 Two Photon Absorption

A clever way to make the bulky setup in Fig. 3.13 more compact would be to incorporate the non linear medium and the photo detector into the same device. This approach has been practically implemented in what is usually referred to as *Two Photon Absorption*. Standard semiconductor detectors [50] operate by converting photons with energy greater than the band gap into electron-hole pairs. If the energy of the incident photons falls below the gap but exceeds half the band gap energy ($2h\nu > E_{GAP}$), see Fig. 3.14-A, it is still possible to generate free carriers in the conduction and valence band if two photons are simultaneously absorbed [51, 52]. When two pulsed laser beams are focused on the same semiconductor photo diode the two photons absorbed can come from the same beam but also from the two different beams provided that they are overlapped temporally. So, in addition to a constant background, a small photo current spike arises whenever the pulses "mix" in the semiconductor.

The detector built in our lab was made up of a *Hamamatsu* GaAsP photo diode whose responsivity curve is shown in Fig. 3.14-B. GaAsP is an ideal candidate for a Ti:Sapphire laser (780nm − 820nm) [55] since it absorbs around 400nm but it is almost completely blind at 800nm. Hence, the detector is insensitive to the main laser radiation that needed to be filtered out in the autocorrelation set up (see Fig. 3.13). Since phase-matching is not an issue here and the signal of interest is generated and measured in the same medium, the only alignment required consists in overlapping the beams at focus on the GaAsP crystal. A small inconvenience is caused by the fact that the two photon absorption signal may be very tiny (in the nA range) and, consequently, needs to be amplified before being processed

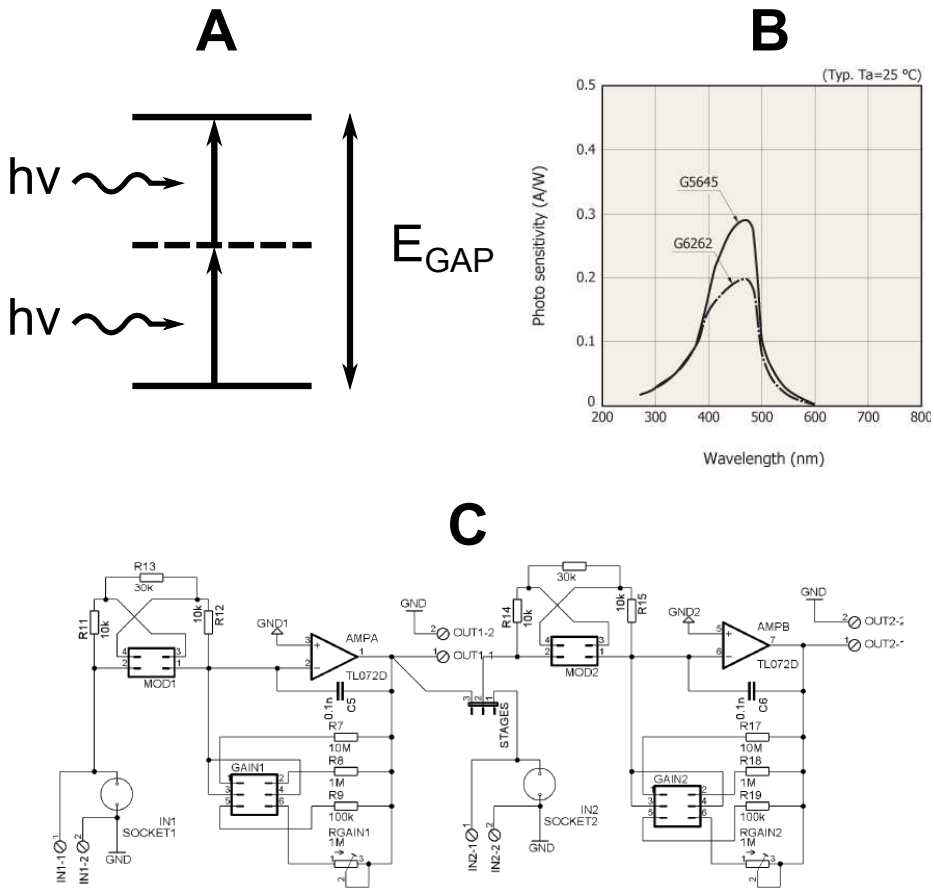

Figure 3.14: (A): two-photon absorption process in a semiconductor with band gap E_{GAP} (B): GaAsP spectral response, from [53] (C): 2-channel transimpedance amplifier board, from [54].

by the lock-in and the computer. Thus, the GaAsP photo diode has been connected to a variable gain amplifier board, purchased from *Boston Electronics* and shown in Fig. 3.13-C, which converts the photo current into a voltage signal and increases its amplitude to the desired value.

3.6.3 FROG

Neither the autocorrelator nor the two photon detector are capable of retrieving any information on the phase of the measured pulse and this is, sometimes, a serious limitation especially when trying to identify the best approach to compensate for chirp. Frequency-resolved optical gating takes care of this issue providing a 2D trace in which both time and frequency are recorded and displayed for real time observation of the pulse width and spectral width [56]. The basic idea behind this technique is to calculate the signal

spectrogram [57]:

$$S(\omega,\tau) = \left| \int_{-\infty}^{+\infty} E(t) g(t-\tau) e^{-i\omega t}\, \mathrm{d}t \right|^2 \tag{3.14}$$

where $E(t)$ is the electric field and $g(t)$ a gate function, see Fig. 3.15-A. Eq. 3.14 is just the Fourier transform of that portion of the electric field sampled at time τ by the function $g(t)$. Once $S(\omega,\tau)$ is known, it is possible to calculate both the intensity and the phase of the electric field [56].

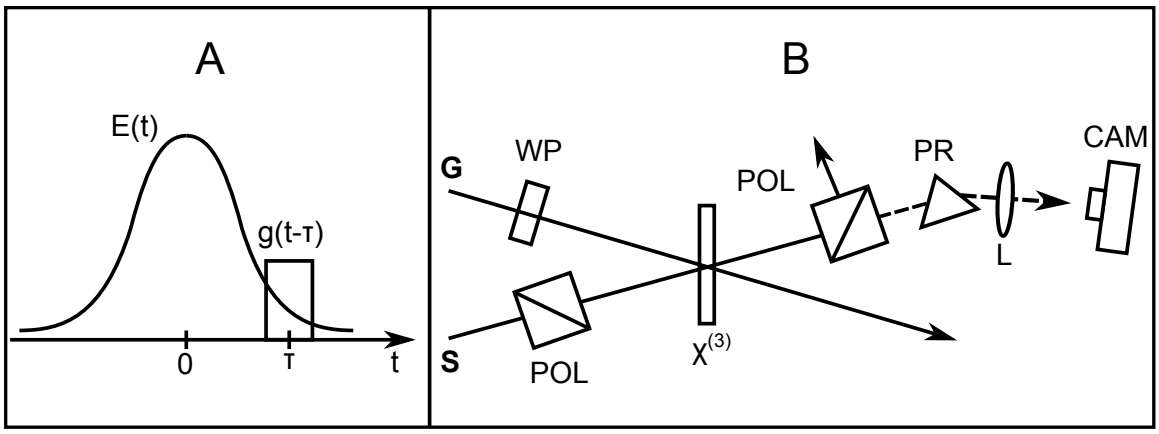

Figure 3.15: (A): spectrogram of the electric field function $E(t)$ (B): Polarization gate FROG, from [58].

Several alternatives are available to implement experimentally the spectrogram algorithm but only one will be discussed here: the polarization gate FROG sketched in Fig. 3.15-B. In this type of FROG the laser beam is transmitted through a beam splitter and sent to two separate paths, the signal (S in Fig 3.15) and the gate (G in Fig. 3.15). The gate beam polarization is set to $\pm 45°$ by a wave plate while its time delay (τ) is controlled by a delay stage similar to the one shown in Fig. 3.13 but not included in Fig. 3.15-B. Through the electronic Kerr effect the gate beam induces birefringence in a non linear crystal, $\chi^{(3)}$, so that when the signal beam, linearly polarized, goes through the crystal its polarization is slightly rotated. Only when the signal and gate beam overlap in time, does part of the transmitted signal beam go through the analyzer (cube polarizer located after the non linear crystal) and this is how the gating process is accomplished. The electric field of the signal beam is finally dispersed by a prism so that its spectrum can be collected by a CCD camera. Since the change in the refractive index induced by the Kerr effect is $\Delta n \propto |E_G|^2$,

the gate function $g(t-\tau)$ is proportional to $|E_G(t-\tau)|^2$ which, being a real quantity, does not perturb the phase of $E_S(t)$.

The FROG layout illustrated in Fig. 3.15-B works only when the two beams are properly aligned and requires expensive components (polarizers, wave plates, beam splitters) that operate usually in a narrow range of frequencies. Thus, this basic scheme has been improved throughout the years and modified to be more compact and easy to use. The FROG utilized in our experiments belongs to one of these upgraded versions of the polarization FROG relying heavily on the Transient Grating technique, and has been suggestively named GRENOUILLE (GRating-Eliminated No-nonsense Observation of Ultrashort Incident Laser Light E-fields). The particular model used is manufactured by Swamp Optics, operates in the $700-1100nm$ wavelength range and is able of retrieving $20-200fs$ pulses at $800nm$, [59]. The GRENOUILLE turned out to be particularly handy both to validate the autocorrelation measurements and to accurately align and tune the RegA stretcher and compressor gratings.

CHAPTER IV

Phonon Polaritons: theory and experiments

This chapter's focus is on the experimental activity carried out during the course of my PhD and its physical interpretation in light of the Raman scattering theory illustrated in Chap. II. The chapter is centered around the study of the interaction of electromagnetic radiation with polar lattice vibration modes, i.e. phonon polaritons. Relying on the mathematical formalism developed in Chap. II for purely mechanical phonons, the theory of phonon polaritons is introduced in Sec. 4.1 and extended to two particular cases: plasmon modes, Sec. 4.2, and surface polaritons, Sec. 4.3. The experimental part of the chapter aims at showing how Raman scattering proved to be a valuable tool to investigate these different polariton types in well known semiconductors: plasmon polaritons in GaAs, Sec. 4.5; phonon polaritons in GaSe, Sec. 4.6; and surface polaritons in CdSe, Sec. 4.7.

4.1 Phonon polaritons

4.1.1 Coupling of light to lattice vibrations: phonon polaritons

Interaction of light with matter can be adequately described once the optical properties of a solid medium are lumped into one frequency dependent operator: the dielectric constant, $\epsilon(\omega)$. The dielectric constant relates the electric field ($\mathbf{E}$) and the electric displacement ($\mathbf{D}$) [60]:

$$\mathbf{D}(\omega) = \epsilon(\omega)\,\mathbf{E}(\omega) \tag{4.1}$$

The expression of $\epsilon(\omega)$ can be exactly derived in simple prototypical cases like a cubic crystal with two ions per unit cell, having mass M^+ and M^- (see Fig. 4.1).

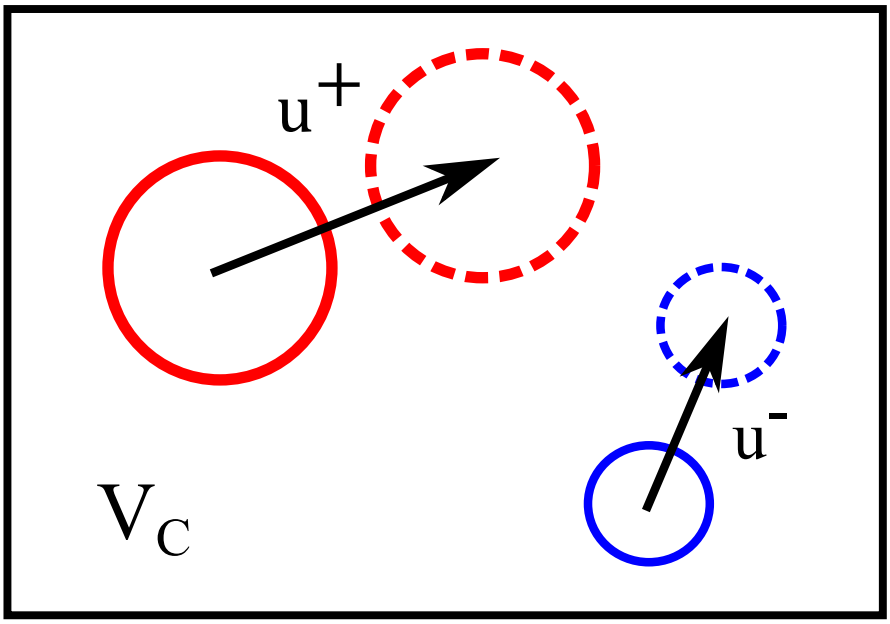

Figure 4.1: Anion, u^+, and cation, u^-, displacement in a unit cell of volume V_C.

Denoting by $\mathbf{u}^+$ and $\mathbf{u}^-$ the displacement of the two ions from their equilibrium position and introducing the reduced mass, $M_R = \frac{M^+M^-}{M^++M^-}$, the "effective" displacement $\mathbf{W}$ in the unit cell of volume V_C can be written as:

$$\mathbf{W} = \sqrt{\frac{M_R}{V_C}}(\mathbf{u}^+ - \mathbf{u}^-) \tag{4.2}$$

Hence, the dipole moment becomes:

$$\mathbf{P_D} = z^* e \sqrt{\frac{V_C}{M_R}} \mathbf{W} \tag{4.3}$$

where z^*e is the effective charge. The dipole moment expression is needed to define the energy of a crystal of volume V:

$$H = \frac{V}{2}(P_W^2 + \omega_{TO}^2 W^2) + \frac{1}{V_C}\int_V \mathbf{P_D}\cdot\mathbf{E}\,\mathrm{d}V + \int_V \mathbf{P_e}\cdot\mathbf{E}\,\mathrm{d}V \tag{4.4}$$

The Hamiltonian in Eq. 4.4 contains three major contributions: the potential ($\frac{1}{2}\omega_{TO}^2 W^2$) and kinetic ($\frac{1}{2}P_W^2$) energy of the ions; the interaction of the positively charged ions with the electric field, $\mathbf{P_D}\cdot\mathbf{E}$, and the interaction of the electrons with the electric field, $\mathbf{P_e}\cdot\mathbf{E}$.

ω_{TO} is the resonance frequency of the coupled ions system shown in Fig. 4.1 and coincides with the transverse phonon mode frequency [8]. $\mathbf{P_e}$ is the dipole moment of the electronic cloud:

$$\mathbf{P_e} = \frac{\alpha^+ + \alpha^-}{V_C}\mathbf{E} \tag{4.5}$$

Two different coefficients (α^+ and α^-) are required here to take into account the different response of the electron shell associated with the two ions in the unit cell [61]. It is natural to use $\mathbf{W}$ as the generalized coordinate and write down the Lagrange equation which, after some simplifications, reads:

$$\frac{d^2\mathbf{W}}{dt^2} = -\omega_{TO}^2\mathbf{W} + \frac{z^*e}{\sqrt{M_R V_C}}\mathbf{E} \tag{4.6}$$

Eq. 4.6 is coupled to the equation for the total dipole moment per unit volume $\mathbf{P} = \mathbf{P_D} + \mathbf{P_e}$:

$$\mathbf{P} = \frac{z^*e}{\sqrt{M_R V_C}}\mathbf{W} + \frac{\alpha^+ + \alpha^-}{V_C}\mathbf{E} \tag{4.7}$$

The solution to Eq. 4.6 and Eq. 4.7 can be found for a harmonic electric field ($\mathbf{E} \propto e^{i\omega t}$). Expressing $\mathbf{W}$ as a function of $\mathbf{E}$ using Eq. 4.6 and then inserting it in Eq. 4.7, an explicit relationship between $\mathbf{E}$ and $\mathbf{P}$ can be found:

$$\mathbf{P} = \frac{\epsilon(\omega) - 1}{4\pi}\mathbf{E} \tag{4.8}$$

with

$$\epsilon(\omega) = 1 + \frac{4\pi(\alpha^+ + \alpha^-)}{V_C} - \frac{4\pi(z^*)^2e^2}{M_R V_C\,(\omega^2 - \omega_{TO}^2)} \tag{4.9}$$

Eq. 4.9 can be rewritten in a more familiar form:

$$\epsilon(\omega) = \epsilon_\infty\frac{\omega^2 - \omega_{LO}^2}{\omega^2 - \omega_{TO}^2} = \epsilon_\infty + \frac{\omega_p^2}{\omega_{TO}^2 - \omega^2} = \epsilon_\infty + \frac{\epsilon_0 - \epsilon_\infty}{1 - (\frac{\omega}{\omega_{TO}})^2} \tag{4.10}$$

where

$$\begin{aligned} \epsilon_\infty &= 1 + \frac{4\pi(\alpha^+ + \alpha^-)}{V_C} \\ \epsilon_0 &= \epsilon_\infty + \frac{4\pi(z^*)^2 e^2}{(M_R V_C)\omega_{TO}^2} \\ \omega_p^2 &= \frac{4\pi(z*)^2 e^2}{M_R V_C} \\ \frac{\omega_{LO}}{\omega_{TO}} &= \sqrt{\frac{\epsilon_0}{\epsilon_\infty}} \end{aligned} \tag{4.11}$$

The last of the four equalities is commonly known as the *Lydanne-Sachs-Teller* (LST) equation. The choice to name ω_{LO} the frequency at which the dielectric constant vanishes will be explained later. Eq. 4.10 has been derived without considering losses which can be phenomenologically incorporated in our model adding a damping term to Eq. 4.6.

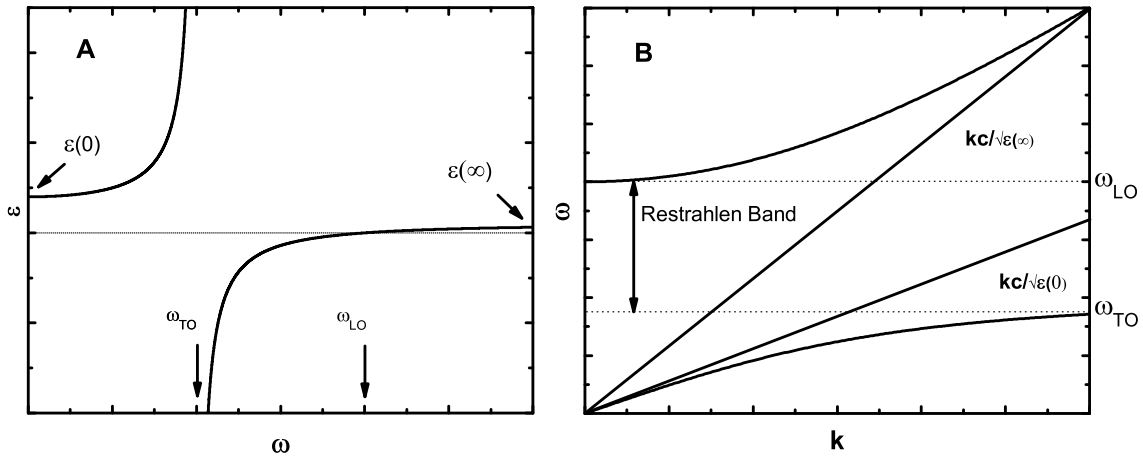

Figure 4.2: (A): Dielectric constant $\epsilon(\omega)$ as a function of frequency, see Eq. 4.10 (B): Phonon polariton dispersion relation.

To study the interaction of the lattice vibrations with the electromagnetic radiation it is necessary to introduce Maxwell's equations:

$$\nabla \times \mathbf{E} = -\frac{1}{c}\frac{\partial \mathbf{B}}{\partial t} \tag{4.12}$$

$$\nabla \times \mathbf{H} = \frac{1}{c}\frac{\partial \mathbf{D}}{\partial t} \tag{4.13}$$

The constituent relations are given by Eq. 4.1 and its counterpart for the magnetic field:

$$\mathbf{B}(\omega) = \mu(\omega)\,\mathbf{H}(\omega) \tag{4.14}$$

In principle both ϵ and μ should be tensors: they collapse to scalar coefficients only in the

case of isotropic materials, as the cubic crystal currently under examination. Since in the context of this work the focus is exclusively on the optical frequencies regime, the frequency dependence of μ can be safely neglected. The combined solution of Eq. 4.12 and Eq.4.13 can be found, in the case of a plane wave $e^{i(\mathbf{k}\cdot\mathbf{r}-\omega t)}$, by looking for the roots of the following equation:

$$\mathbf{k} \times [\mu^{-1}\mathbf{k} \times \mathbf{E}] + \frac{\omega^2}{c^2}\epsilon(\omega)\mathbf{E} = 0 \tag{4.15}$$

There are two allowed solutions:

- If $\mathbf{k} \parallel \mathbf{E}$, Eq. 4.15 can be satisfied only if $\epsilon(\omega) = 0$. Since in this case the electric field is parallel to the propagation vector, the solution is commonly referred to as the longitudinal mode. This mode oscillates, irrespective of the value $\mathbf{k}$, at only one frequency: ω_{LO}.

- If $\mathbf{k} \perp \mathbf{E}$, Eq. 4.15 becomes $\omega = \frac{kc}{\sqrt{\epsilon(\omega)}}$ which, in turn, can be satisfied by two different sets of $\omega - k$ values showed in Fig 4.2-B. The lower branch exhibits an electromagnetic character when k is small and turns into the optical transverse phonon dispersion curve for large values of the wave vector. On the contrary, the upper branch behaves like an LO phonon around $k = 0$ and tends asymptotically to the light line with propagation velocity $\frac{c}{\sqrt{\epsilon(\infty)}}$.

It is evident from Fig. 4.2-B that there is no solution to Eq. 4.15 between ω_{TO} and ω_{LO}: no electromagnetic waves can propagate inside the medium at frequencies $\omega_{TO} \leq \omega \leq \omega_{LO}$. This range of frequencies is known as the *Reststrählen* band and is responsible for the close to 100% plateau observable in reflectance curves.

4.1.2 Phonon strength function

Since, as just discussed, a polariton has a dual nature, it is convenient to define a function that "weights" the wave and the phonon contribution. The natural starting point to accomplish this goal is to work out the energy density (kinetic and potential) associated to the phonon field in the hypothesis that it is oscillating at frequency ω:

$$U_L = \frac{1}{2}\dot{W}^2 + \frac{1}{2}\omega_{TO}^2 W^2 = \frac{1}{2}(\omega^2 + \omega_{TO}^2)W^2 \tag{4.16}$$

The energy density can be analogously written for the electric field as:

$$U_E = \frac{\epsilon_\infty}{8\pi}E^2 + \frac{1}{8\pi}H^2 = \frac{1}{8\pi}(\epsilon_\infty + \epsilon)E^2 \tag{4.17}$$

Finally, the total energy can be determined adding up Eq. 4.16 and Eq. 4.17:

$$U_T = \frac{1}{2}(\omega^2 + \omega_{TO}^2)W^2 + \frac{1}{8\pi}(\epsilon_\infty + \epsilon)E^2 \tag{4.18}$$

Furthermore, recalling Eq. 4.6, U_T can be recast in this form:

$$U_T = W^2(\epsilon + \frac{\omega}{2}\frac{\partial\epsilon}{\partial\omega})\frac{(\omega_{TO}^2 - \omega^2)^2}{\omega_p^2} \tag{4.19}$$

where ϵ is defined in Eq. 4.10. Eq. 4.19 was obtained through a purely classical mechanics approach but can be generalized to the quantum mechanics case provided W is replaced by $< W >$: the expectation value of the generalized displacement. The simple harmonic oscillator model can now be invoked to express the energy density as:

$$U_T = \frac{\hbar\omega}{V}(N + \frac{1}{2}) \tag{4.20}$$

where N represents the number of phonons. $< W^2 >$ can be found by equating Eq. 4.19 to Eq. 4.20:

$$< W^2 >= \frac{\hbar\omega}{2V}\frac{\omega_p^2}{(\omega_{TO}^2 - \omega^2)^2}\frac{1 + 2N}{\epsilon + \frac{1}{2}\omega(\frac{\partial\epsilon}{\partial\omega})} \tag{4.21}$$

This apparently intimidating expression turns into a more familiar form in the limit $\omega \mapsto \omega_{TO}$:

$$< W^2 >_0= \frac{\hbar}{2V\omega_{TO}}(1 + 2N) \tag{4.22}$$

In a harmonic oscillator, this is the expectation value of W^2 at the presence of N quanta. Eq. 4.21 and Eq. 4.22 are the last piece required to define the *Phonon Weight Function*, L_P:

$$L_P(\omega) = \frac{< W^2 >}{< W^2 >_0} = \frac{\omega\,\omega_p^2\,\omega_{TO}}{(\omega_{TO}^2 - \omega^2)^2}\frac{1}{\epsilon_\infty + \omega_p^2\,\omega_{TO}^2(\omega_{TO}^2 - \omega^2)^{-2}} \tag{4.23}$$

L_P is graphed in Fig 4.3-A in the case $\frac{\omega_{LO}}{\omega_{TO}} = 2$. As expected, when the polariton exhibits an electromagnetic nature ($\omega \mapsto \infty$), the function is zero. On the other hand, $L_P(\omega)$ becomes unitary at $\omega = \omega_{TO}$ when the polariton behaves like a phonon. L_P is not defined in the *Reststrählen* band where polaritons do not exist.

Analogously, recalling that $U_T = \epsilon_\infty < E^2 >_0 /4\pi$, the *Electric Field Strength Function* [62], $L_E(\omega)$, can be found:

$$L_E(\omega) = \frac{< E^2 >}{< E^2 >_0} = \epsilon_\infty \Big(\epsilon_\infty + \frac{\omega_p^2 \omega_{TO}^2}{(\omega_{TO}^2 - \omega^2)^2}\Big)^{-1} \tag{4.24}$$

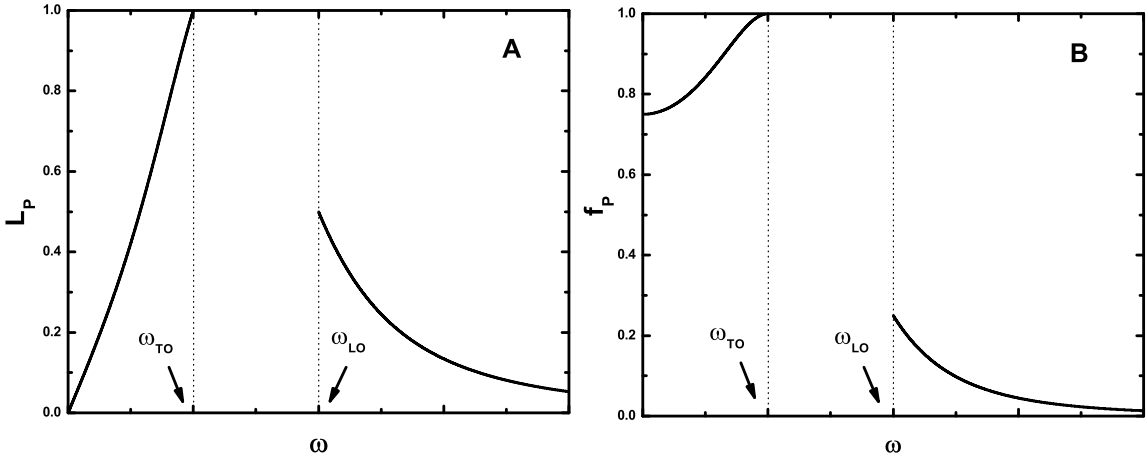

Figure 4.3: (A): *Phonon Strength Function* L_P (B): Fraction of the energy of the electromagnetic wave stored in the lattice motion.

The physical significance of L_P and L_E can be better appreciated after considering the following sum rule:

$$\omega L_E + \omega_{TO} L_P = \omega \tag{4.25}$$

Multiplication of both sides of Eq. 4.25 by $\hbar$ leads to an energy balance: the total energy of the incident photon ($\hbar\omega$) is stored into an electromagnetic field and a phonon field. Thus, the percentage fraction of the total energy transferred to the phonon mode can be defined as:

$$f_P = \frac{\omega_{TO}}{\omega} L_P \tag{4.26}$$

f_P is plotted in Fig. 4.3-B and resembles in great part F_P with only one exception: the region close to $\omega = 0$. Although $L_P = 0$ at $\omega = 0$, the phonon field still carries some energy

whose value depends exclusively on the material parameters (ω_{TO}, ω_{LO} and ϵ_∞).

4.2 Plasmon phonon coupled modes

In this section the effect of free carriers will be included in the treatment developed so far. Rather than again going over the lengthy procedure outlined in the previous section, the well known Drude model [63] will be invoked. According to Drude's theory, in the absence of losses the dielectric constant of a material with a carrier density n can be written as:

$$\epsilon(\omega) = 1 - \frac{\omega_p^2}{\omega^2} \tag{4.27}$$

Here $\omega_p^2 = 4\pi e^2 n/m_R$ (m_R is the carriers' effective mass) and it is the carriers' plasma frequency analogous to the one which was introduced in Eq. 4.11 for phonons. Assuming that the carriers do not interact with the lattice ions, the lattice Hamiltonian has to be modified by including an additional term: $H = H_{PHONON} + H_{CARRIER}$, with H_{PHONON} given by Eq. 4.4. Without retracing all the steps previously followed, it is possible to predict, within the rotating phase approximation [64], that the electrical susceptibility will be $\chi = \chi_{PHONON} + \chi_{CARRIER}$. Since $\epsilon = 1 + 4\pi\chi$, the dielectric constant becomes $\epsilon = \epsilon_{PHONON} + \epsilon_{CARRIER} - 1$, i.e.:

$$\epsilon = \epsilon_\infty \frac{\omega^2 - \omega_{LO}^2}{\omega^2 - \omega_{TO}^2} - \frac{\omega_p^2}{\omega^2} \tag{4.28}$$

In Fig. 4.4-A $\epsilon(\omega)$ is plotted as a function of frequency. Eq. 4.15 can now be solved with the new expression for the dielectric constant. Once again there will be two branches for the transverse mode ($\mathbf{k} \perp \mathbf{E}$) and, as opposed to the case of a simple polariton, two branches for the longitudinal mode ($\mathbf{k} \| \mathbf{E}$) as well. This is due to the fact that the equation $\epsilon(\omega) = 0$ has two different solutions. Even though the frequency of the LO phonon remains independent of the wave vector k, it is strongly related to the plasma frequency ($\omega_p \propto \sqrt{n}$). Fig. 4.4-B depicts the effect of an increase in carrier concentration: the higher branch frequency keeps raising while the lower branch bends down until it reaches asymptotically the TO mode frequency. This is the ultimate manifestation of the free carrier mediated coupling between the electromagnetic field and the LO phonon mode: the Coulomb field of the electrons

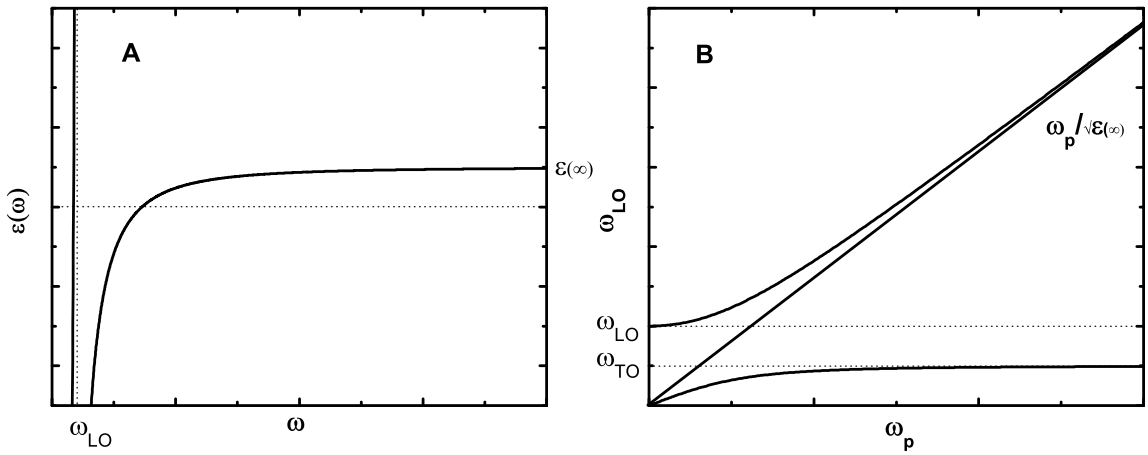

Figure 4.4: (A): Dielectric constant calculated according to Eq. 4.28 (B): LO phonon dependence on the plasma frequency ω_p.

interacting with light can drive the longitudinal mode and deeply affect its frequency.

4.3 Surface polariton

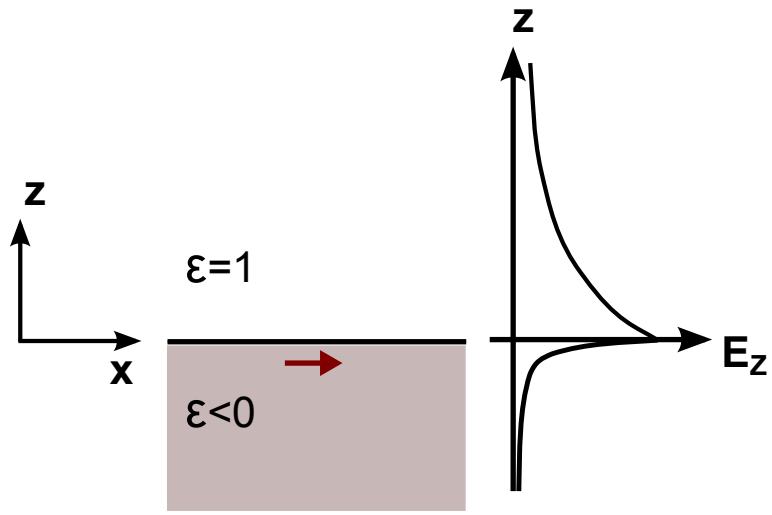

Figure 4.5: Surface plasmon propagating at the interface between AIR and a dielectric with $\epsilon < 0$

Looking both at Fig. 4.2 and Fig. 4.4, it is evident that there is a range of frequencies in which the dielectric constant is negative. This aspect becomes particularly significant when considering the propagation of an electromagnetic wave at the interface between two media with different dielectric constants (see Fig. 4.5). Normally this "boundary" problem is treated within the classical reflection-transmission framework. When a wave traveling

in air encounters the interface with a dielectric medium, part of it is reflected away from it, part of it is transmitted inside the medium where it propagates over a length scale defined by the material penetration depth. In the case of p-polarized electric field though, Maxwell's equations admit another solution [65] which is commonly referred to as *Surface Plasmon Polariton* (SPP) and whose signature is an electric field decaying on both sides of the interface, see Fig. 4.5. Surface plasmon modes are easily identified in the simplest possible geometry: the interface between a metal (dielectric constant given by Eq. 4.27) and air. Adopting the reference frame indicated in Fig. 4.5, the electric and magnetic field are written as:

$$\mathbf{E} = [E_x, 0, E_z] \qquad \mathbf{H} = [0, H_y, 0] \tag{4.29}$$

Maxwell's equations without sources read:

$$\begin{cases} \nabla \times \mathbf{E} = -\frac{1}{c}\frac{\partial \mathbf{B}}{\partial t} \\ \nabla \times \mathbf{H} = \frac{1}{c}\frac{\partial \mathbf{D}}{\partial t} \end{cases} \tag{4.30}$$

Postulating a solution of the type $e^{i(kx-\omega t)}$, the system in Eq. 4.30 can be reduced to:

$$\begin{cases} \frac{\epsilon\omega^2}{c^2}E_x + \frac{\partial^2 E_x}{\partial z^2} = ik\frac{\partial E_z}{\partial z} \\ E_z = \frac{ik}{\epsilon\omega^2/c^2 - k^2}\frac{\partial E_x}{\partial z} \end{cases} \tag{4.31}$$

The solution is different in air ($z > 0$) and in the dielectric medium ($z < 0$):

$$\begin{cases} E_x = E^+ e^{-\alpha z}, & \text{if } z > 0 \\ E_x = E^+ e^{\beta z}, & \text{if } z < 0 \end{cases} \tag{4.32}$$

$\alpha^2 = k^2 - \omega^2/c^2$ and $\beta^2 = k^2 - \epsilon\omega^2/c^2$; the air dielectric constant has been assumed unitary. Eq. 4.32 is physically meaningful only is α and β are positive. If this were not the case, the wave would be carrying an exponentially growing power. Imposing the appropriate

boundary conditions at $x = 0$ on E_x and E_z leads us to:

$$\frac{\beta}{\alpha} = -\epsilon \tag{4.33}$$

Since both $\alpha > 0$ and $\beta > 0$, the only way to satisfy Eq. 4.33 is to have $\epsilon < 0$. This justifies our initial interest in materials with a negative dielectric constant. Eq. 4.33 can be rewritten in a more explicit form:

$$k^2 = \frac{\mid \epsilon \mid}{\mid \epsilon \mid -1} \frac{\omega^2}{c^2} \tag{4.34}$$

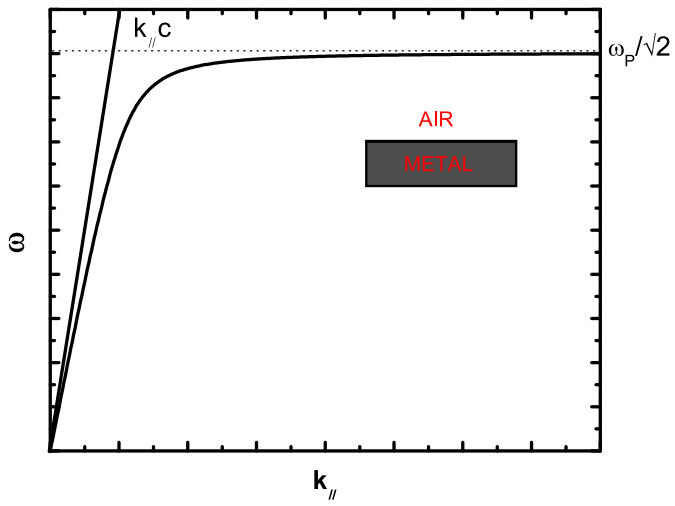

Figure 4.6: Dispersion relation of a surface plasmon propagating at the interface metal-air.

In the case of a metal, ϵ is given by Eq. 4.27 and the dispersion relation is shown in Fig. 4.6. A few observations can now be made. First, the plasmon mode exists only in the region $\omega < \omega_p$ where the dielectric constant is negative. Further, when $k \simeq 0$ the dispersion curve is well approximated by the light line ($\omega = kc$). Finally, when $k >> k_p = \omega_p/c$, $\omega \mapsto \omega_p/\sqrt{2}$. It is also worth noticing that $\epsilon(\omega_p/\sqrt{2}) = -1$. As a result, in the short wavelength range, the plasmon tends to the frequency at which the dielectric constant is -1. From now on this frequency will be called ω_D.

One last piece can be added to the general picture by discussing the case of surface plasmons excited in a dielectric material with an infrared active mode (dielectric constant given by Eq. 4.10). In this case the plasmon frequency has to be confined in the $\omega_{TO} - \omega_{LO}$ range where $\epsilon < 0$ (see Fig. 4.2-A) and the asymptotic value ω_D is now $\sqrt{\frac{\epsilon_\infty \omega_{LO}^2 - \omega_{TO}^2}{1+\epsilon_\infty}}$ as visible in the plot of the dispersion relation (Fig. 4.7-A). The situation does not vary much when dealing with a stack of thickness a of the same dielectric medium surrounded by air (see inset of Fig 4.7-B). The presence of two interfaces gives rise to two distinct plasmon polariton branches (the red and black curves in Fig. 4.7-B). The two curves converge to the same ω_D of Fig. 4.7-A in the limit $k_\parallel a \mapsto \infty$. This is because when $\lambda \mapsto 0$ or $a \mapsto \infty$ the two interfaces are completely decoupled and there is no longer any difference between the two geometries in Fig. 4.7-A and Fig. 4.7-B.

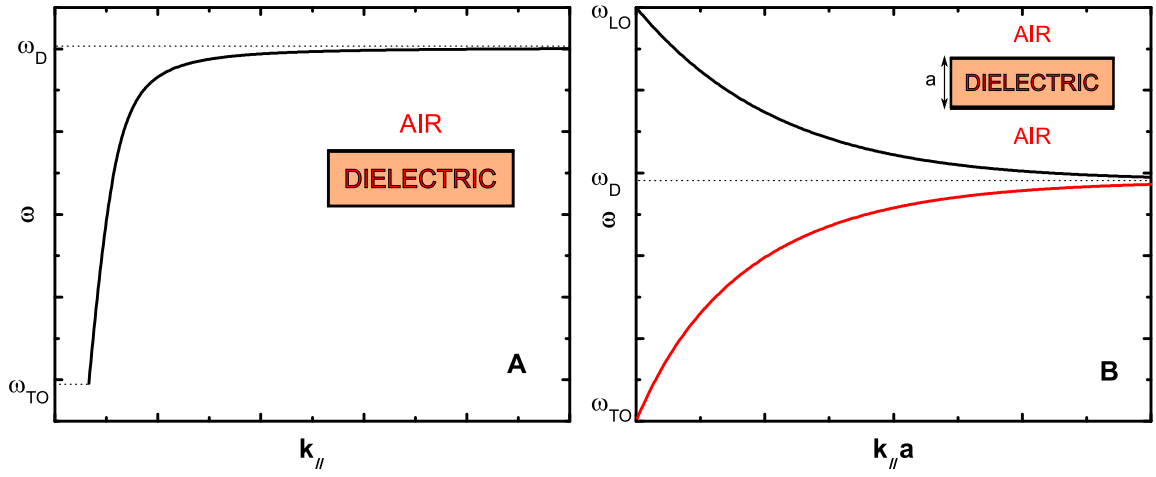

Figure 4.7: (A): dispersion relation for a surface plasmon propagating at the interface dielectric-air (B): surface plasmon mode for a air-dielectric-air stack.

4.4 Raman Scattering by polaritons

All the different polariton modes introduced so far can be measured experimentally through Raman spectroscopy. An overview of the milestones in the field of Raman scattering by polariton is thus necessary, especially to discuss how it is actually possible to probe the polariton dispersion curve by a proper choice of the scattering geometry. As seen in Chap. II, Raman scattering always requires the conservation of energy and momentum. If $(\mathbf{k}_I, \omega_I)$, $(\mathbf{k}_S, \omega_S)$ and $(\mathbf{q}, \omega)$ are the wave vectors and frequencies of the incident, scattered and

polariton field, it is always possible to write:

$$\begin{aligned} k_I c &= n_I \omega_I \\ k_S c &= n_S \omega_S \end{aligned} \tag{4.35}$$

where c is the speed of light, while n_I and n_S are the refractive of the scattering medium at ω_I and ω_S respectively.

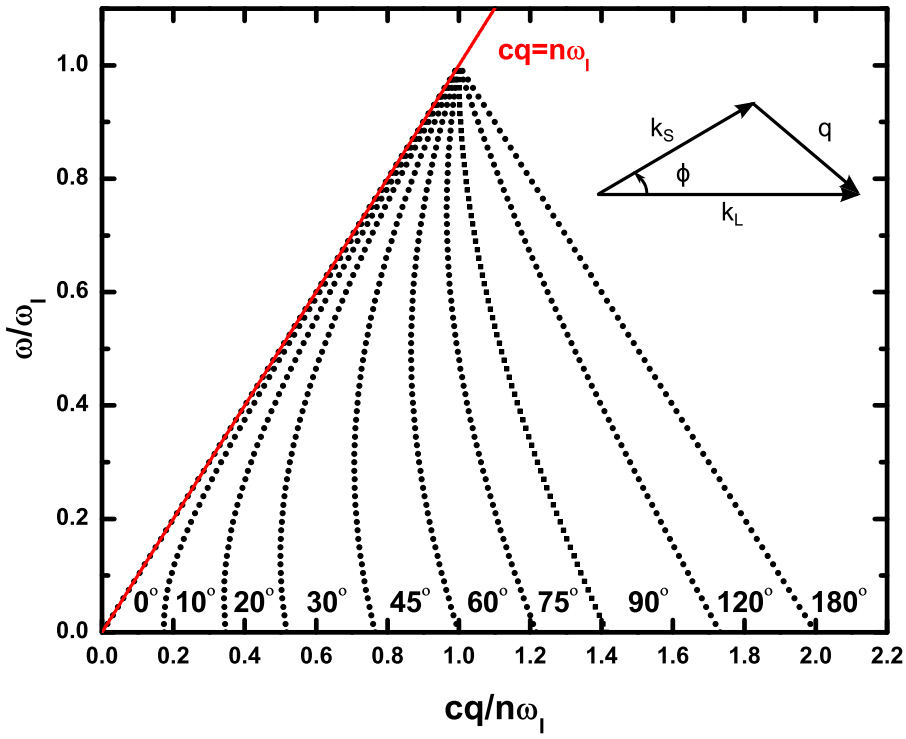

Figure 4.8: Accessible region in the $q - \omega$ plane for Stokes scattering of incident light at frequency ω_L in a medium with refractive index n. The light line is in red.

Following [20], conservation of momentum and energy can then be rewritten as:

$$\begin{aligned} q^2 &= k_I^2 + k_S^2 - 2\, k_I\, k_S \cos(\phi) \\ \omega &= \omega_I - \omega_S \end{aligned} \tag{4.36}$$

Fig. 4.8 inset helps to visualize the wave vector arrangement predicted by Eq. 4.36. Using

Eq. 4.35, Eq. 4.36 can be condensed into a compact expression:

$$c^2q^2 = n_I^2\omega_I^2 + n_S^2(\omega_I - \omega)^2 - 2n_I n_S \omega_I(\omega_I - \omega)\cos(\phi) \tag{4.37}$$

where the only variables are the wave vector (q) and the frequency (ω) of the polariton. Eq. 4.37, graphed in Fig. 4.8 together with the light line, defines a line in the $q-\omega$ plane, so that, by varying the value of ϕ from 0° (forward scattering) to 180° (backward scattering), it is possible to identify the region accessible through Raman spectroscopy. The excited polariton branch and frequencies are thus found simply intersecting the previously discussed dispersion relations with the curve in Fig. 4.37 corresponding to the collection angle ϕ. A pioneering work in the field of Raman scattering by polaritons is the paper by Henry and Hopfield [66], who were able to reproduce experimentally the dispersion relation shown in Fig. 4.2-B for GaP. Following a similar approach, Davydov et al. [67] recovered the graphs in Fig. 4.7 by measuring the surface plasmon dispersion in the case of a thick and thin dielectric layer of GaN.

4.5 GaAs

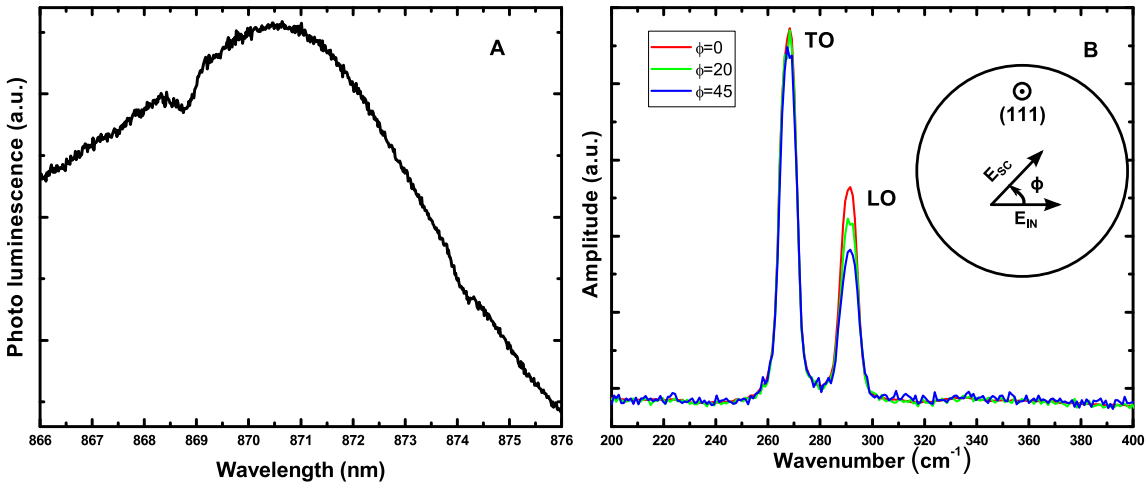

Figure 4.9: (A): GaAs band gap (the two dips at 869nm and 874 are due to condensation onto the Si photo detector) (B): (111) GaAs phonon peaks, $\lambda_L = 488nm$.

GaAs was the first material that was measured in order to verify experimentally some of the theoretical conclusions drawn in the previous section. GaAs is a III-V direct band

gap semiconductor which crystallizes in the zinc blend structure, space group T_d. At room temperature the gap is located at $\simeq 871$nm (see Fig 4.9-A) and, as it is usually the case with the majority of semiconductors, gets wider when the temperature is lowered. The particular sample used in our measurements was a semi-insulating, undoped crystal oriented along the (111) direction. The GaAs crystal structure allows for a triply degenerate optical phonon mode, belonging to the T_2 (or Γ_5) representation, which is both Raman and infrared active [68]. The three Raman tensors relative to the coordinate system $(X, Y, Z) = ([110], [11\bar{2}], [111])$ are [18, 69]:

$$R(X) = \frac{d}{\sqrt{3}} \begin{bmatrix} 0 & \sqrt{2} & -1 \\ \sqrt{2} & 0 & 0 \\ -1 & 0 & 0 \end{bmatrix} R(Y) = \frac{d}{\sqrt{3}} \begin{bmatrix} \sqrt{2} & 0 & 0 \\ 0 & -\sqrt{2} & -1 \\ 0 & -1 & 0 \end{bmatrix} R(Z) = \frac{d}{\sqrt{3}} \begin{bmatrix} -1 & 0 & 0 \\ 0 & -1 & 0 \\ 0 & 0 & 2 \end{bmatrix} \tag{4.38}$$

When light is incident along the (111) direction, both the TO and LO mode can be observed through Raman spectroscopy, as opposed to the (100) case where only the LO mode can be excited. The Raman tensors that were just introduced can be employed to determine the selection rules relative to the $z(xy)\bar{z}$ geometry (shown in the inset of Fig 4.9-B):

$$\begin{aligned} \sigma(TO) &\propto \tfrac{2}{3}d^2 \\ \sigma(LO) &\propto \tfrac{d^2}{3}cos^2(\phi) \end{aligned} \tag{4.39}$$

where σ is the scattering cross section for the two different modes.

The Raman spectra collected at room temperature with excitation wavelength $\lambda_{\mathrm{L}} = 488$nm are shown in Fig 4.9-B. The LO and TO mode are clearly visible at $\simeq 268.2\mathrm{cm}^{-1}$ (8THz) and at $\simeq 291.5\mathrm{cm}^{-1}$ (8.74THz). The dependence on the angle between the incident and scattered electric field is verified for three different values of ϕ.

ISRS measurements at 800nm were carried out on the same sample. Since this wavelength is above the gap, coherent phonons were detected by measuring the differential change in the probe beam reflected by the sample (see Fig. 3.10). The pulse width was always below $\simeq 80$fs, while the pump and probe beam power was 100mW and 30mW respectively. In order to minimize the background arising from pump leakage, the pump and probe polarizations were set perpendicular to each other and inserted a polarizer with

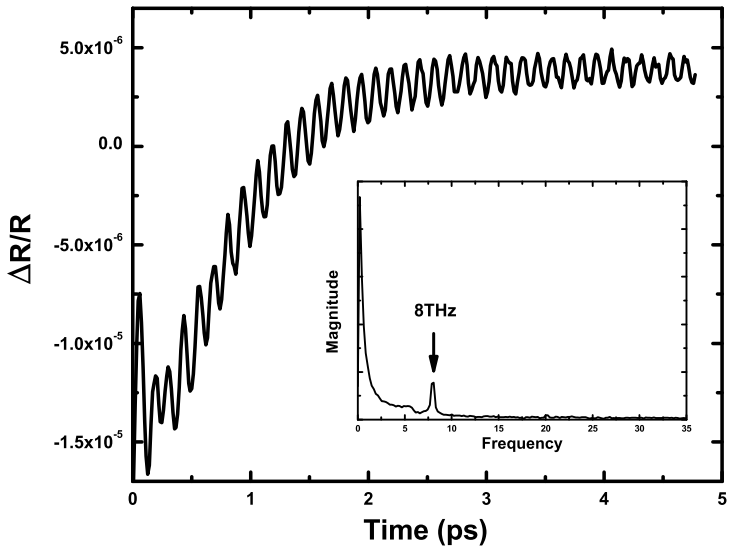

Figure 4.10: GaAs differential reflection ISRS signal at $100K$ and relative Fourier Tranform.

the axis parallel to the probe polarization in front of the detector. Employing the Raman tensors (Eq. 4.38), it is possible to calculate the selection rules pertaining to the impulsive stimulated case. The LO mode can alway be excited regardless of the detection geometry, while the TO mode amplitude has an intensity $\propto \cos(2\phi)$, where ϕ is now the angle between the pump and probe field. The differential reflection signal measured at 100K is shown as a function of the pump-probe time delay together with its Fourier Transform in Fig. 4.10. It is evident that only one mode at the TO frequency (8THz) is observable. The oscillations do not disappear when ϕ is varied, so that the signal observed, even though at the TO mode frequency, seems to obey the LO mode selection rules. This apparent anomaly has been consistently verified at other temperatures. In Fig. 4.11-A the signal at 10K, 50K and 300K is reported and in Fig. 4.11-B the oscillation frequency, extracted through linear prediction [70], is plotted as a function of temperature. The absence of the LO mode from our data can be explained in the context of the plasmon polariton theory, introduced in Sec. 4.2. Since the excitation energy is above the semiconductor band gap, whenever a laser pulse hits the sample new carriers are photo excited. Thus, the originally intrinsic semiconductor experiences a sudden increase in the concentration of free carriers, which ultimately reflects in an augmented value of the plasma frequency (Eq. 4.27). The LO mode, which is now

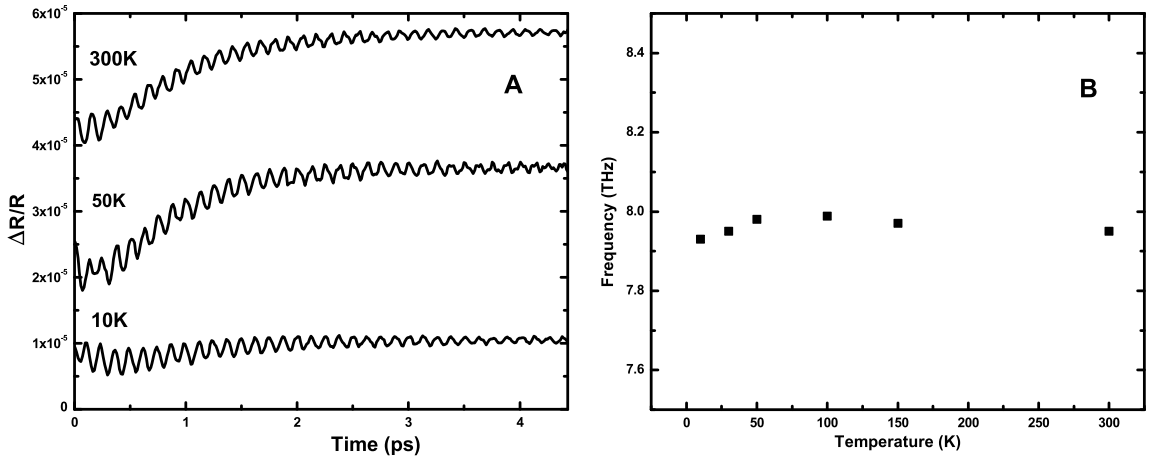

Figure 4.11: (A): Reflection pump probe data on (111) GaAs at different temperatures, $\lambda_L = 800nm$ (B): Frequency of the measures signal as a function of temperature.

split into two separate branches (Fig. 4.4-B), undergoes a frequency shift induced by the variations in the carrier density. When ω_p becomes sufficiently large, the lower branch approaches asymptotically the TO mode frequency, while the higher branch keeps increasing in frequency as visible in Fig. 4.4-B. Given the large power used in our experiments and the considerable fluence of the laser pulses, it can be inferred that the observed frequency is precisely the LO mode oscillating at the TO frequency due to the presence of carriers. In principle, the upper branch frequency should be detected as well, but the pulse width of the laser source (80fs) is not short enough to excite such a rapidly oscillating signal ($f > 8.7$THz).

4.5.1 Literature discussion

The experimental results presented so far seem to be in contradiction with some work from the literature. Cho et al. [43], among others, were able to measure the LO phonon by ISRS in a bulk GaAs sample. To understand why this was not possible in our case, it is necessary to first identify the different physical mechanisms [42, 71, 72, 73, 74] through which an LO mode can be excited in GaAs and then establish whether or not each one of them is active in a specific experimental condition.

Pfeifer et al. [74] correctly pointed out that the force driving a longitudinal phonon

mode includes, in addition to the Raman tensor, a non linear polarization term, P^{NL}:

$$F_j = R_{kl}^{(i)} E_k E_l - \frac{4\pi z e^*}{\epsilon_\infty} P_j^{NL} \tag{4.40}$$

where E_k and E_l are the incident and scattered field. P^{NL} contains three main contributions:

$$\mathbf{P}_j^{NL} = \chi_{jkl}^{(2)} E_k E_l + \chi_{jklm}^{(3)} E_k E_l E_m + \int_{-\infty}^{t} J_j(t')\,\mathrm{d}t' \tag{4.41}$$

where $\chi_{jkl}^{(2)}$ and $\chi_{jklm}^{(3)}$ are the second and third-order nonlinear susceptibilities and $J_j(t)$ is a current associated with the drift of photoexcited carries in surface-space-charge fields. The last term is responsible for longitudinal phonon excitation in GaAs and other III-V semiconductors.

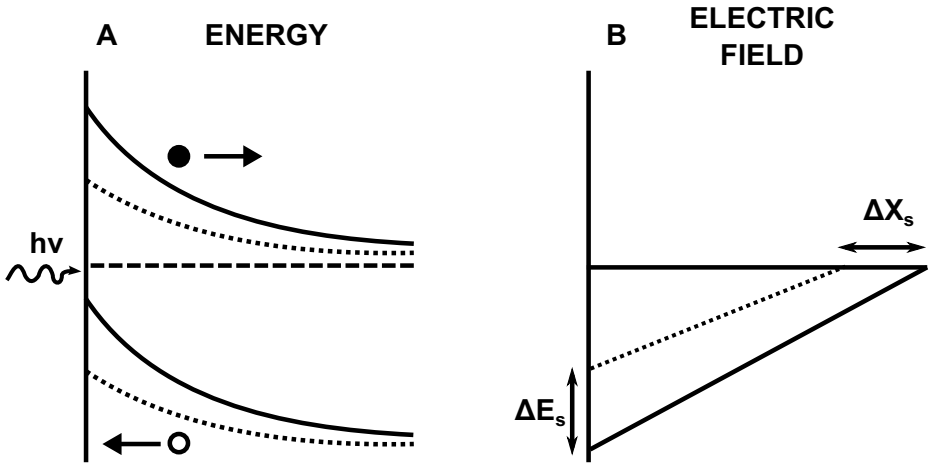

Figure 4.12: Energy band diagram (A) and electric field (B) within the space charge layer of an n-doped semiconductor before (continuous line) and after (dashed line) the arrival of the optical pulse of energy $h\nu > E_{GAP}$.

By solving Eq. 4.6 in the static case, it is possible to see that a static electric field (E) induces an atomic displacement given by:

$$W = \frac{z * e}{\sqrt{M_R V_C}\omega_{\mathrm{TO}}^2} E \tag{4.42}$$

Hence, the depolarization of the static field, caused by ultrafast photocurrents $J(t)$, perturbs the lattice arrangement and acts as an impulsive driving force in the equation of motion of the phonon amplitude, $q(t)$, see Eq. 2.31. This is precisely what happens when the

surface space-charge electric field gets screened by photo excited carriers. Fig. 4.12 shows how the absorption of photons with energy $h\nu$ leads to a change in the energy band profile (Fig. 4.12-A) and, consequently, in the electric field (Fig. 4.12-B). Given the pivotal role played by the static electric surface field (E_S), its expression will be reported [75]:

$$E_S = \sqrt{\frac{2eN_D}{\epsilon(0)}(V_{bi} - U - \frac{k_B T}{e})} \tag{4.43}$$

where e is the electron charge, $\epsilon(0)$ the static dielectric constant, V_{bi} the junction built-in voltage, N_D the doping level and U the externally applied bias voltage. Several experiments performed on (100) GaAs provide strong evidence to confirm this theory.

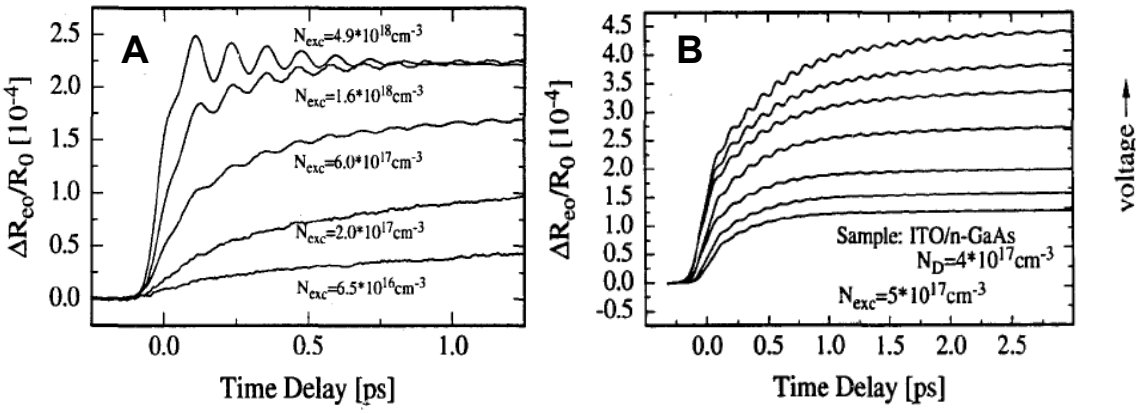

Figure 4.13: (A): Time domain signal of a p-doped (100) GaAs sample ($N_A = 10^{18} cm^{-3}$) as a function of the photo excited carrier density, from [74] (B): Time domain signal for a n-doped (100) GaAs sample as a function of the static surface field, from [74].

In Fig 4.13-A phonon oscillations are plotted as a function of the photo excited carrier density, which is controlled by changing the intensity of the incident laser beam (λ_L = 620nm). In contrast, Fig 4.13-B shows the LO oscillatory signal as a function of the surface static electric field. In the latter case, the GaAs sample was grown on a transparent Indium Tin Oxide (ITO) Schottky contact so that an external bias voltage (U) could be applied to control the electric field in the depleted region.

The scenario is substantially different when the excitation wavelength is increased. Cho et al. [73] performed ISRS on GaAs at $\lambda_L = 844$nm (very close to the wavelength used in our experiments, 800nm) with a significantly different outcome (see Fig. 4.14). In this case, the incident photon energy is so low that the penetration depth ($\simeq 1\mu$m) exceeds by far the

surface depletion layer (< 100nm). The photons are consequently absorbed mainly in the neutral bulk region of the semiconductor where the electron-hole pairs, created through the doping process and the photon absorption, do not affect the charge-depleted-layer electric field. The interaction between the free carriers and the LO phonon gives rise to a plasmon mode which is now driven exclusively by the Raman-like force in Eq. 4.40. As discussed in Sec.4.2, the LO frequency depends strongly on the carrier density (n). In Fig. 4.14-B it is indeed shown that the frequency of the measured phonon oscillations is a function of the total carrier concentration (photo excited and majority carriers). In particular, it can be observed that, in accordance with our experiments, for high enough values of n the plasmon lower branch approaches 8THz, the transverse mode frequency.

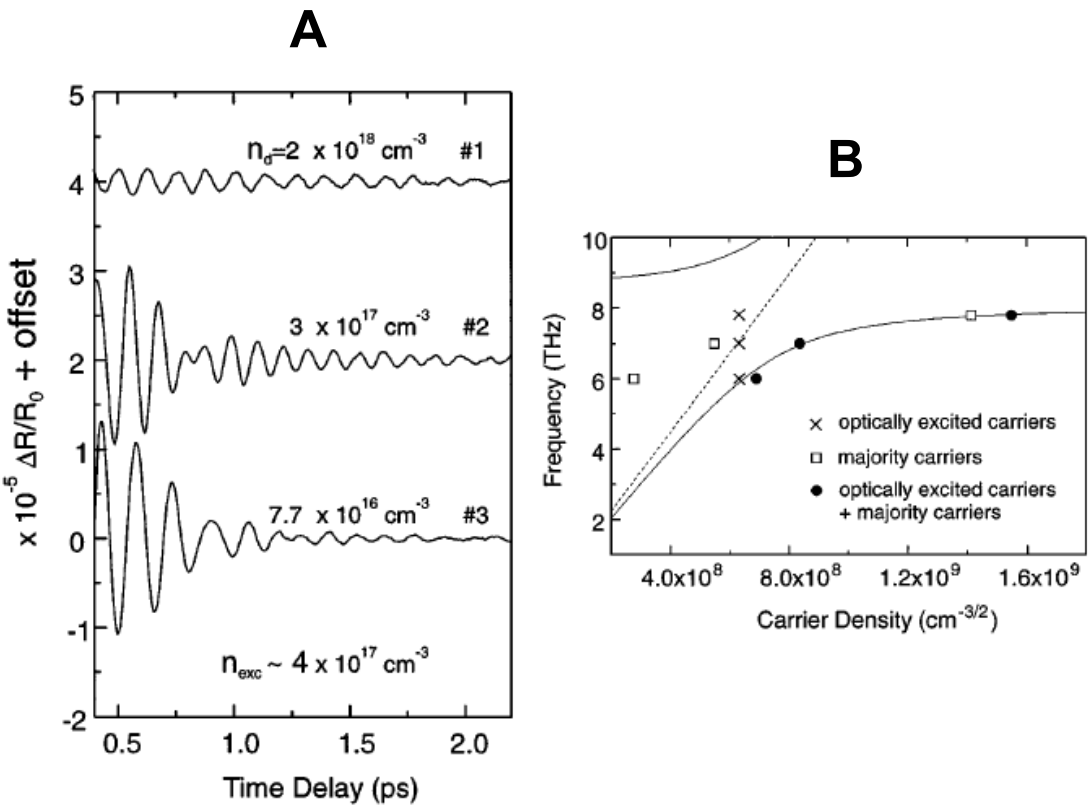

Figure 4.14: (A) Oscillatory part of the reflectivity change in differently doped n-GaAs at a constant excitation density $\simeq 4 \times 10^{17}\text{cm}^{-3}$, from [73] (B) Plasmon-phonon dispersion curve as a function of the optically excited density (crosses), the doped density (squares) and the sum of both (circles); the solid line is the theoretical prediction, from [73].

4.6 GaSe

The second material that was considered is another very popular semiconductor: GaSe. This material was originally chosen to verify the theoretical prediction about the Raman Tensor expression in the case of spontaneous and stimulated Raman spectroscopy [2] discussed in Chap. II. However, after a first round of experiments, it became obvious that, in order to make sense of the measurements' outcome, it was necessary to develop a broader and more exhaustive model than simple Raman scattering by phonons. Once again, the correct interpretation of the experimental data seems to be closely connected to the phonon polariton theory discussed in Sec. 4.1.

4.6.1 Material properties

GaSe is a III-VI indirect gap layered semiconductor. The different layers, visible in Fig. 4.15, interact through the weak van der Waals force, while the atoms belonging to the same layer are tied together through the much stronger covalent bonds. This fundamental spatial anisotropy is responsible for, among other phenomena, the material birefringence.

The fundamental gap of this semiconductor is centered around 600nm and changes as a function of temperature, ranging between $\simeq$ 590nm at 10K and $\simeq$ 620nm at 300K [76].

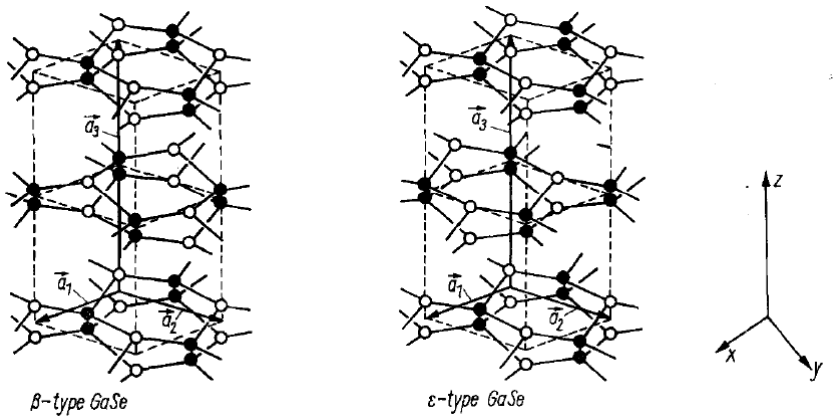

Figure 4.15: Ga (full circles) and Se (empty circle) coordination in the hexagonal GaSe, from [77]

Hence, GaSe turns out to be particularly attractive given the ability to probe it at wavelengths above (Argon laser and optical OPA) and below (Ti:Sapphire and RegA) the gap.

GaSe crystallizes in three different polytypes: ϵ and β (hexagonal structure) and γ

(rhomboedral structure). The β and ϵ types, shown in Fig. 4.15, have the same crystal structure in the layers' plane but are characterized by a different stacking sequence. While the β polytype has an inversion center located in the mid plane between layers, such a symmetry is not present in the ϵ polytype. Thus, the Raman modes are not infrared active in the β structure [78].

4.6.2 Sample preparation

All the GaSe samples used in this dissertation were prepared starting from a bulk 1cm $\times$ 1cm $\times$ 0.5cm crystal oriented along the c-axis. The weak attraction between layers makes it extremely easy to peel thin sheets off the main surface using scotch tape. These films were then glued to a copper substrate using a low temperature conductive varnish and peeled again until the desired thickness was obtained. When aiming for a thicker ($\simeq 100\mu$m) sample, a piece was cleaved from the bulk sample with a razor blade, glued on the substrate and finally peeled with scotch tape to remove any roughness.

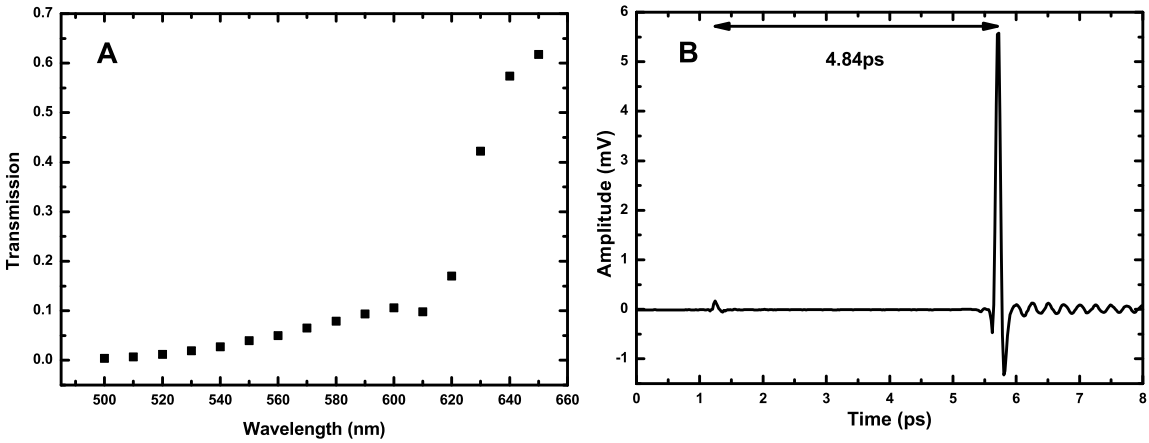

Figure 4.16: (A): Transmission curve through a $\simeq 50\mu$m thick GaSe sample (B): Differential transmission as a function of time for a $\simeq 240\mu$m GaSe sample, $\lambda_{\mathrm{L}} = 800$nm.

The ISRS measurements were all performed in the transmission geometry shown in Fig. 3.11. As a result, it was critical, especially when the laser was above the gap, to choose the sample thickness in such a way that the transmitted beam could be measured by our photo detectors (P $\geq 10\mu$W). In Fig. 4.16-A the transmission curve is plotted as a function of the laser wavelength at $300K$. The sample under examination was kept under vacuum inside a cryostat and the relative transmission was obtained by normalizing each data point by

the power transmitted through the empty cryostat to remove the influence of the CaF_2 windows. The data was fit using the Fresnel equations for normal incidence [26]. The absence of Fabry-Perot interference fringes, the inaccuracy of the GaSe optical constants and the coarse distribution of points made it challenging to get a good fit. Nevertheless, the thickness of the sample was estimated to be
$\simeq 50\mu\text{m} \pm 5\mu\text{m}$. This thickness guaranteed adequate transmission at the visible wavelengths of interest and was thus used in all the above the gap experiments.

A different issue arises when the sample is tested below the gap. The differential transmission through the sample as a function of the pump-probe time delay is shown in Fig. 4.16-B. Here an extra coherent artifact, displaced by about 5ps from the main one, can be seen. The presence of this and other additional peaks located before and after time zero has already been observed and explained [19] by the interaction between the incident laser beam and its reflections at the back and front surface of the sample. The reflection coefficient at the interface GaSe-air is $\simeq 0.23$ due to the high refractive index of the material ($n \simeq 2.84$); consequently, the extra peaks are relatively strong and can interfere with the coherent phonon signal. To prevent these spikes from distorting the phonon-induced signal, a much thicker sample was prepared using the razor blade cleaving technique. This time it was possible to more accurately calculate the exact thickness of the sample knowing that the spacing between two consecutive peaks is given by $\frac{2nL}{c}$, with c being the speed of light, n the refractive index and L the sample thickness. After a few trials, a $\simeq 240\mu$m thick sample, granting a 4ps spacing between successive coherent artifacts, was obtained.

4.6.3 Phonon dynamics

The GaSe unit cell contains 4 molecules and thus there are 24 normal vibrations in total. Since our sample is a ϵ-polytype, the phonon modes (at Γ) can be decomposed into the following irreducible representations of the D_{3h} point group [81]:

$$\Gamma \equiv 4A_1^{'} + 4A_2^{'} + 4E^{'} + 4E^{''} \tag{4.44}$$

A unit cell is made up of two layers; however, it is easier to get an intuitive picture of what the different phonon modes look like by considering first only a single layer (2 molecules) as

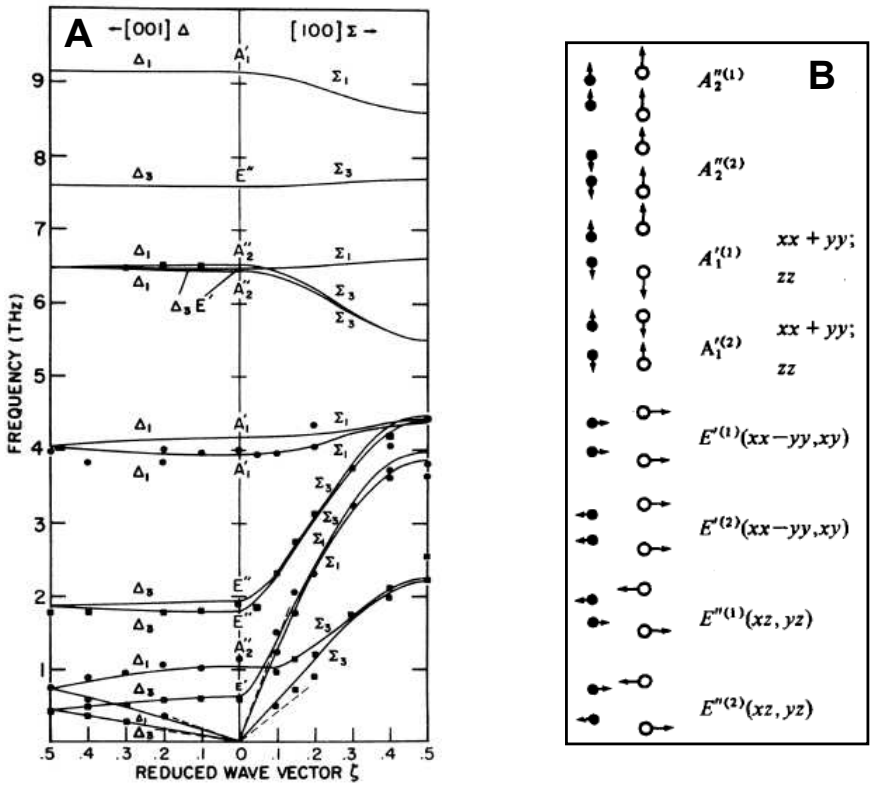

Figure 4.17: (A): Dispersion curves, experimental (symbols) and fitted (solid lines), for the Δ and Σ directions in ϵ-GaSe, from [79] (B): Schematic displacement of the cations ($\bullet$) and anions ($\circ$) in one layer of GaSe, from [80].

shown in Fig 4.17-B. The vibrations in the neglected layer are either the same or out of phase [80]. Looking at the quadratic functions by which each vibration transforms (Fig 4.17-B), it is possible to identify the Raman active modes, namely $A_1^{'}$, $E^{'}$ and $E^{''}$. The fact that $E^{'}$ is also infrared active, since it transforms like (x, y) [77], confirms the lack of inversion symmetry of the ϵ polytype. The phonon frequencies and their dispersion relations relative to the [011] and [100] directions are shown in Fig 4.17-A.

4.6.4 Spontaneous Raman scattering

Before discussing the experimental results, the Raman tensors associated to the phonon modes introduced in the previous section will be quickly described. The strongest mode

detected is the $A_1^{'}$ mode:

$$R^{A_1'} = \begin{bmatrix} a & 0 & 0 \\ 0 & a & 0 \\ 0 & 0 & b \end{bmatrix} \tag{4.45}$$

In the backscattering geometry (incident and scattered light along the c-axis of the sample) the intensity of this Raman peak is $\propto \mathrm{a}^2\cos^2(\phi)$ where, as before, ϕ indicates the angle between the incident and scattered electric field polarization vectors. The other vibration present in the Raman spectra exhibits $E^{'}$ symmetry:

$$R_1^{E^{'}} = \begin{bmatrix} 0 & f & 0 \\ f & 0 & 0 \\ 0 & 0 & 0 \end{bmatrix} \; R_2^{E^{'}} = \begin{bmatrix} f & 0 & 0 \\ 0 & -f & 0 \\ 0 & 0 & 0 \end{bmatrix} \tag{4.46}$$

This mode is infrared active and obviously doubly degenerate. In the back scattering geometry only the TO branch can be excited and its intensity is independent of the orientation of the incident and scattered electric field polarization. $E^{''}$ is the representation of the last Raman active mode and its Raman tensors are:

$$R_1^{E^{''}} = \begin{bmatrix} 0 & 0 & 0 \\ 0 & 0 & d \\ 0 & e & 0 \end{bmatrix} \; R_2^{E^{''}} = \begin{bmatrix} 0 & 0 & -d \\ 0 & 0 & 0 \\ -e & 0 & 0 \end{bmatrix} \tag{4.47}$$

Inspection of the two matrices in Eq. 4.47 immediately reveals that the mode cannot be excited in the back scattering configuration, $z(xy)\bar{z}$.

A brief description of the experimental setup is necessary to correctly interpret the experimental data. The sample was mounted inside a cryostat in such a way that the c-axis (labeled Z from now on) was oriented toward the entrance port of the spectrometer. The full back scattering geometry was the preferred choice since the sample was too thin to access it from the X or Y direction. The linear polarization of the incident electric field was changed through a $\lambda/2$ plate while the scattered light polarization was forced through a broad band polarizer to be perpendicular to the grating grooves to achieve the maximum diffraction efficiency. The focusing lens had a 150mm focal length while the collimating lens a 50mm

focal length to collect the largest possible solid angle. Raman data was recorded by a *Dilor*-XY multichannel spectrometer and a *SPEX*1404 single channel spectrometer. The latter was particularly useful when measuring modes very close to the laser line. The entrance and exit slits of both spectrometers were set at 200μm. A prism based monochromator was inserted into the laser path to attenuate the Argon laser plasma lines and narrow the broad Ti:Sapphire spectrum. An additional $\simeq$ 3nm band pass filter centered around 780nm was placed after the Ti:Sapphire output coupler to filter out even further the elastic scattering.

Fig. 4.18 shows the room temperature Raman spectrum for the 514.5nm laser line; the incident power was set at $\simeq$ 5.2mW. By changing the polarization of the incident electric field, the different behavior of two $A_1^{'}$ and two $E_1^{'}(TO)$ modes can be easily recognized.

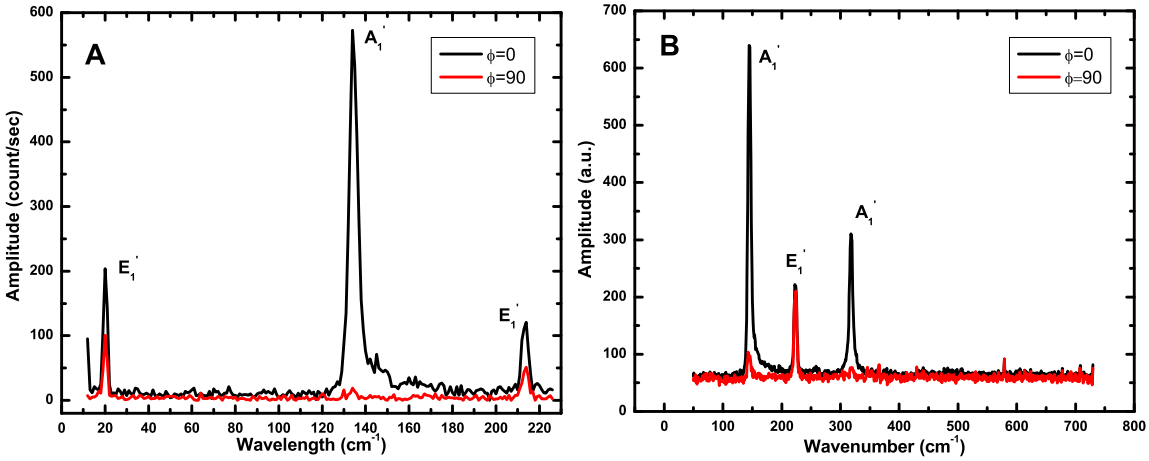

Figure 4.18: (A): Raman spectrum of GaSe at 300K measured by a *SPEX*1404 spectrometer, $\lambda_L = 514.5$nm (B): Raman spectrum measured by a *Dilor*-XY spectrometer.

The frequencies of the peaks marked in Fig. 4.18 are summarized in the first column of Table 4.1 and match closely values already reported in the literature [82]. A similar experiment was carried out after shifting the laser wavelength to 476.5nm. The result is that the mode frequencies and their relative amplitudes remained unchanged. In contrast, the Raman spectrum undergoes two significant changes when the laser line is moved below the gap to 780nm (see Fig. 4.19 and the second column of Table 4.1). The 213cm^{-1} peak splits into a doublet and a new mode emerges at 252cm^{-1}. This latter feature has been observed previously [82] and associated to either the $A_2^{''}$ mode or the LO branch of the $E^{'}$ mode. It turns out that the $A_2^{''}$ is Raman forbidden and the LO mode cannot be detected in the back scattering geometry. Therefore the presence of either one is attributable to leakage

or disorder induced-scattering. It is more challenging to make sense of the 208cm^{-1} and 212cm^{-1} peaks especially because, to the best of our knowledge, this is the first time they have been observed and discussed. At first it may appear that the doublet is simply due to the lifted degeneracy of the $E^{'}$ mode; that is, the laser could induce in the sample a mechanical stress, for instance by heat transfer, sufficient to break the symmetry in the XY plane. However, this argument falls apart after noticing that the same splitting does not occur when the sample is probed by the 514.5nm Argon line (see Fig. 4.18-B). In fact, at this wavelength, a significant fraction of the power is transfered to the sample given the large absorption coefficient of GaSe (see Fig. 4.16-A) and thus the symmetry breaking process should be even more efficient.

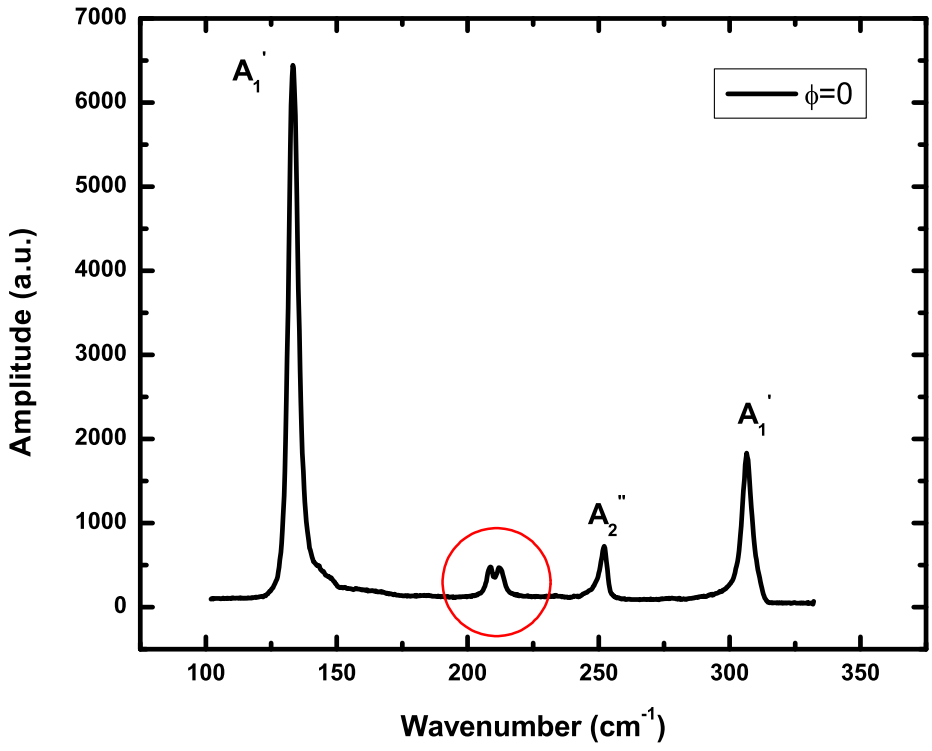

Figure 4.19: Raman spectrum of GaSe at 300K, $\lambda_{\mathrm{L}} = 780$nm.

A more convincing explanation can be found by approaching the problem within the framework of the phonon polariton theory discussed in Section 4.1. Since the $E^{'}$ mode is infrared active, when it interacts with light it turns into a phonon polariton mode with the disper-

FREQUENCY $\lambda_L = 514.5$nm	FREQUENCY $\lambda_L = 780$nm	SYMMETRY MODE
20cm^{-1}	20cm^{-1}	$E^{'}$
134cm^{-1}	133cm^{-1}	$A_1^{'}$
	208cm^{-1}	
213cm^{-1}	212cm^{-1}	$E^{'}$(TO)
	252cm^{-1}	$A_2^{''}$
307cm^{-1}	306cm^{-1}	$A_1^{'}$

Table 4.1: Summary of observed Raman modes at 300K at two different laser wavelengths, 514.5nm (above the gap) and 780nm (below the gap).

sion relation shown in Fig. 4.2-B. As seen in Sec. 4.4, polaritons can be probed through Raman spectroscopy. Fig. 4.20 shows the $E^{'}$ polariton lower branch dispersion curve and the points in the $\omega - k$ plane accessible through Raman spectroscopy in the case of forward scattering and backward scattering. It is evident that in the backward scattering geometry the dispersion curve is intersected near the asymptotic values (ω_{TO}) while, in the forward scattering case, a lower frequency is detected. Using the optical constants of GaSe (i.e. n and $\frac{dn}{d\omega}$) the two frequencies already measured experimentally were recovered: 208cm^{-1} and 212cm^{-1}. Hence, both these modes are attributed to the lower branch of the transverse $E^{'}$ phonon polariton mode.

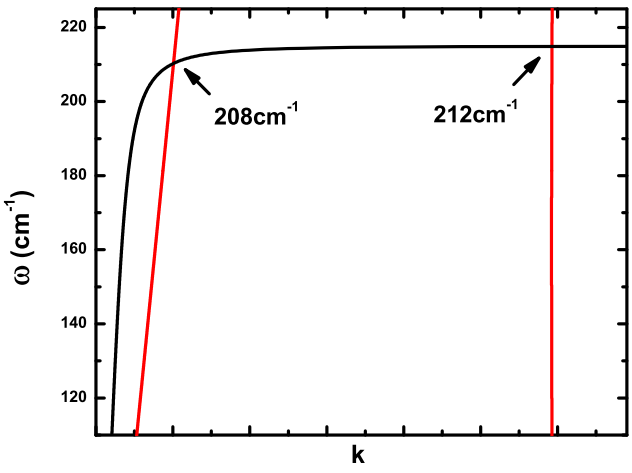

Figure 4.20: GaSe $E^{'}$ phonon polariton dispersion and intersection with the Raman line in forward ($208cm^{-1}$) and backward scattering ($212cm^{-1}$).

It is crucial to note here that the forward scattering signal, in principle incompatible with

the $z(xy)\bar{z}$ geometry, is generated by the laser beam reflection at the back interface of the sample and, as a result, it is present only when the sample is transparent. This ultimately explains the difference between Fig. 4.18 and Fig. 4.19. It would be an oversimplification to examine solely the perfect backward and forward scattering case: the collimating lens is capable of collecting the light scattered in a cone whose aperture is determined by the focal length and the diameter of the lens.

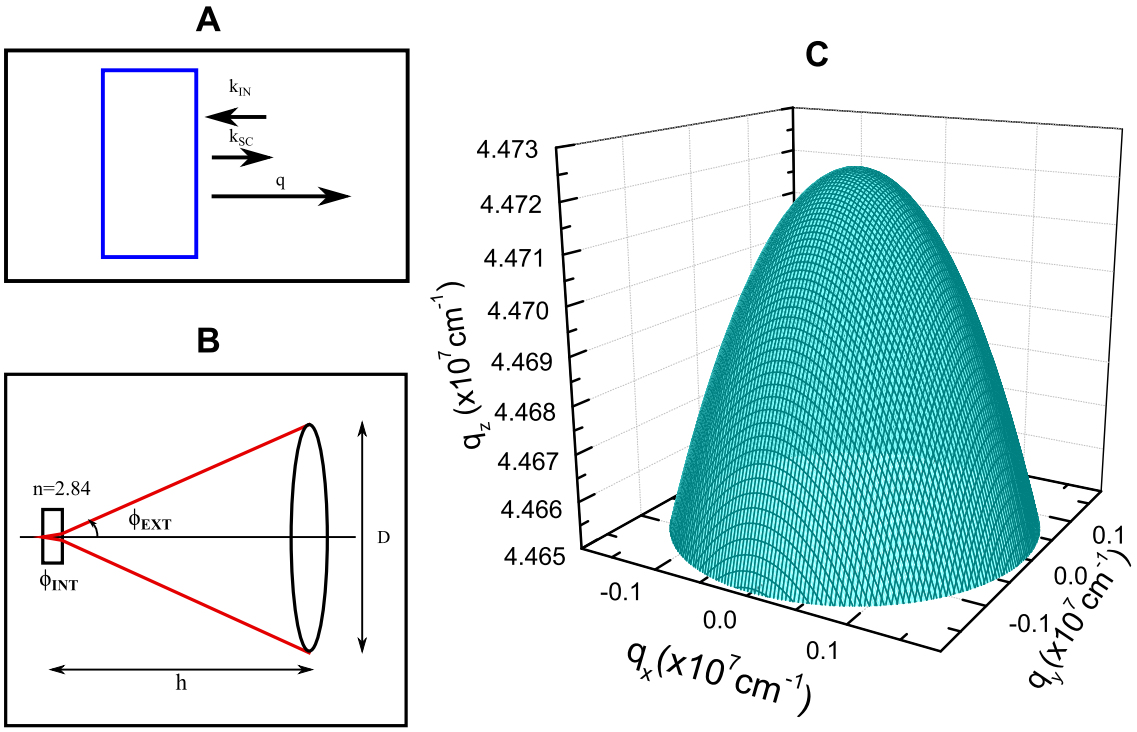

Figure 4.21: (A) Backward scattering wave vector arrangement (B) Collection geometry (C) Excited polariton wave vector surface.

Accounting for all the collected scattered wave vectors, a range of allowed polariton q-vectors, Δq, and frequencies, $\Delta\omega$, can be identified around the two intersections shown in Fig. 4.20. All the possible combinations of the three Cartesian components of the polariton **q** vector can be seen in Fig. 4.21-C for the backscattering geometry, shown in Fig. 4.21-A. This curve has been derived considering the setup sketched in Fig 4.21-B. The collimating lens focal length h = 5cm and diameter D = 2.5cm result in an external collection angle

$\phi_{EXT} \simeq 14^\circ$ and an internal angle $\phi_{INT} \simeq 4.89^\circ$. The wave vector of the polariton defines a paraboloid surface in the reciprocal space: when $\phi = 0$ $\mathbf{q}$ is parallel to the c-axis so $q_x = q_y = 0$ while for larger collection angles the in-plane components (q_x and q_y) are excited as well. The continuous range of frequencies ($\Delta\omega$) that can be excited on the polariton dispersion is obviously related to the width of the two peaks in Fig. 4.19.

4.6.5 Faust-Henry coefficient

The Raman scattering cross section, presented in Sec. 2.2.2, can be extended to the case of phonon polaritons. A polariton, as opposed to a purely mechanical phonon, carries a time-varying transverse electric field that, analogously to a lattice vibration, can induce a change in the dielectric susceptibility:

$$\delta\chi_{\mu\nu} = \sum_{\lambda} a_{\mu\nu\lambda}\epsilon_\lambda \sqrt{\frac{V_C}{M_R}} W + b_{\mu\nu\lambda}\epsilon_\lambda E \tag{4.48}$$

where $\hat{\epsilon}W$ was defined in Eq. 4.2, $\hat{\epsilon}E$ is the electric field, while $a_{\mu\nu\lambda}$ and $b_{\mu\nu\lambda}$ are respectively the deformation potential and the electro optic coefficient. Using Eq. 4.6, E can be expressed as a function of W so that Eq. 4.48 becomes:

$$\delta\chi_{\mu\nu} = \sum_{\lambda} \epsilon_\lambda [a_{\mu\nu\lambda} + \frac{M_R}{e^*}(\omega_{\mathrm{TO}}^2 - \omega^2) b_{\mu\nu\lambda}] \sqrt{\frac{V_C}{M_R}} W \tag{4.49}$$

$\delta\chi_{\mu\nu}$ is then used to write the Raman scattering cross section:

$$\frac{d\sigma}{d\Omega d\omega_S} = \frac{\hbar\omega_I \omega_S^3 V \upsilon n_S}{(4\pi\epsilon_0)^2 2c^4 n_I \omega_{\mathrm{TO}}} \left| \sum_{\mu\nu\lambda} x_S^\mu x_I^\nu \epsilon_\lambda [a_{\mu\nu\lambda} + \frac{M_R}{e^*}(\omega_{\mathrm{TO}}^2 - \omega^2) b_{\mu\nu\lambda}] \right|^2 L_P(\omega)(1 + n_\omega) g_\omega(\omega_S) \tag{4.50}$$

where $\hat{x}_I$ and $\hat{x}_S$ are unit vectors parallel to the polarization of the incident and scattered electric field. To establish whether the Raman and the electro optic effect add up or subtract and to identify the relative strength of the two processes, it is customary to refer to the Faust-Henry coefficient [83]:

$$C = \frac{a}{b} \frac{e^*}{M_R \omega_{\mathrm{TO}}^2} \tag{4.51}$$

In Eq. 4.51, for the sake of simplicity, $a_{\mu\nu\lambda}$ and $b_{\mu\nu\lambda}$ have been assumed to be scalar quantities (a and b). The Faust-Henry coefficient of several materials, such as GaAs, GaP, ZnS, ZnSe, has been measured [83, 84, 85, 86, 87] or theoretically calculated [88]. In order to estimate C, it is necessary to measure the Raman cross section at two different frequencies. This is usually possible when the TO and LO mode can both be detected in the same geometry. Although the LO mode is forbidden by the selection rules, two separate frequencies stemming from the same mode are nonetheless available in the Raman data and thus the value of C can be extracted. After defining $x = \frac{A(\omega_f)}{A(\omega_b)} \frac{1+n(\omega_f)}{1+n(\omega_b)}$, A being the area underlying the peaks at frequencies ω_f ($208cm^{-1}$) and ω_b ($212cm^{-1}$) and n the Bose-Einstein coefficient, C can be written as:

$$C = \frac{1 - \frac{\omega_f^2}{\omega_b^2}}{\sqrt{\frac{x}{RL_P}} - 1} \tag{4.52}$$

where $R \simeq 0.23$ is the reflection coefficient for normal incidence. Substitution of the numerical values acquired from the Raman spectrum leads to $C \simeq 0.044$.

4.6.6 Stimulated Raman scattering

The study of GaSe will be concluded by presenting the pump probe experimental data and interpreting it according to the model used for spontaneous Raman. As previously mentioned, the measured variable was always the differential transmission ($\frac{\Delta T}{T}$) of the probe beam as a function of the pump-probe time delay.

Experiments performed above the gap were done by employing a visible OPA whose output was compressed through a prism pair to compensate for dispersion (the pulse width was consistently $\tau \simeq 80$fs). The Regenerative Amplifier, used in measurements below the gap, provided a shorter compressed pulse $\tau \simeq 75$fs. The pump and probe power were set at 1.7mW and 600μW respectively to avoid burning the sample or saturating the photo detector. The Raman tensors introduced in Eq. 4.45 and Eq. 4.46 can be employed to calculate the selection rules, namely, the intensity of the $E^{'}$ mode is $\propto \cos(2\phi)$ while the $A_1^{'}$ mode is isotropic. The $A_1^{'}$ signal was dominant and tended to obscure the weaker $E^{'}$ oscillations. The polarization sensitive detection scheme depicted in Fig. 3.11 was thus used to cancel

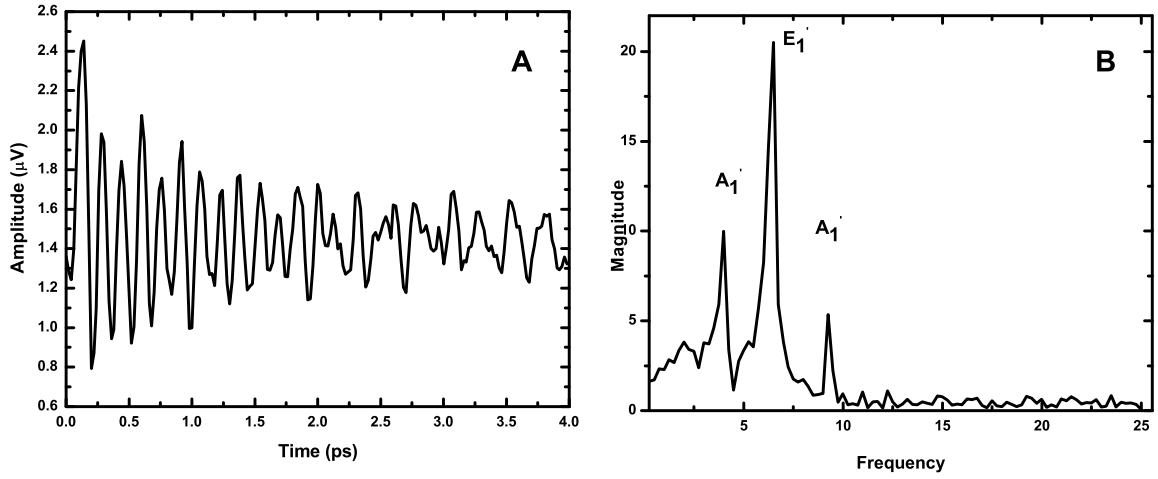

Figure 4.22: 30K pump probe data (A) and FFT (B) on GaSe at $\lambda_L = 514$nm.

the $A_1^{'}$ mode and enhance the $E^{'}$ one. The time domain signal at 30K relative to a 514nm laser line is shown in Fig. 4.22-A. The data was collected in the $\phi = 45°$ balanced configuration. The FFT spectrum (Fig. 4.22-B) reveals the presence of three distinct frequencies which correspond to the two $A_1^{'}$ modes at 4THz and 9THz and the $E^{'}$ mode at 6.3THz (see Table 4.1). The lower frequency $E^{'}$ peak (0.6THz) was not observed.

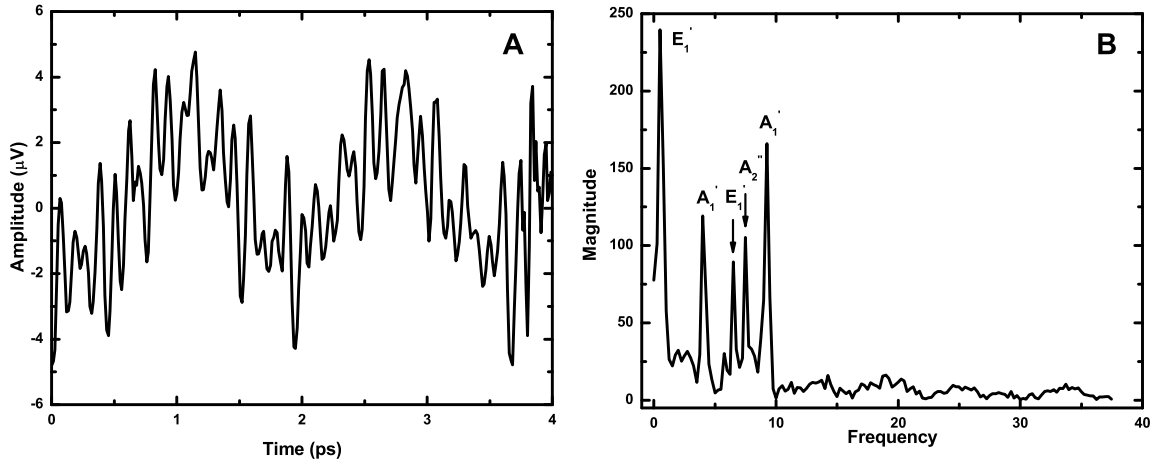

Figure 4.23: 30K pump probe data (A) and FFT (B) on GaSe at $\lambda_L = 800$nm.

The same experiment carried out at 800nm (Fig. 4.23-A) led to a substantially different spectrum (see Fig 4.23-B). The presence of two additional features, the 0.6THz mode and the 7.5THz Raman forbidden $A_2^{''}$ mode, makes the pump probe spectrum closely comparable to the spontaneous Raman one shown in Fig. 4.19. The absence of a doublet at the $E^{'}$ mode frequency seems to confirm our theory: only the lower frequency peak (Fig. 4.20) can be

excited in a forward scattering measurement, like ISRS.

Taking advantage of the tunable wavelength output of the OPA, it was possible to study the dependence on the laser wavelength of the oscillation amplitude of the $A_1^{'}$ and 0.6THz $E^{'}$ modes. Fig. 4.24 gives a summary of the results when T = 10K. The strength of both modes reaches a maximum around the band gap frequency where the absorption is the highest. This behavior is consistent with the two Raman tensor theory and has already been extensively discussed by Stevens et al. [2]. Moreover, it is possible to note the drastic drop in the $E^{'}$ mode amplitude once the wavelength is lower than 600nm. In contrast to its counterpart at 6.3THz, in ISRS experiments the 0.6THz $E^{'}$ mode vanishes above the gap.

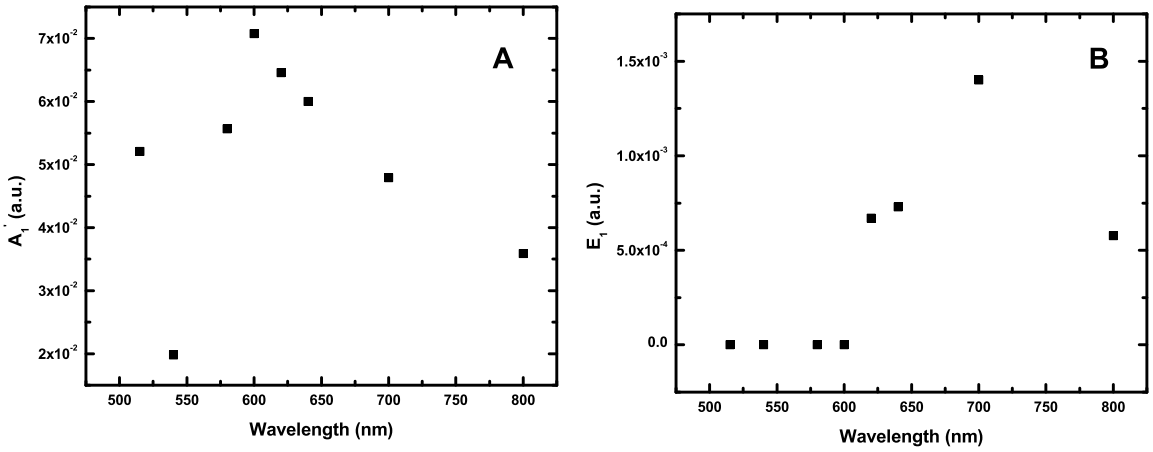

Figure 4.24: 10K $A_1^{'}$ (A) and 0.6THz $E^{'}$ (B) oscillation amplitudes as a function of the laser wavelength.

4.6.7 Spontaneous and Stimulated Raman scattering Comparison

The conclusions drawn at the end of the previous section make it clear that it was not possible to compare the deformation potentials of the two phonon modes. However, the initial plan was not completely abandoned: the same kind of comparison was performed between a purely mechanical phonon mode ($A_1^{'}$) and a phonon polariton (6.3THz $E^{'}$). In order to correctly extract the Raman matrix element (including both deformation potential and electro optic contribution) from the experimental data, it is critical to scale the measured oscillation amplitude by the proper coefficients. In the case of spontaneous Raman, it is necessary to take into account the dependence of the scattering cross section on three factors. They can be identified looking at Eq. 2.27: the Bose Einstein term (n), the phonon

frequency (ω_σ) and, in the case of the $E^{'}$ mode, the fact the mode is not generated by the incident beam but rather by its reflection from the back surface. As regards ISRS, since the interface effects are negligible, the only required correction is the one relative to the finite pump and probe pulse width, see Eq. 2.40. The 780nm (Raman) and 800nm (pump probe) data will be first analyzed. According to the discussion in Sec. 2.3.1, it seems reasonable to expect that the ratio of the $A_1^{'}$ and $E^{'}$ deformation potentials calculated from Raman and pump probe data should essentially be the same.

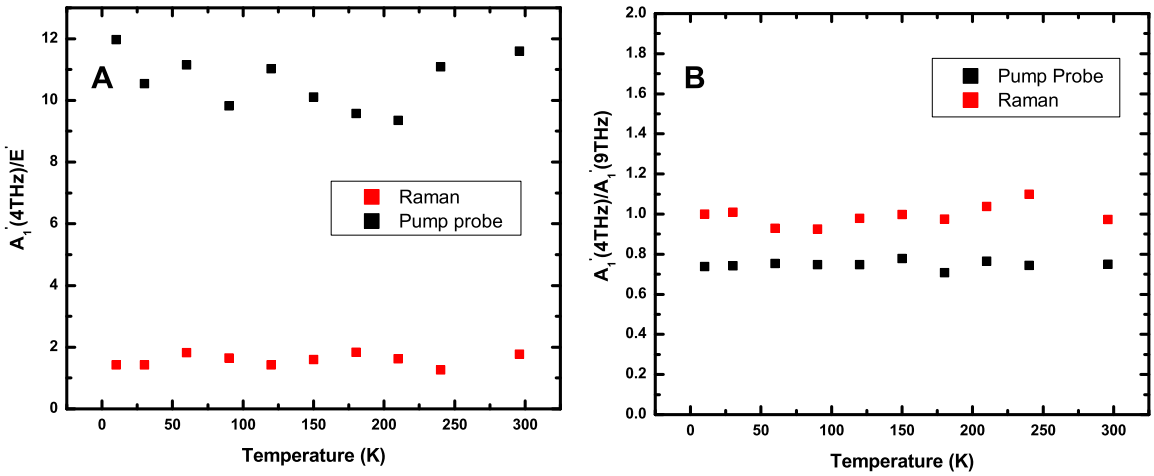

Figure 4.25: Below the gap Raman and pump probe comparison. (A) Ratio of the $A_1^{'}$ (at 4THz) and $E^{'}$ deformation potentials as a function of temperature (B) Ratio of the $A_1^{'}$ (at 4THz) and $A_1^{'}$ (at 9.3THz) deformation potentials as a function of temperature.

However, the experimental data contradicted our predictions. Fig. 4.25-A shows the ratio of the $A_1^{'}$ and $E^{'}$ matrix elements as a function of temperature for pump probe and spontaneous Raman. It can be seen that the two sets of data differ by a factor greater than 5. To verify the validity of our mathematical analysis and test the accuracy of our fitting routines, the two $A_1^{'}$ modes' deformation potentials were compared as well. Fig. 4.25-B shows that the Raman and pump probe trends, as expected, almost overlap. Noting that in the ISRS experiments the $E^{'}$ amplitude is somehow lower than in Raman's, a possible interpretation of the data can be developed . The starting point is, once again, the realization that polaritons display both a phonon-like and a wave-like nature, that is, they can be treated as the field of an an electromagnetic wave. Accordingly, the pump beam traveling through the sample at the group velocity of the laser pulse (v_g) generates a point-like cluster of radiating dipoles. It turns out that the dipoles, oscillating at $\Omega = 6.3$THz, propagate through the medium faster

than the speed of light at their oscillating frequency, $\frac{c}{n(\Omega)}$. A charged particle (in our case an oscillating dipole) traveling faster than the speed of light generates what is commonly referred to as Cherenkov radiation [89, 90, 91, 92]. When dealing with Cherenkov radiation it is customary to distinguish between two different regimes: subluminal ($v_g > \frac{c}{n(0)}$) and superluminal ($v_g < \frac{c}{n(0)}$) [93]. Recalling the dispersion of the dielectric constant in the vicinity of a phonon resonance (Fig. 4.2-A), it becomes evident that in the former case the entire polariton branch is engaged, while in the latter one, only those frequencies $\Omega > \Omega_c$ are involved in the radiation process; Ω_c is defined such that $v_g = \frac{c}{n(\Omega_c)}$.

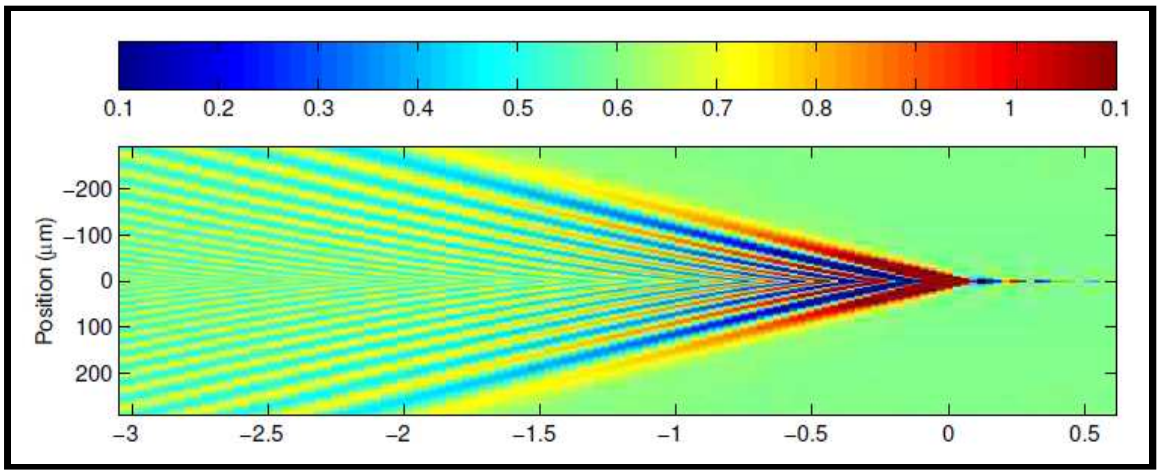

Figure 4.26: Results of a calculation of the Cherenkov electric field due to a point dipole located at $\rho = 0$ and $z - vt = 0$ traveling to the right at speed v through a medium with dispersion given by 4.10, from [94].

In both cases the electric field is not emitted isotropically but rather within a cone whose aperture angle is given by:

$$\theta_c = cos^{-1}(\frac{c}{v_g n}) \tag{4.53}$$

for the superluminal case and by:

$$\theta_c = tan^{-1}(4\frac{\sqrt{(\eta - \zeta)/\xi^3}}{\gamma}) \tag{4.54}$$

for the subluminal case, where $\gamma = \frac{1}{\sqrt{1-\epsilon_\infty v^2/c^2}}$, $\zeta = 2 - \sqrt{4 - 3\eta}$ and $\eta = 1 - (\Omega_c/\Omega_{\mathrm{TO}})$ [95]. Fig. 4.26 shows the simulated electric field spatial and temporal intensity in the superluminal regime and clearly portrays the Cherenkov angle. It is important to observe that the polariton field is confined mainly to the edge of the Cherenkov cone and tends to

fade in the center region right behind the traveling dipoles. The field distribution illustrated in Fig 4.26 is relative to a point source distribution of dipoles. In our experiments the focused spot size of the pump is $\simeq 40\mu$m and is thus effectively point-like compared to the wavelength of the polariton ($\frac{c2\pi}{n\Omega}$). Since the probe spatially overlaps with the pump to enhance the signal strength and is even smaller in size, only the central region of the cone ($\theta = 0$ in Fig. 4.26) is actually scanned. Thus, the scattering cross section extracted from our measurements includes only a portion of the polariton field. As a result, the $E^{'}$ mode Raman matrix element is underestimated, consistently with what is shown in Fig. 4.25.

It would be possible, in principle, to reconstruct the field profile moving the probe beam along the radial direction (ρ) for each value of the pump probe time delay [93]. The $E^{'}$ mode spread across the Cherenkov cone could then be fully accounted for by integrating the experimental data along the ρ direction. This procure would eventually result in a more accurate value for the scattering cross section.

4.7 CdSe

The last section of this chapter is dedicated to CdSe; a II-VI semiconductor known mainly for its applications in quantum dots [96, 97, 98]. Since CdSe has been extensively studied over the years [99, 100, 101] and its Raman and infrared properties are fully understood, it seems unnecessary to review the details of the vibrational spectrum of the material. Rather, only one particular feature, shared by both time domain and frequency domain measurements, will be examined here because it appears to be ascribable to the interaction of light with a surface polariton mode of CdSe.

4.7.1 Material properties

CdSe crystallizes in the wurtzite structure and belongs to the C_{6v} point group [100]. The vibrational representation of CdSe can be decomposed into the irreducible representation [99]:

$$\Gamma_{vib} \equiv A_1 + 2B_1 + E_1 + 2E_2 \tag{4.55}$$

The A_1 and E_1 modes are both Raman and infrared active and transform according to Z and (X, Y) respectively; the E_2 is only Raman active; while the B mode is neither Raman

nor infrared active. The gap of CdSe is located at $\simeq$ 730nm at room temperature and shifts to $\simeq$ 690nm at 75K [102]. The sample used in our measurements is a (0001) double-side polished 1cm $\times$ 1cm $\times$ 1mm CdSe crystal purchased from MTI Corporation. CdSe has a natural tendency to be slightly n-type even when no dopants have been added during the growing process [100]. This was presumably the case for our sample as well.

4.7.2 Experimental data

The Raman scattering spectrum for 514.5nm laser excitation line is shown in Fig. 4.27.

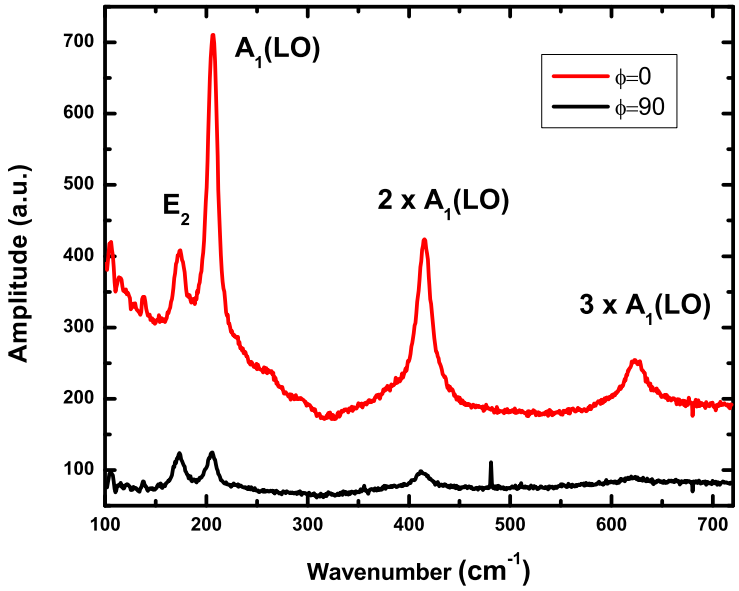

Figure 4.27: CdSe Raman spectrum at $100K$ in back scattering geometry $z(xy)\bar{z}$, $\lambda_{\mathrm{L}} = 514.5$nm

The experimental setup is the same one used for GaSe (Sec. 4.6). The incident power is $\simeq$ 40mW. In the back scattering geometry, $z(xy)\bar{z}$, only two modes can be detected, namely the A_1(LO) and the E_2, both visible in Fig. 4.27. The longitudinal character of the A_1 mode is displayed by the presence of several peaks at frequency multiples of the fundamental one at 210cm^{-1} [103, 104, 105]. The accuracy of our peak labeling has been confirmed by the modes' selection rules tested at two different choices of the incident field polarization. Yet, a closer look at the spectrum reveals the presence of an additional feature which mingles

with the E_2 peak (see Fig. 4.28). The frequency of this unexpected peak coincides very well with the A_1(TO) frequency which should be forbidden in this geometry.

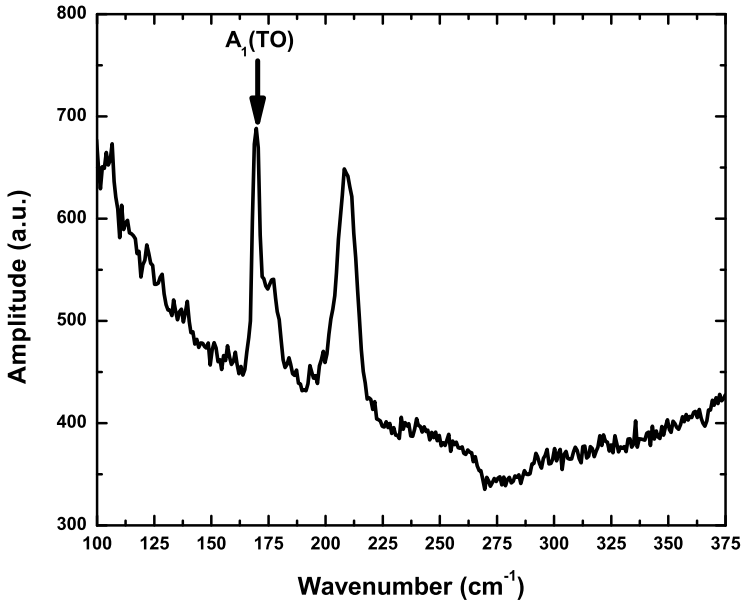

Figure 4.28: Raman spectrum of CdSe at 100K: extra feature at $\simeq 169\text{cm}^{-1}$, $\lambda_{\text{L}} = 514.5\text{nm}$.

Before attempting to justify the anomalous presence of the A_1(TO) mode in the spontaneous Raman spectrum, the corresponding pump probe data will be presented. Since CdSe is highly absorptive at 514.nm, the parameter measured was the differential reflectance ($\frac{\Delta R}{R}$). Fig. 4.29 shows the normalized differential reflectance when the pump and probe power is 1.66mW and 620μW respectively. The linear prediction fitting of the time domain data (inset of Fig. 4.29) reveals the presence of two modes; the A_1(TO) at $\simeq 169\text{cm}^{-1}$ and a second mode at $\simeq 200\text{cm}^{-1}$.

The key to explain these additional features lies in the surface plasmon polariton theory. The first evidence that surface modes had to be included in the picture came from the realization that 200cm^{-1} is the frequency at which the dielectric constant of CdSe equals -1, as can be easily verified using Eq. 4.10 with $\Omega_{\text{LO}} = 211\text{cm}^{-1}$, $\Omega_{\text{TO}} = 169\text{cm}^{-1}$ and $\epsilon_\infty = 7.9$ [106]. As shown in Fig. 4.7-A, a surface plasmon mode is confined between two frequencies, Ω_{TO} and Ω_{D}, and requires a wave vector parallel to the sample surface in order to be launched. In both Raman and pump probe experiments, the laser beam is not

perfectly perpendicular to the GaSe crystal and, as a result, the incident k vector has a non vanishing component along the surface ($k_{\|}$). Moreover, a continuum of $k_{\|}$ values is generated whenever a collimated laser beam is focused down by a lens.

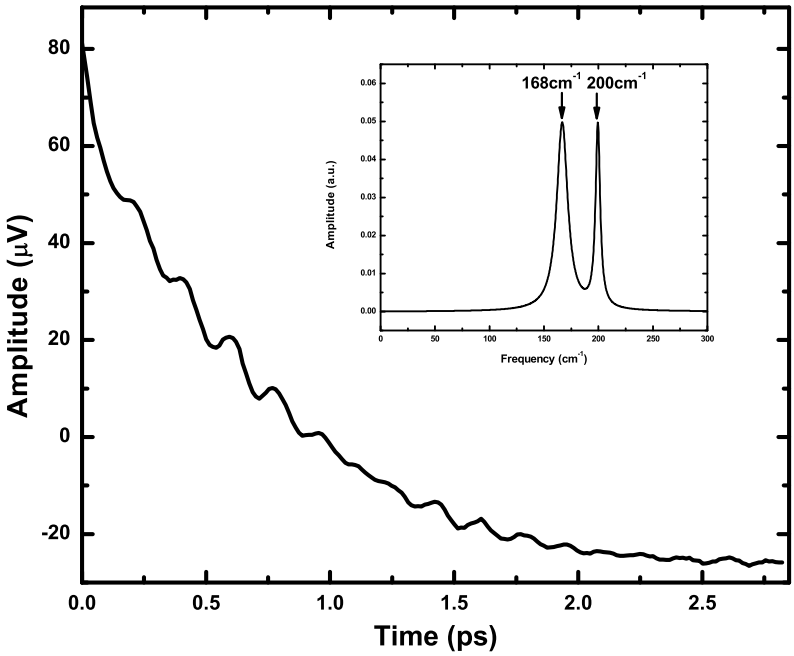

Figure 4.29: ISRS signal on CdSe at 300K, $\lambda_{\mathrm{L}} = 514$nm and, in the inset, frequency spectrum, calculated after fitting the data through the Linear Prediction algorithm.

Since both Ω_{TO} and Ω_{D} are detected, it is obvious that all the other frequencies along the surface plasmon curve can be equally excited. Yet, Fig. 4.29 inset shows only two distinct peaks at ω_{D} and ω_{TO} and none of the intermediate frequencies. To reconcile the theoretical picture with the experimental data, it is necessary to reconstruct the time domain signal, $S(t)$, assuming that all frequencies on the surface polariton branch, shown in Fig. 4.7-A, are excited. Each point on the dispersion relation results in a sinusoidal signal, sin(ωt), in the time domain. Hence, assuming for the sake of simplicity that all oscillators have the same strength, the final signal can be obtained by adding up the contribution from all frequencies

in the $\omega_{\mathrm{TO}} - \omega_{\mathrm{D}}$ range:

$$S(t) \propto \int_{\Omega_{\mathrm{TO}}}^{\Omega_{\mathrm{D}}} \sin(\omega \mathrm{t})\, dt = \frac{\cos(\Omega_{\mathrm{TO}} t)}{t} - \frac{\cos(\Omega_{\mathrm{D}} t)}{t} \tag{4.56}$$

The beating of the two sinusoidal signals in Eq. 4.56 can be clearly observed in Fig. 4.29.

CHAPTER V

Two Pulse Squeezing: Phonon Echo

This chapter is somewhat of a detour from the general theme of the previous three chapters of this thesis: coherent phonons and their interaction with light. The topic is, in fact, a peculiar phenomenon, suggestively named "phonon echo", that characterizes a different kind of vibrational state squeezed phonons. The theory of squeezed phonons, first demonstrated by Garrett and coworkers in 1997 [107], is developed in Sec. 5.1 in close analogy with the concepts introduced in Chap. II. Sec. 5.2 shows how the echo effect emerges when squeezed phonons are generated in the context of a double pump experiment. The chapter concludes with a review of a set of simulations carried on to validate the theory and set the guidelines for a potential experiment designed to measure the echoes.

5.1 Coherent and Squeezed Phonons

5.1.1 Coherent Phonons Revisited

In order to discuss again coherent phonons, it is helpful to rewrite the equation of motion neglecting damping:

$$\frac{d^2q}{dt^2} + \omega^2 q = 2F(t) \tag{5.1}$$

A factor of two has been added to the right hand side of Eq. 5.1 for computation convenience. The driving term, that was derived formally in Eq. 2.48, can be related to the electrical susceptibility recalling that the energy density stored in a medium is given by $E = \frac{1}{2}\mathbf{P} \cdot \mathbf{E}$ and the polarization vector can be written as $\mathbf{P} = \chi\mathbf{E}$. Similarly to what was done in

Eq. 2.41, it is possible to expand χ as a function of the normal mode coordinate $q(t)$:

$$\chi(t) = \chi_0 + \left.\frac{\partial \chi}{\partial q}\right|_0 q(t) + \frac{1}{2}\left.\frac{\partial^2 \chi}{\partial q^2}\right|_0 q^2(t) + ... \tag{5.2}$$

In the case of coherent phonons, only the second term in the expansion, the one depending linearly on $q(t)$, is retained and the force becomes:

$$2F(t) = \frac{1}{2}\left.\frac{\partial \chi}{\partial q}\right|_0 |\mathbf{E}|^2 \tag{5.3}$$

After replacing $2F(t)$ with Eq. 5.3 and using a delta function approximation for the electric field intensity, i.e. $F(t) = \lambda\delta(t)$, the solution of Eq. 5.1 is:

$$q(t) = Dsin(\omega t + \varphi) \tag{5.4}$$

where $Dsin(\varphi) = q_0$ and $Dcos(\varphi) = \frac{\dot{q_0}}{\omega} + 2\frac{\lambda}{\omega}$, q_0 and $\dot{q_0}$ are here the initial value of the phonon position and momentum. Eq. 5.4 is the analog of Eq. 2.33 and describes the dynamic of a coherent phonon: when the laser pulse hits the sample the phonon mode amplitude remains unchanged, but its derivative, i.e., the phonon momentum p, undergoes a sudden increase as shown in Fig. 5.1-A.

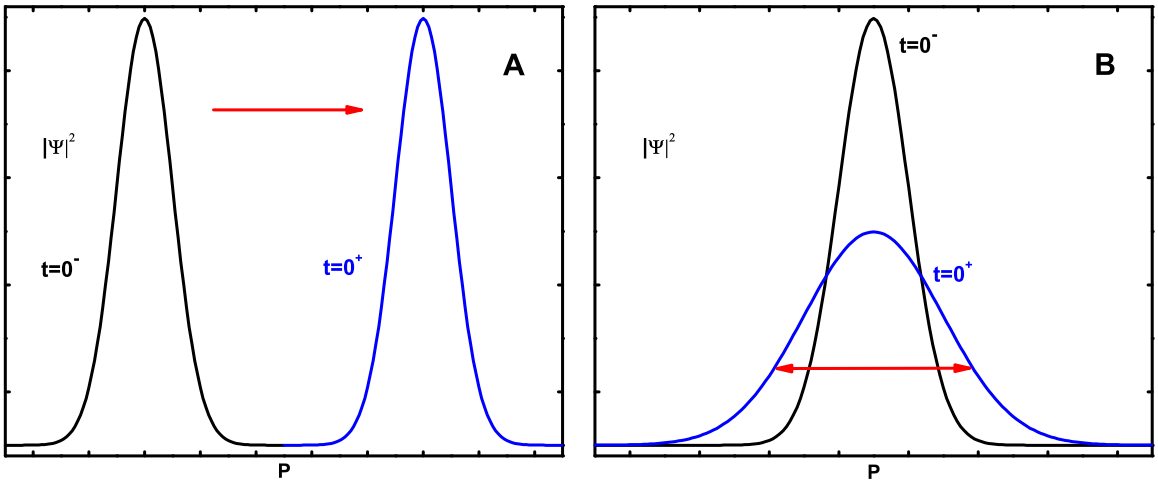

Figure 5.1: Eigenfunction of a coherent (A) and squeezed (B) phonon in the momentum space before and after $t = 0$, when the laser pulse reaches the sample.

The behavior of a coherent phonon can be more clearly visualized in phase space, i.e., the

$q-p$ plane. The energy equipartition principle [108] states that the energy associated with a single lattice mode with frequency ω is given by:

$$\frac{< p >^2}{2m} + \frac{< q >^2 \omega^2 m}{2} = kT \tag{5.5}$$

where m is the ion mass (assuming that all the ions are the same), k the Boltzmann constant and T the temperature in degree Kelvin. <> indicates the thermal average. Operating in the microcanonical ensemble and renormalizing q and p:

$$\begin{aligned} P &= p\frac{1}{\sqrt{2kTm}} \\ Q &= q\omega\sqrt{\frac{m}{2kT}} \end{aligned} \tag{5.6}$$

an unperturbed phonon mode is represented by a sequence of points rotating at angular velocity ω on a unitary radius circumference, see Fig. 5.2-A.

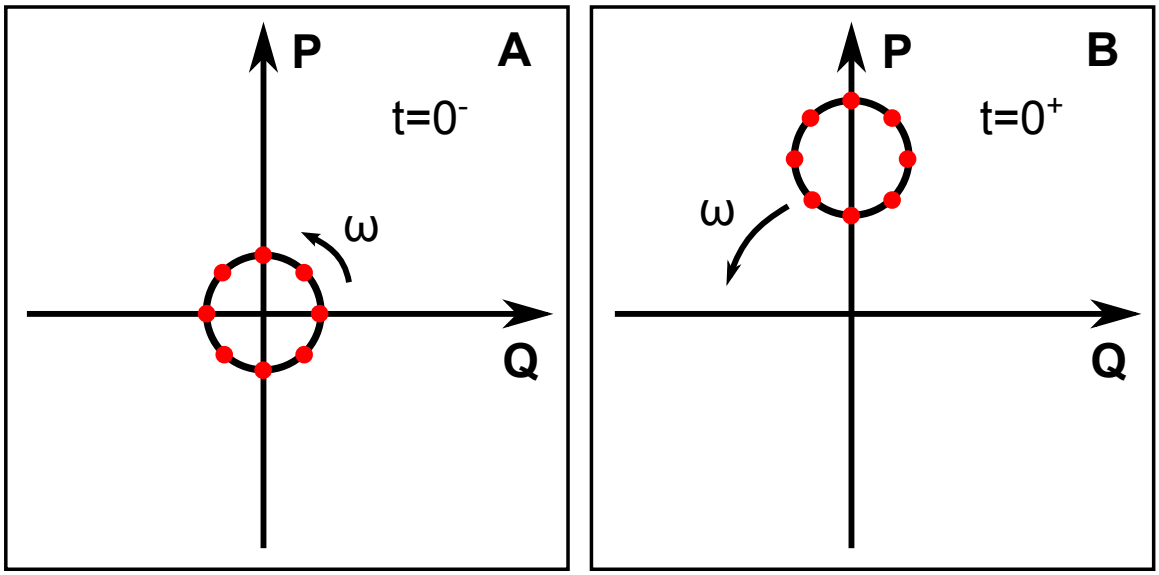

Figure 5.2: Representation of a coherent phonon in the phase space: the circle associated to a particular phonon mode is displaced along the momentum axis by an impulsive driving force and starts rotating around the center at angular velocity ω, so that $< Q > \propto sin(\omega t)$.

After the arrival of the laser pulse the circumference is shifted along the momentum axis and starts orbiting around the axes center, as shown in Fig. 5.2-B, so that Q and P oscillate harmonically at frequency ω. Comparing Fig. 5.2-A and Fig. 5.2-B, it can be noted that, even though the interaction with the laser light modifies the phonon expectation value,

$< Q >$, its variance $< Q^2 >$ remains unaffected: the circle shape and area do not change.

5.1.2 Squeezed Phonons

A substantially different scenario is encountered when the force is calculated considering the second order term in Eq. 5.2:

$$2F(t) = \frac{1}{2}\frac{\partial^2 \chi}{\partial q^2}\bigg|_0 q(t)|\mathbf{E}|^2 \tag{5.7}$$

Maintaining the same notation used in the coherent phonon case, the driving force can be written as $F(t) = \lambda q(t)\delta(t)$ so that the solution of Eq.5.1 reads:

$$q(t) = W sin(\omega t + \varphi) \tag{5.8}$$

where now $W sin(\varphi) = q_0$ and $W cos(\varphi) = \frac{\dot{q_0}}{\omega} + \frac{2\lambda}{\omega} q_0$. Hence a broadening, rather than a rigid translation, is induced in the phonon momentum, as depicted in Fig. 5.1-B. Equivalently, in phase space, a driving term linearly dependent on q deforms the original circle into an ellipse (hence the name "squeezing") which keeps rotating at angular velocity 2ω.

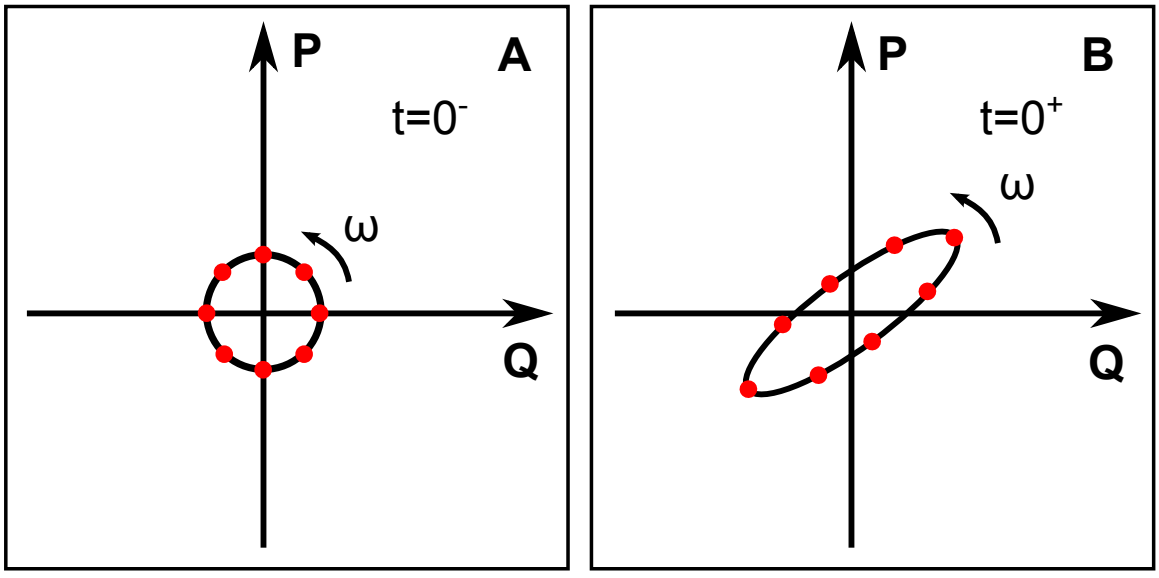

Figure 5.3: Representation of a squeezed phonon state in phase space: the circle associated to a particular phonon mode is deformed into an ellipse that rotates around the center at angular velocity 2ω so that $< Q >= 0$ but $< Q^2 > \propto sin(2\omega t)$.

As opposed to $< Q >$ and $< P >$ which remain constantly zero since the ellipse is not off

centered, $< Q^2 >$ and $< P^2 >$ begin to oscillate in time at twice the mode frequency as shown in Fig. 5.3. The detection of squeezed phonons, in exact analogy with their coherent counterpart, takes place reversing the generation mechanism: probing the changes that an oscillation in $< Q^2 >$ induces in the dielectric constant, see Eq. 5.2. Obviously this is more easily accomplished in materials where $\left.\frac{\partial \chi}{\partial q}\right|_0 \simeq 0$ so that only squeezed phonons are effectively generated and their detection is not obscured by other stronger interferences. It turns out that this is actually the case in several perovskite crystals, such as $KTaO_3$ and $SrTiO_3$ [25]. In 1997 Garrett et al. [107] performed several ISRS experiments on $KTaO_3$ detecting a signal at a frequency, $\simeq 3.5$THz, which is very close to twice the frequency of one of the TA modes of the material at the X-point of the Brillouin zone, see Fig. 5.4. Through careful comparison with second order spontaneous Raman scattering, the authors proved that they effectively measured the squeezed phonon field, extracted the squeezing factor, $1 - \frac{<u^2(t)>}{<u^2(0)>}$ (where $u(t)$ is the ions' displacement introduced in Chap. II), and showed its linear dependence on the pump power consistently with the theoretical predictions.

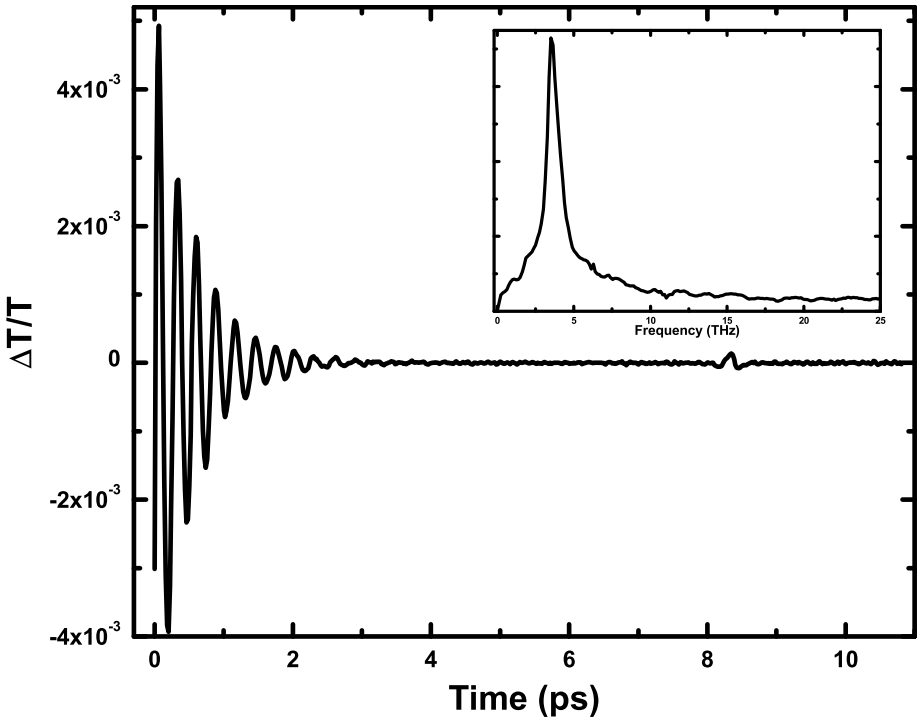

Figure 5.4: Room temperature normalized differential transmittance through a $\sim 1mm$ thick $KTaO_3$ sample. The frequency retrieved, see FFT trace displayed in the inset, is $KTaO_3$ and corresponds to twice the frequency of the $KTaO_3$ TA mode at the X-point of the Brillouin zone.

5.2 Echo

The novelty of this work consists in studying the behavior of squeezed phonons when they are generated by two distinct light pulses separated by a time delay t^*. Although the mathematical formulation of the "two pump" experiment is fundamentally the same as the previous section's, the final outcome of the analysis is unexpected. In fact, both theory and simulations show that when a squeezed phonon field is generated by two pulses separated by a delay Δt, an oscillatory signal arises at time $2\Delta t$ after the initial excitation. To get a broader perspective on the matter, the two pump generation process will be treated both classically, along the lines of Sec. 5.1, and quantum mechanically.

5.2.1 Classical approach

Considering now excitations by two pulses arriving successively, the only modification needed in the equation of motion, Eq. 5.1, pertains to the driving force, $F(t)$:

$$F(t) = q(t)\ [\,\lambda\delta(t) + \mu\delta(t - t^*)\,] \tag{5.9}$$

When $t < t^*$ the solution is given by Eq. 5.8, while, when $t > t^*$, $q(t)$ can still be written as:

$$q(t) = Z\sin(\omega(t - t^*) + \theta) \tag{5.10}$$

and by applying the boundary conditions it is possible to determine Z and θ:

$$\begin{aligned} Z\sin(\theta) &= \sin(\omega t^*)\left(\tfrac{\dot{q}_0}{\omega} + \tfrac{2\lambda}{\omega}q_0\right) + q_0\cos(\omega t^*) \\ Z\cos(\theta) &= \cos(\omega t^*)\left(\tfrac{\dot{q}_0}{\omega} + \tfrac{2\lambda}{\omega}q_0\right) - q_0\sin(\omega t^*) + \tfrac{2\mu}{\omega}Z\sin(\theta) \end{aligned} \tag{5.11}$$

Inserting Eq. 5.11 in Eq. 5.10 leads to the final expression of $q(t)$ when $t > t^*$:

$$q(t)\Big|_{t>t*} = \sin(\omega t)\left(\frac{\dot{q}_0}{\omega} + \frac{2\lambda}{\omega}q_0\right) + q_0\cos(\omega t) + \frac{2\mu}{\omega}\sin(\omega(t-t^*))\left[\sin(\omega t^*)\left(\frac{\dot{q}_0}{\omega} + \frac{2\lambda}{\omega}q_0\right) + \cos(\omega t^*)q_0\right] \tag{5.12}$$

q^2 is obtained by squaring Eq. 5.12:

$$q^2(t) = \left[\sin(\omega t)\left(\frac{\dot{q}_0}{\omega} + \frac{2\lambda}{\omega}q_0\right) + q_0\cos(\omega t)\right]^2$$
$$+\frac{4\mu}{\omega}\sin(\omega(t-t^*))\left[\sin(\omega t)\left(\frac{\dot{q}_0}{\omega} + \frac{2\lambda}{\omega}q_0\right) + q_0\cos(\omega t)\right]\left[\sin(\omega t^*)\left(\frac{\dot{q}_0}{\omega} + \frac{2\lambda}{\omega}q_0\right) + \cos(\omega t^*)q_0\right]$$
$$+\frac{4\mu^2}{\omega^2}\sin^2(\omega(t-t^*))\left[\sin(\omega t^*)\left(\frac{\dot{q}_0}{\omega} + \frac{2\lambda}{\omega}q_0\right) + \cos(\omega t^*)q_0\right]^2 \tag{5.13}$$

The first and second term represent oscillations respectively at $t = 0$ and $t = t^*$. The third term, on the other hand, produces an oscillatory signal that arises at $t = 2t^*$ and can be rewritten, taking a thermal average and using Eq. 5.5, as:

$$\frac{< q^2_{ECHO}(t) >}{< q_0^2 >} = \frac{\mu^2}{\omega^2}\left[\frac{2\lambda}{\omega}\sin(2\omega(t-2t^*)) + \frac{2\lambda^2}{\omega^2}\cos(2\omega(t-2t^*))\right] \tag{5.14}$$

The name "echo" refers to the fact that the oscillations in Eq. 5.14 are delayed with respect to the first pump arrival by twice the time difference between the pumps, t^*, and thus resembles the familiar phenomenon of acoustic echo. It is crucial to emphasize that the echo effect is exclusively associated to the squeezed phonon field and would thus not be observable when just a coherent phonon state is generated.

5.2.2 Quantum mechanical approach

In order to further confirm the validity of the conclusions reached so far, the two pump problem will be now approached from a quantum mechanic viewpoint. When only one phonon mode at frequency ω is considered, the relevant Hamiltonian can be written as:

$$H = \frac{P^2}{2} + \left[\omega^2 - 2F(t)\right]\frac{Q^2}{2} \tag{5.15}$$

where P and Q are defined in Eq. 5.6 and $F(t)$ in Eq. 5.9. Recalling that, given a time dependent operator A, the commutator $[H, A]$ is given by [10]:

$$[H, A] = -i\hbar\frac{dA}{dt} + \frac{\partial A}{\partial t} \tag{5.16}$$

the equations of motion for $\sigma =< Q^2 >$ can be retrieved:

$$\ddot{\sigma} + 4\dot{\sigma}\left[\omega^2 - 2F(t)\right] - 4\dot{F}(t)\sigma = 0 \tag{5.17}$$

The boundary conditions at $t = 0$, when the first impulse arrives, are:

$$\begin{aligned} \Delta\sigma &= 0 \\ \Delta\dot{\sigma} &= 4\lambda\sigma(0) \\ \Delta\ddot{\sigma} &= 2\lambda\left[\dot{\sigma}(0^-) + \dot{\sigma}(0^+)\right] \end{aligned} \tag{5.18}$$

The solution of Eq. 5.17 when $t < t^*$ is:

$$\sigma = \sigma_0[A + \text{sign}(\lambda)\sqrt{A^2 - 1}\sin(2\omega t + \varphi)] \tag{5.19}$$

where $A = 1 + 2\frac{\lambda^2}{\omega^2}$ and $\varphi = -\text{atan}(\frac{\lambda}{\omega})$. When $t > t^*$, Eq. 5.17 has to be solved applying the boundary conditions, listed in Eq. 5.18, at $t = t^*$:

$$\begin{aligned} &\left.\frac{\sigma(t)}{\sigma_0}\right|_{t>t*} = A(1 + 2\frac{\mu^2}{\omega^2}) + 2\frac{\mu}{\omega}\sqrt{A^2 - 1}\cos(2\omega t^* + \varphi) + 2\frac{\mu^2}{\omega^2}\sqrt{A^2 - 1}\sin(2\omega t^* + \varphi) + \\ &+(1 - \frac{\mu^2}{\omega^2})\sqrt{A^2 - 1}\sin(2\omega t + \varphi) - 2\frac{\mu}{\omega}\sqrt{A^2 - 1}\cos(2\omega t + \varphi) + \\ &+2\frac{\mu}{\omega}A\sin(2\omega(t - t^*)) - 2\frac{\mu^2}{\omega^2}A\cos(2\omega(t - t^*)) + \\ &+\frac{\mu^2}{\omega^2}\sqrt{A^2 - 1}\sin(2\omega(t - 2t^*) - \varphi) \end{aligned} \tag{5.20}$$

The last term represents the echo arising at time $t = 2t^*$ and matches exactly what was obtained classically in Eq. 5.14.

5.3 Simulations

In this last section the theoretical results are tested through different simulations designed to mimic the behavior of a distribution of phonons when excited by an impulsive force. Within the framework of the microcanonical ensemble, in the absence of any perturbation, a phonon mode with characteristic frequency ω can occupy a variety of states all with the same energy $k_B T$, see Fig. 5.5-A.

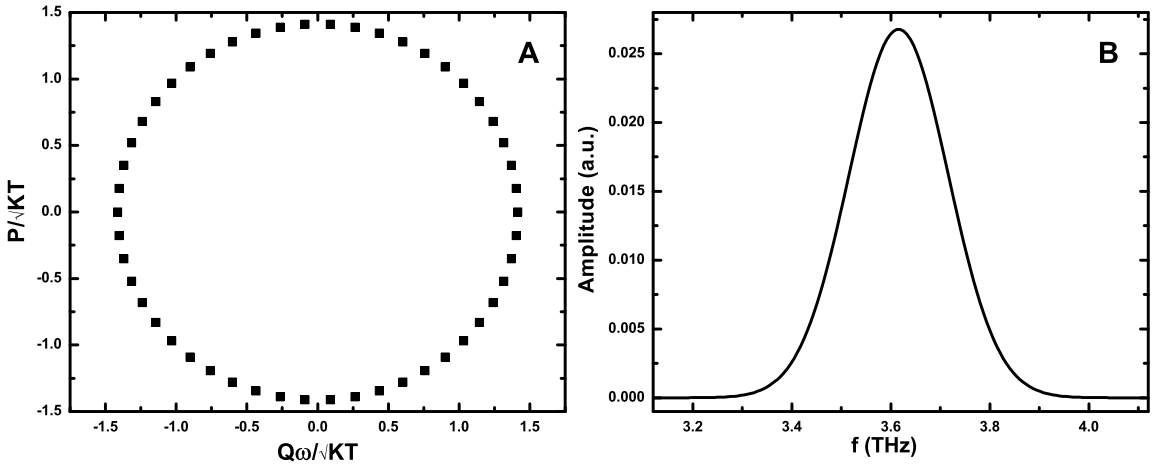

Figure 5.5: (A) Thermal distribution of P and Q for a phonon mode of frequency ω (B) Phonon density of states adopted in the simulations.

These different combinations of Q and P values constitute the allowed initial conditions necessary to solve Eq. 5.1. In this perspective a thermal average is equivalent to averaging the solutions obtained with the system in different initial states. Another aspect that has to be included in the simulations is the phonon spread in frequency: each phonon mode has associated a particular dispersion relation with a corresponding range of frequencies. Since the phonon density of states [7], which indicates which frequencies are the most likely to be excited, has a peak at any existing van Hoove singularity [109], it was approximated by a Gaussian function centered around $f_0 = 3.5$THz, see Fig. 5.5-B. Fig. 5.6 shows a numerical simulation of $< Q^2(t) >$ as defined in Eq. 5.13, obtained by averaging over $N_o = 100$ oscillators distributed like in Fig 5.5. The others parameter were chosen as follows: $\lambda = \mu = \omega_0$, $t^* = 10$ps. Three distinct oscillation bursts at frequency $2\omega_0$ can be observed: at $t = 0$, when the first pump arrives; at t = 10ps, when the second pump reaches the sample; and at t = 20ps, the echo signal. The interaction between sinusoids with different frequency, commonly known as dephasing, is responsible for the decaying character of the oscillatory signal. The decay constant is consequently proportional to the inverse of the phonon density width, Fig. 5.5-B. Both Eq. 5.20 and Eq. 5.13 suggest that the ratio between the echo and the first oscillation amplitude is $\propto \frac{\mu^2}{\omega^2}$. This is actually confirmed in Fig. 5.7 where $< Q^2(t) >$ has been simulated for the case $\lambda = \mu = \omega_0/2$. The simulations presented so far constitute the necessary framework to guide any future experimental effort aimed at measuring the echo signal. In particular, the very pronounced dependence of the

echo amplitude on the pump intensity shows how critical it is to estimate the required conditions, in terms of power, pulse width, repetition rate, in order to successfully carry on the experiments.

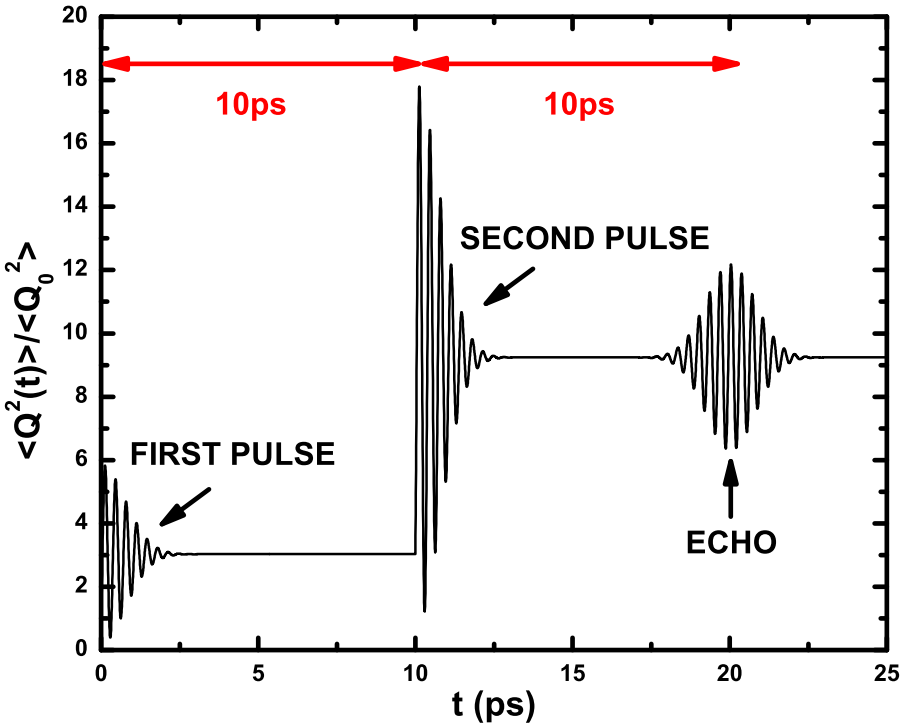

Figure 5.6: Simulated time evolution of $< Q^2(t) >$ when $\lambda = \mu = \omega_0$.

5.4 Experimental Feasibility

The main challenge encountered when trying to measure experimentally the echo signal consisted in detecting its very small amplitude. As both Eq. 5.14 and Eq. 5.20 indicate, the echo is a factor $(\frac{\mu}{\omega})^2$ smaller than the oscillations generated directly by the two pumps. Since the frequency of the lattice vibrations (ω) cannot be changed, the primary concern in the experiments was to maximize μ.

Both μ and λ depend linearly on the laser intensity I_0 [107]:

$$I_0 = \frac{P}{f_R A} \tag{5.21}$$

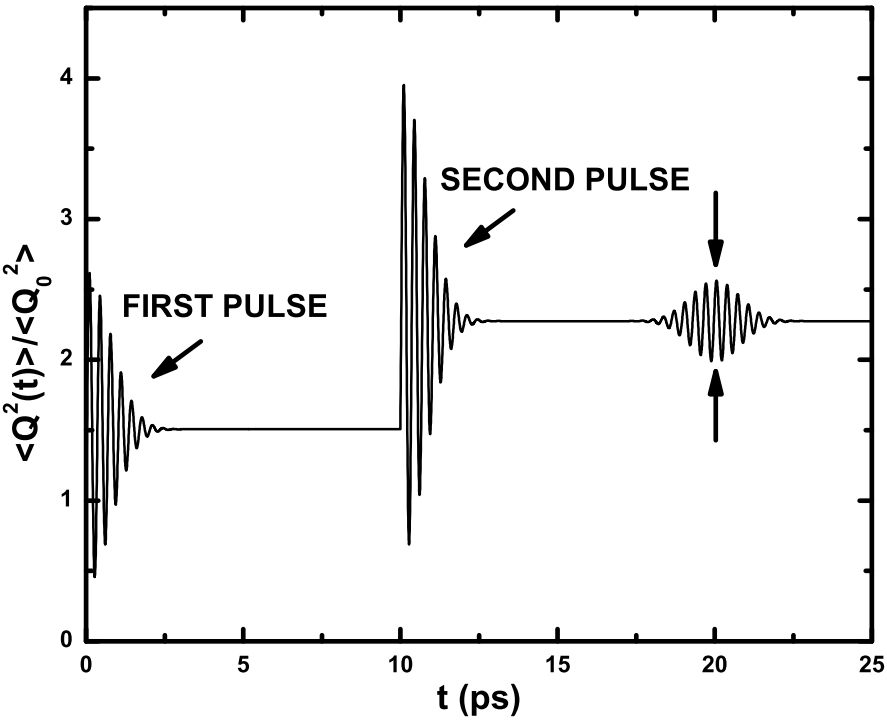

Figure 5.7: Simulated time evolution of $< Q^2(t) >$ when $\lambda = \mu = \omega_0/2$.

where P is the laser average power, f_R the repetition rate and A the pump spot size. All these three parameters were optimized in the course of the measurements. An 800nm Coherent RegA amplifier was always preferred to a Ti:sapphire oscillator due to its significantly higher fluence. The maximum available power was $\simeq$ 400mW for the pump beams and $\simeq$ 80mW for the probe. Short focal length lenses were used to reduce the spot size which ended up being $\simeq 20\mu$m for the pump and $\simeq 10\mu$m for the probe. The amplifier is optimized for a 250kHz repetition rate. Even though it is possible to modify the repetition rate, this usually resulted in a substantial loss of power: when operating the amplifier at 150kHz the average intensity dropped by 30%. Moreover, using the RegA at a frequency different than the one it is designed for always introduces additional noise and power fluctuations. Thus, it turned out to be more effective in terms of overall signal to noise ratio to set f_R to 250kHz.

At 800nm $KTaO_3$ is transparent [110], so the differential transmittance was the physi-

cal quantity measured in all the pump probe experiments. Despite the exceptionally high amplitude of the main oscillations (see Fig. 5.4), the echo could never be detected. This suggests that a further increase in the laser fluence is required to raise the signal amplitude above the noise floor. A possible approach would be to employ a kHz amplifier which could easily provide a more energetic pump beam: 8μJ/pulse [111]. It is instructive to estimate the echo signal amplitude achievable using such an amplifier. If $\frac{\Delta T}{T} \simeq 4 \cdot 10^{-3}$ was obtained at 250kHz repetition rate, 4μJ pulses at 1kHz will increase the first pump oscillations to $\simeq 4 \cdot 10^{-2}$. To calculate the echo signal strength, it is necessary to recall the exact expression for μ [107]:

$$\mu = \frac{R\pi I_0}{nc} \tag{5.22}$$

where R is the Raman tensor ($\simeq 6 \cdot 10^{15}$cm/g in $KTaO_3$), $n = 2.24$ the refractive index and c the speed of light. This results in $(\frac{\mu}{\omega})^2 \simeq 10^{-4}$ and sets the echo amplitude around $\frac{\Delta T}{T} \simeq 5 \cdot 10^{-6}$. This sensitivity is definitely achievable with a heterodyne detection scheme. In fact, signals of lower intensity (10^{-7}) have successfully been detected in our lab. In conclusion, considering the consistent improvement obtainable by reducing the laser repetition rate, future attempts to measure the echo should be pursued with a kHz amplifier.

CHAPTER VI

High-Frequency Diamagnetic Metamaterials

In the last few years, metamaterials have been an area of rapidly increasing interest. Beyond the attractive potential applications offered by these novel materials, the main motivation underlying the massive effort sustained by the scientific community can be attributed to the possibility of building left-handed (or negative refraction) materials [112, 113, 114]. One of the main difficulties hindering the achievement of negative refraction [115] lays in the weak magnetic response, even in the presence of a resonance, of natural materials especially at high frequencies [116]. To overcome this obstacle, several approaches have been proposed, one of the most famous being perhaps assemblies involving split rings [117]. Another popular method to achieve negative refraction [118] is to employ a matrix of resonators embedded in a host material: this artificial structure can exhibit both negative permittivity and permeability taking advantage of the well known Mie resonances [119, 120, 121]. Keeping in mind the aforementioned pioneering works, another aspect of magnetism will be examined here: diamagnetism, i.e., $\mu < 1$, μ being the magnetic permeability. This phenomenon is extremely weak in natural materials: the magnetic susceptibility, $\chi = \mu - 1$, of the majority of common materials does not exceed $\simeq -10^{-5}$ and reaches $\simeq -5 \cdot 10^{-4}$ only in pyrolytic graphite (see Table 6.1). Diamagnetism has certainly not received much attention in the scientific literature, but it is responsible for several remarkable phenomena: magnetic levitation is probably the most noteworthy [122, 123, 124].

The present chapter describes a novel metamaterial based on the well known sphere-in-a-host structure whose magnetic permeability can be selectively varied in the microwave frequency range up to a point where a strongly diamagnetic character ($\mu \simeq 0.4$) is achieved.

MATERIAL	χ (SI UNITS)
Water	-8.8×10^{-6}
Bismuth metal	-1.7×10^{-4}
Graphite rod	-1.6×10^{-4}
Pyrolitic graphite $\perp$ axis	-4.5×10^{-4}
Pyrolitic graphite $\parallel$ axis	-8.5×10^{-5}

Table 6.1: Magnetic susceptibility for different materials present in nature, from [4].

The first part of the chapter (Sec. 6.1) lays down the necessary mathematical tools to address a classic problem in physics: the scattering of electromagnetic radiation by a sphere (Sec. 6.2). The solution to the isolated sphere problem is then generalized in Sec. 6.3 to the case of multiple spheres arranged in a cubic lattice. The expression for the effective optical constants of a medium loaded with a matrix of such spheres is attained at the end of Sec. 6.3 and used in Sec. 6.4 to estimate the magnetic permeability of the new metamaterial. Sec. 6.5 is dedicated to outlining the fabrication procedure followed to build our samples, reporting the experimental data and discussing their relevance in light of the simulations previously carried out.

6.1 Expansion of a vector plane wave in spherical wave functions

The main difficulty that arises when dealing with the problem of a plane wave interacting with an object with spherical symmetry is to choose a convenient set of basis functions that provide the proper frame to solve Maxwell's equations and, particularly, to satisfy the required boundary conditions. In the case of a plane wave incident on a sphere, it turns out that the best choice are the *Spherical Wave Functions* $\mathbf{l}_{\substack{e\\o}}{}_{mn}$, $\mathbf{m}_{\substack{e\\o}}{}_{mn}$, $\mathbf{n}_{\substack{e\\o}}{}_{mn}$, defined as follows

[125]:

$$\mathbf{l}_{\substack{e\\mn\\o}} = \frac{\partial}{\partial R} z_n(kR) P_n^m(cos\theta) \begin{matrix} cos \\ sin \end{matrix} m\phi \, \mathbf{i}_1 + \frac{1}{R} z_n(kR) \frac{\partial}{\partial \theta} P_n^m(cos\theta) \begin{matrix} cos \\ sin \end{matrix} m\phi \, \mathbf{i}_2 \mp \frac{m}{Rsin\theta} z_n(kR) P_n^m(cos\theta) \begin{matrix} sin \\ cos \end{matrix} m\phi \, \mathbf{i}_3 \tag{6.1}$$

$$\mathbf{m}_{\substack{e\\mn\\o}} = \mp \frac{m}{sin\theta} z_n(kR) P_n^m(cos\theta) \begin{matrix} sin \\ cos \end{matrix} m\phi \, \mathbf{i}_2 - z_n(kR) \frac{\partial P_n^m}{\partial \theta} \begin{matrix} cos \\ sin \end{matrix} m\phi \, \mathbf{i}_3 \tag{6.2}$$

$$\mathbf{n}_{\substack{e\\mn\\o}} = \frac{n(n+1)}{kR} z_n(kR) P_n^m(cos\theta) \begin{matrix} cos \\ sin \end{matrix} m\phi \, \mathbf{i}_1 + \frac{1}{kR} \frac{\partial}{\partial R} [R z_n(kR)] \frac{\partial}{\partial \theta} P_n^m(cos\theta)] \begin{matrix} cos \\ sin \end{matrix} m\phi \, \mathbf{i}_2 \mp \frac{m}{kRsin\theta} \frac{\partial}{\partial R} [R z_n(kR)] P_n^m(cos\theta) \begin{matrix} sin \\ cos \end{matrix} m\phi \, \mathbf{i}_3 \tag{6.3}$$

where $\mathbf{i}_1$, $\mathbf{i}_2$ and $\mathbf{i}_3$ are the three unit vectors in the spherical coordinate system, $z_n(kR)$ represents one of the *Spherical Bessel functions* (j, n, $h^{(1)}$ or $h^{(2)}$), while P_n^m are the *Associated Legendre Polynomials* [126]. In order to take advantage of the benefits offered by the *Spherical Wave Functions*, it is necessary to expand a plane wave in terms of Eq. 6.1, Eq. 6.2 and Eq. 6.3. Let us thus consider a plane wave propagating in a medium with optical constants ϵ and μ, assuming that it is traveling along the z direction and that its electric field is polarized along $\mathbf{a}$:

$$\mathbf{E} = \mathbf{a} e^{ikz} = \mathbf{a} e^{ikRcos\theta} \tag{6.4}$$

where $k = \frac{2\pi}{\lambda}\sqrt{\epsilon\mu}$ is the magnitude of the wave vector, while θ is the angle between the radial vector $\mathbf{R}$ and the z axis. The vector $\mathbf{a}$ can be decomposed into its three Cartesian components:

$$\mathbf{a}_x = sin\theta cos\phi \, \mathbf{i}_1 + cos\theta cos\phi \, \mathbf{i}_2 - sin\phi \, \mathbf{i}_3 \tag{6.5a}$$

$$\mathbf{a}_y = sin\theta sin\phi \, \mathbf{i}_1 + cos\theta sin\phi \, \mathbf{i}_2 + cos\phi \, \mathbf{i}_3 \tag{6.5b}$$

$$\mathbf{a}_z = cos\theta \, \mathbf{i}_1 - sin\theta \, \mathbf{i}_2 \tag{6.5c}$$

Each of them can now be rewritten in terms of the *Spherical Wave Functions*. The mathematical procedure will be shown in detail only for $\mathbf{a}_x$; the result obtained will then be generalized to $\mathbf{a}_y$ and $\mathbf{a}_z$. Since $\nabla \cdot \mathbf{a}_x = 0$, only the zero divergence *Spherical Wave Func-*

tions, namely **m** and **n**, need to be included in the expansion. Moreover, given the $\mathbf{a}_x$ dependence on ϕ and the fact that the electric field does not diverge when $R \mapsto 0$, m has to be set to 1 and z_n has to be restricted to the *Spherical Bessel functions* of the first kind (j_n). The appropriate parity (e or o) for Eq. 6.2 and Eq. 6.3 can be chosen by keeping in mind the ϕ dependence of $\mathbf{a}_x$:

$$\mathbf{a}_x e^{ikz} = \mathbf{a}_x e^{ikRcos\theta} = \sum_{n=0}^{\infty} \left(a_n \mathbf{m}_{o1n}^{(1)} + b_n \mathbf{n}_{e1n}^{(1)} \right) \tag{6.6}$$

a_n can be found by first projecting Eq. 6.6 on the $\mathbf{m}_{o1n}^{(1)}$ vector space:

$$\int_0^{\pi} \int_0^{2\pi} \mathbf{a}_x \cdot \mathbf{m}_{o1n}^{(1)} e^{ikRcos\theta} sin\theta \, d\theta \, d\phi = 2\pi i^n n(n+1)[j_n(kR)]^2 \tag{6.7}$$

and then using the orthogonality properties of the *Spherical Bessel Functions* and the *Associated Legendre Polynomials*:

$$a_n \int_0^{2\pi} \int_0^{\pi} \mathbf{m}_{\substack{e \\ o}mn} \cdot \mathbf{m}_{\substack{e \\ o}mn} sin(\theta) \, d\theta \, d\phi = a_n(1+\delta) \frac{2\pi}{2n+1} \frac{(n+m)!}{(n-m)!} n(n+1)[z_n(kR)]^2 \tag{6.8}$$

where $\delta = 0$ if $m > 0$, $\delta = 1$ if $m = 0$. Equating Eq. 6.7 to Eq. 6.8 leads to:

$$a_n = i^n \frac{2n+1}{n(n+1)} \tag{6.9}$$

Since $\mathbf{n}_{e1n}$ shares the same orthogonality properties of $\mathbf{m}_{e1n}$, b_n can be promptly found:

$$b_n = -i^{n+1} \frac{2n+1}{n(n+1)} \tag{6.10}$$

Hence, $\mathbf{a}_x$ can be written as:

$$\mathbf{a}_x e^{ikz} = \sum_{n=0}^{\infty} i^n \frac{2n+1}{n(n+1)} \left(\mathbf{m}_{o1n}^{(1)} - i\mathbf{n}_{e1n}^{(1)} \right) \tag{6.11}$$

The y component of the $\mathbf{a}$ vector can be expanded in a similar way:

$$\mathbf{a}_y e^{ikz} = -\sum_{n=0}^{\infty} i^n \frac{2n+1}{n(n+1)} \left(\mathbf{m}_{e1n}^{(1)} + i\mathbf{n}_{o1n}^{(1)} \right) \tag{6.12}$$

The z component has to be treated somehow differently. Since $\mathbf{a}_z$ has a non-vanishing divergence, only the $\mathbf{l}$ function has to be included in its expansion. Repeating the same procedure outlined for $\mathbf{a}_x$ results in:

$$\mathbf{a}_z e^{ikz} = \frac{1}{k} \sum_{n=0}^{\infty} i^{n-1} (2n+1) \mathbf{l}_{e0n}^{(1)} \tag{6.13}$$

6.2 Diffracted field by a sphere

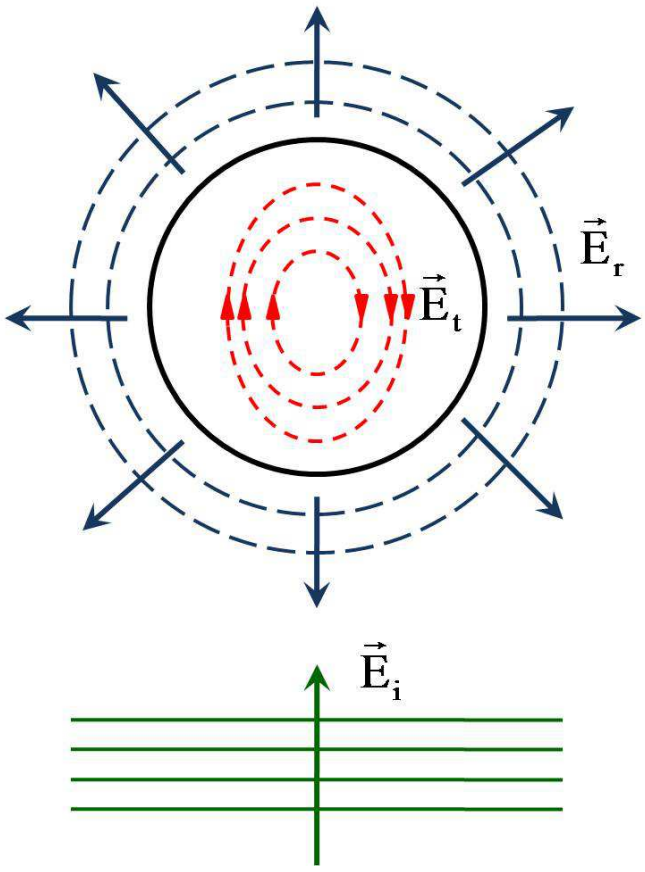

Figure 6.1: Plane wave incident on a dielectric sphere.

The spherical wave expansion so far developed can now be employed to solve the scattering-by-sphere problem [127, 128, 129]. If a sphere of radius a with dielectric constant

ϵ_2 and magnetic permeability μ_2 is located in a medium with constants ϵ_1 and μ_1, a plane wave propagating along the z direction and polarized along the x direction has a propagation vector given by $k_1 = \frac{2\pi}{\lambda}\sqrt{\epsilon_1\mu_1}$ in the medium and $k_2 = \frac{2\pi}{\lambda}\sqrt{\epsilon_2\mu_2}$ inside the sphere. The goal is now to calculate the electric and the magnetic field both inside and outside the sphere. The standard approach to this problem consists in splitting the electric field into three different parts (see Fig. 6.1): the incident plane wave $\mathbf{E}_i$; the field inside the sphere, $\mathbf{E}_t$; and the field that the sphere itself radiates due to the interaction with the incoming wave, $\mathbf{E}_r$. As pointed out at the beginning of the previous section, the boundary conditions are easily handled if $\mathbf{E}_i$, $\mathbf{E}_r$ and $\mathbf{E}_t$ are written in terms of vector spherical wave functions. The incident field has already been expanded in Eq. 6.11 and the result is restated here for convenience:

$$\begin{aligned}
\mathbf{E}_i &= \mathbf{a}_x E_0 e^{ik_1 z - i\omega t} = E_0 e^{-i\omega t} \sum_{n=1}^{\infty} i^n \frac{2n+1}{n(n+1)} \left(\mathbf{m}_{o1n}^{(1)} - i\mathbf{n}_{e1n}^{(1)} \right) \\
\mathbf{H}_i &= \mathbf{a}_y \tfrac{k_1}{\mu_1 \omega} E_0 e^{ik_1 z - i\omega t} = -\tfrac{k_1 E_0}{\mu_1 \omega} e^{-i\omega t} \sum_{n=1}^{\infty} i^n \frac{2n+1}{n(n+1)} \left(\mathbf{m}_{e1n}^{(1)} + i\mathbf{n}_{o1n}^{(1)} \right)
\end{aligned} \tag{6.14}$$

E_0 is the plane wave amplitude. The field inside the sphere and the "diffracted" one have the same functional form just with different coefficients a_n and b_n (see Eq. 6.6).

$$\begin{aligned}
\mathbf{E}_r &= E_0 e^{-i\omega t} \sum_{n=1}^{\infty} i^n \frac{2n+1}{n(n+1)} \left(a_n^r \, \mathbf{m}_{o1n}^{(3)} - i b_n^r \, \mathbf{n}_{e1n}^{(3)} \right) \\
\mathbf{H}_r &= -\tfrac{k_1 E_0}{\mu_1 \omega} e^{-i\omega t} \sum_{n=1}^{\infty} i^n \frac{2n+1}{n(n+1)} \left(b_n^r \, \mathbf{m}_{e1n}^{(3)} + i a_n^r \, \mathbf{n}_{o1n}^{(3)} \right)
\end{aligned} \tag{6.15}$$

$$\begin{aligned}
\mathbf{E}_t &= E_0 e^{-i\omega t} \sum_{n=1}^{\infty} i^n \frac{2n+1}{n(n+1)} \left(a_n^t \, \mathbf{m}_{o1n}^{(1)} - i b_n^t \, \mathbf{n}_{e1n}^{(1)} \right) \\
\mathbf{H}_t &= -\tfrac{k_2 E_0}{\mu_2 \omega} e^{-i\omega t} \sum_{n=1}^{\infty} i^n \frac{2n+1}{n(n+1)} \left(b_n^t \, \mathbf{m}_{e1n}^{(1)} + i a_n^t \, \mathbf{n}_{o1n}^{(1)} \right)
\end{aligned} \tag{6.16}$$

$\mathbf{m}$ and $\mathbf{n}$ in the incident and transmitted field contain spherical Bessel functions of the first

kind (j_n):

$$\mathbf{m}^{(1)}{}_{\substack{e\\o}}{}_{1n} = \pm\frac{1}{sin\theta}j_n(k_1R)P_n^1(cos\theta)\begin{matrix}sin\\cos\end{matrix}m\phi\,\mathbf{i}_2 - j_n(k_1R)\frac{\partial P_n^1}{\partial\theta}\begin{matrix}cos\\sin\end{matrix}m\phi\,\mathbf{i}_3 \tag{6.17}$$

$$\mathbf{n}^{(1)}{}_{\substack{e\\o}}{}_{1n} = \frac{n(n+1)}{k_1R}j_n(k_1R)P_n^1(cos\theta)\begin{matrix}cos\\sin\end{matrix}m\phi\,\mathbf{i}_1 + \frac{1}{k_1R}[k_1Rj_n(k_1R)]' \tag{6.18}$$
$$\frac{\partial}{\partial\theta}P_n^1(cos\theta)\begin{matrix}cos\\sin\end{matrix}m\phi\,\mathbf{i}_2 \pm \frac{1}{k_1Rsin\theta}[k_1Rj_n(k_1R)]'P_n^1(cos\theta)\begin{matrix}sin\\cos\end{matrix}m\phi\,\mathbf{i}_3$$

In Eq. 6.16 k_2 replaces k_1, while in $\mathbf{m}^{(3)}$ and $\mathbf{n}^{(3)}$, $h_n^{(1)}$ (the spherical Hankel function of the first kind) takes the place of j_n. In order to find the value of a_n and b_n, the continuity of the tangential component of the electric and magnetic field has to be enforced:

$$\begin{aligned}\mathbf{i}_1\times(\mathbf{E}_i+\mathbf{E}_r)&=\mathbf{i}_1\times\mathbf{E}_t\\ \mathbf{i}_1\times(\mathbf{H}_i+\mathbf{H}_r)&=\mathbf{i}_1\times\mathbf{H}_t\end{aligned} \tag{6.19}$$

These two vector equations generate a system of four scalar equations that can be solved to find the unknown coefficients a_n and b_n. Only a_n^r and b_n^r are needed to find the field outside the sphere ($\mathbf{E}_r$) and they are given by:

$$a_n^r = -\frac{\mu_2 j_n(N\rho)[\rho j_n(\rho)]' - \mu_1 j_n(\rho)[N\rho j_n(N\rho)]'}{\mu_2 j_n(N\rho)[\rho h_n^{(1)}(\rho)]' - \mu_1 h_n^{(1)}(\rho)[N\rho j_n(N\rho)]'} \tag{6.20}$$

$$b_n^r = -\frac{\mu_2 j_n(\rho)[N\rho j_n(N\rho)]' - \mu_1 N^2 j_n(N\rho)[\rho j_n(\rho)]'}{\mu_2 h_n^{(1)}(\rho)[N\rho j_n(N\rho)]' - \mu_1 N^2 j_n(N\rho)[\rho h_n^{(1)}(\rho)]'} \tag{6.21}$$

where two new variables have been introduced: $\rho = k_1 a$ and $N = \frac{k_2}{k_1}$.

6.3 Scattering by a material loaded with spherical particles

The mathematical framework defined in the previous section can be now adopted to address a more involved problem: a plane wave incident on a material loaded with a matrix of spherical particles (see Fig. 6.2). The negative semi space ($z < 0$) contains a medium with permittivity ϵ_1 and permeability μ_1, so that a plane wave propagating through is denoted

by the following electric and magnetic field:

$$\begin{aligned} E_{xi} &= E_{0i}e^{-ikz\sqrt{\epsilon_1\mu_1}} \\ H_{yi} &= H_{0i}e^{-ikz\sqrt{\epsilon_1\mu_1}} = -\sqrt{\frac{\epsilon_1}{\mu_1}}E_{0i}e^{-ikz\sqrt{\epsilon_1\mu_1}} \end{aligned} \tag{6.22}$$

where, as usual, k is the magnitude of the propagating vector. The same medium is filled in the positive half space ($z > 0$) by spherical particles of radius a, with permittivity ϵ_2, permeability μ_2, spaced from each other by a length s.

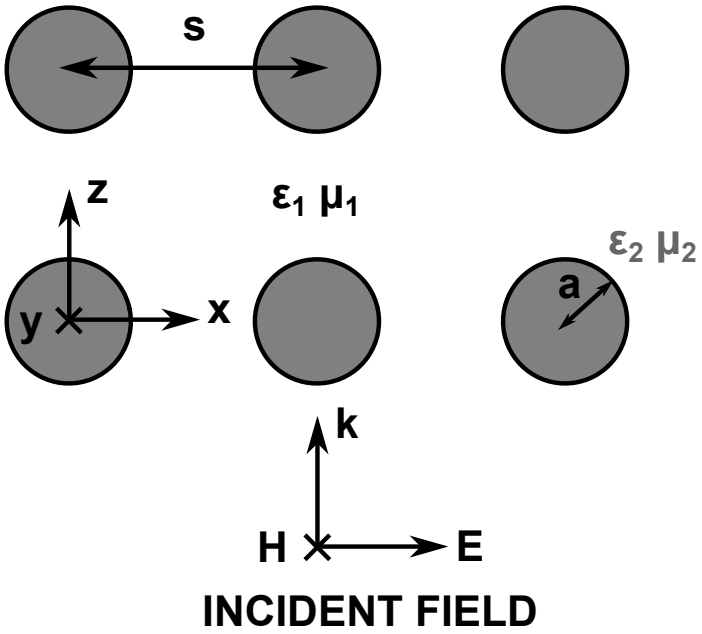

Figure 6.2: Electromagnetic wave incident on a medium loaded with a matrix of spherical particles.

Assigning to the sphere matrix effective optical constants ϵ and μ is equivalent to saying that the reflected and transmitted fields are related to the incident field by the reflection (r) and transmission (t) coefficients [26]:

$$r = \frac{E_r}{E_i} = \frac{\sqrt{\frac{\mu}{\epsilon}} - \sqrt{\frac{\mu_1}{\epsilon_1}}}{\sqrt{\frac{\mu}{\epsilon}} + \sqrt{\frac{\mu_1}{\epsilon_1}}} \qquad\qquad t = \frac{E_t}{E_i} = 1 + r \tag{6.23}$$

The reflected field is:

$$\begin{aligned} E_{xr} &= rE_{0i}e^{-ikz\sqrt{\epsilon_1\mu_1}} \\ H_{yr} &= r\sqrt{\frac{\epsilon_1}{\mu_1}}E_{0i}e^{-ikz\sqrt{\epsilon_1\mu_1}} \end{aligned} \tag{6.24}$$

while the transmitted field is:

$$\begin{aligned} E_{xt} &= tE_{0i}e^{-ikz\sqrt{\epsilon\mu}} \\ H_{yt} &= -t\sqrt{\frac{\epsilon}{\mu}}E_{0i}e^{-ikz\sqrt{\epsilon\mu}} \end{aligned} \tag{6.25}$$

6.3.1 Scattered field by a sphere in the small wavelength approximation

The rather cumbersome problem defined above can be considerably simplified by considering spheres with a radius much smaller than the incident plane wave wavelength. When $a << \frac{\lambda}{\sqrt{\epsilon_1\mu_1}}$ (or, equivalently, $\rho << 1$), all $n > 1$ terms in the Eq. 6.15 summation can be neglected and the coefficients a_1^r and b_1^r can be recast in a new form:

$$\begin{aligned} a_1 = &\quad i\frac{2}{3}(k^2\mu_1\epsilon_1)^{\frac{3}{2}}a^3\frac{\mu_1-\mu_p}{2\mu_1+\mu_p} \\ b_1 = &\quad i\frac{2}{3}(k^2\mu_1\epsilon_1)^{\frac{3}{2}}a^3\frac{\epsilon_1-\epsilon_p}{2\epsilon_1+\epsilon_p} \end{aligned} \tag{6.26}$$

ϵ_p and μ_p are defined as follows:

$$\frac{\epsilon_p}{\epsilon_2} = \frac{\mu_p}{\mu_2} = \frac{2(sin\theta - \theta cos\theta)}{(\theta^2-1)sin\theta + \theta cos\theta} \tag{6.27}$$

and $\theta = ka\sqrt{\epsilon_2\mu_2}$. Eq. 6.26 can be obtained from Eq. 6.20 and Eq. 6.21 recalling the following approximations for small arguments of the Bessel functions [126]:

$$\begin{aligned} j_1(\rho) &\sim \frac{1}{3}\rho & [N\rho j_1(N\rho)]' &\sim \frac{1}{3}\rho \\ h_1^{(1)}(\rho) &\sim \frac{i}{\rho^2} & [\rho h_1^{(1)}(\rho)]' &\sim \frac{i}{\rho^2} \end{aligned} \tag{6.28}$$

The x component of the electric field generated by a single sphere located at (x_0, y_0, z_0) can be now computed from Eq. 6.15:

$$E_{xr} = a^3\left[E(z_0)\frac{\epsilon_p-\epsilon_1}{\epsilon_p+2\epsilon_1}(\frac{\partial^2}{\partial x^2}+k^2\mu_1\epsilon_1) - ik\mu_1 H(z_0)\frac{\mu_p-\mu_1}{\mu_p+2\mu_1}\frac{\partial}{\partial z}\right]\frac{e^{-ikr_0\sqrt{\epsilon_1\mu_1}}}{r_0} \tag{6.29}$$

r_0 indicates the distance between the particle and the point at which the field is investigated. A similar approach leads to the corresponding equation for the magnetic field polarized along

the y axis:

$$H_{yr} = a^3 \left[H(z_0) \frac{\mu_p - \mu_1}{\mu_p + 2\mu_1} (\frac{\partial^2}{\partial y^2} + k^2 \mu_1 \epsilon_1) - ik\mu_1 E(z_0) \frac{\epsilon_p - \epsilon_1}{\epsilon_p + 2\epsilon_1} \frac{\partial}{\partial z} \right] \frac{e^{-ikr_0\sqrt{\epsilon_1\mu_1}}}{r_0} \tag{6.30}$$

6.3.2 Scattering by an array of spherical particles

The total scattered field includes the contributions from all the other spheres located at $R_i = ls\mathbf{a}_x + ms\mathbf{a}_y + ns\mathbf{a}_z$ where l, m, n are three integer indexes. The field at (x_0, y_0, z_0) is given by:

$$\begin{aligned} E(z_0) = E_i e^{-ikz_0\sqrt{\epsilon_1\mu_1}} + \sum_{l'=-\infty}^{+\infty} \sum_{m'=-\infty}^{+\infty} \sum_{n'=0}^{+\infty} a^3 \\ \left[E(ns) \frac{\epsilon_p - \epsilon_1}{\epsilon_p + 2\epsilon_1} (\frac{\partial^2}{\partial x_0^2} + k^2 \epsilon_1 \mu_1) - jk\mu_1 H(ns) \frac{\mu_p - \mu_1}{\mu_p + 2\mu_1} \frac{\partial}{\partial z_0} \right] \frac{e^{-ikR_0\sqrt{\epsilon_1\mu_1}}}{R_0} \end{aligned} \tag{6.31}$$

l', m', n' are used to indicate that the 0 term has to be omitted from the summation, while $R_0 = \sqrt{(ls - x_0)^2 + (ms - y_0)^2 + (ns - z_0)^2}$ is the distance of the i^{th} sphere from (x_0, y_0, z_0). Defining $\alpha = ls$, $\beta = ms$ and $\gamma = ns$, the sum can be replaced by the following integral:

$$\begin{aligned} \frac{1}{s^3} \int_{-\infty}^{+\infty} \int_{-\infty}^{+\infty} \int_{0}^{+\infty} - \int_{x_0-\frac{s}{2}}^{x_0+\frac{s}{2}} \int_{y_0-\frac{s}{2}}^{y_0+\frac{s}{2}} \int_{z_0-\frac{s}{2}}^{z_0+\frac{s}{2}} d\alpha\, d\beta\, d\gamma \\ \left[E(\gamma) \frac{\epsilon_p - \epsilon_1}{\epsilon_p + 2\epsilon_1} (\frac{\partial^2}{\partial x_0^2} + k^2 \epsilon_1 \mu_1) - jk\mu_1 H(\gamma) \frac{\mu_p - \mu_1}{\mu_p + 2\mu_1} \frac{\partial}{\partial z_0} \right] \frac{e^{-ik\sqrt{\epsilon_1\mu_1}\sqrt{(\alpha-x_0)^2+(\beta-y_0)^2+(\gamma-z_0)^2}}}{\sqrt{(\alpha - x_0)^2 + (\beta - y_0)^2 + (\gamma - z_0)^2}} \end{aligned} \tag{6.32}$$

When dealing with the integration around the (x_0, y_0, z_0) sphere, only the highest $\frac{1}{R_0}$ power, which arises from the $\frac{\partial^2}{\partial x_0^2}$ term, has to be retained:

$$\frac{\partial^2}{\partial x_0^2} [\frac{e^{-ikR\sqrt{\epsilon_1\mu_1}}}{R_0}] \sim \frac{3(\alpha - x_0)^2 - R_0^2}{R_0^5} \tag{6.33}$$

The integral of Eq. 6.33 is easily computable by substitution:

$$\int_{x_0-\frac{s}{2}}^{x_0+\frac{s}{2}} \int_{y_0-\frac{s}{2}}^{y_0+\frac{s}{2}} \int_{z_0-\frac{s}{2}}^{z_0+\frac{s}{2}} \frac{3(\alpha - x_0)^2 - R_0^2}{R_0^5} d\alpha\, d\beta\, d\gamma = -\frac{4}{3}\pi \tag{6.34}$$

The first integral in Eq. 6.32 can be carried out more easily addressing first the dα and dβ part and switching to cylindrical coordinates:

$$\int_{-\infty}^{+\infty}\int_{-\infty}^{+\infty} \frac{e^{-ikR\sqrt{\epsilon_1\mu_1}}}{R_0} d\alpha\, d\beta = \frac{-2\pi i}{k\sqrt{\epsilon_1\mu_1}} e^{-ik|\gamma - z_0|\sqrt{\epsilon_1\mu_1}} \tag{6.35}$$

The integration in dγ can be performed more straightforwardly after setting $\frac{\partial}{\partial z_0} = -\frac{\partial}{\partial \gamma}$, the substitution is allowed since the integrand is a function of $\gamma - z_0$. This finally leads to the expression for the electric field:

$$\begin{aligned} E(z_0) &= E_i e^{-ikz_0\sqrt{\epsilon_1\mu_1}} + \frac{4}{3}\frac{\pi a^3}{s^3} E(z_0) \frac{\epsilon_p - \epsilon_1}{\epsilon_p + 2\epsilon_1} \\ &- \frac{2\pi i}{k\sqrt{\epsilon_1\mu_1}} \frac{a^3}{s^3} \int_0^{+\infty} \left[k^2 \epsilon_1 \mu_1 E(\gamma) \frac{\epsilon_p - \epsilon_1}{\epsilon_p + 2\epsilon_1} + ik\mu_1 H(\gamma) \frac{\mu_p - \mu_1}{\mu_p + 2\mu_1} \frac{\partial}{\partial \gamma} \right] e^{-ik|\gamma - z_0|\sqrt{\epsilon_1\mu_1}} d\gamma \end{aligned} \tag{6.36}$$

6.3.3 Effective electrical constants

To conclude the analysis, it is necessary to compute explicitly the electric and magnetic field in the medium filled by spheres and infer from their expression the value of the effective optical constants. By applying the operator $\triangle = \frac{\partial^2}{\partial z^2} + k^2\epsilon_1\mu_1$ to both Eq. 6.36 and the corresponding equation for the magnetic field, the following system of two differential equations is obtained:

$$\begin{aligned} \triangle E(z_0)(Q - f) &= -3k^2\epsilon_1\mu_1 f \left[E(z_0) + \frac{1}{ik\epsilon_1} \frac{Q}{R} \frac{\partial}{\partial z_0} H(z_0) \right] \\ \triangle H(z_0)(R - f) &= -3k^2\epsilon_1\mu_1 f \left[H(z_0) + \frac{1}{ik\epsilon_1} \frac{R}{Q} \frac{\partial}{\partial z_0} E(z_0) \right] \end{aligned} \tag{6.37}$$

where

$$Q = \frac{\epsilon_p + 2\epsilon_1}{\epsilon_p - \epsilon_1} \qquad R = \frac{\mu_p + 2\mu_1}{\mu_p - \mu_1} \tag{6.38}$$

and $f = \frac{4}{3}\pi a^3/s^3$ is the filling factor, i.e. the ratio between the volume filled by the spheres and the volume filled by the hosting material. The system in Eq. 6.37 can be solved postulating the following functional form of the solution:

$$E(z_0) = Ae^{-iKz_0} \qquad H(z_0) = Be^{-iKz_0} \tag{6.39}$$

Some tedious algebraic manipulation leads eventually to the propagation constant K and the reflected electric field E_r:

$$K = k^2\epsilon_1\mu_1\frac{(Q+2f)(R+2f)}{(Q-f)(R-f)} \tag{6.40}$$

$$E_{xr} = E_i e^{ikz\sqrt{\epsilon_1\mu_1}}\frac{\sqrt{\frac{Q-f}{Q+2f}\frac{R+2f}{R-f}}-1}{\sqrt{\frac{Q-f}{Q+2f}\frac{R+2f}{R-f}}+1} \tag{6.41}$$

The effective dielectric and magnetic constant are found by setting $K = k^2\epsilon\mu$ and comparing Eq. 6.41 with Eq. 6.23:

$$\epsilon = \epsilon_1\left(1+\frac{3f}{\frac{\epsilon_p+2\epsilon_1}{\epsilon_p-\epsilon_1}-f}\right) \tag{6.42}$$

and

$$\mu = \mu_1\left(1+\frac{3f}{\frac{\mu_p+2\mu_1}{\mu_p-\mu_1}-f}\right) \tag{6.43}$$

6.3.4 Approximation for metal spheres

Even though Eq. 6.42 and Eq. 6.43 are exact and perfectly general, they are quite involved and tend to hide the dependence of the optical constants on the different parameters involved. The physical picture can be greatly simplified limiting our analysis to metal spherical inclusions. In this case the dielectric constant, in accordance with the Drude model [63], is large and almost purely imaginary at low frequencies, while the magnetic constant is approximately equal to one. If $\epsilon_2 = -i\alpha$ with $\alpha >> 1$, $F(\theta) \sim \frac{2}{i\theta}$, ϵ_p and μ_p are reduced to:

$$\epsilon_p = \frac{2}{i}\sqrt{\frac{\epsilon_2}{\mu_2}}\frac{\lambda}{2\pi a} \qquad\qquad \mu_p = \frac{2}{i}\sqrt{\frac{\mu_2}{\epsilon_2}}\frac{\lambda}{2\pi a} \tag{6.44}$$

Since ϵ_p is now smaller than ϵ_2 but still significantly larger than ϵ_1, Eq. 6.42 becomes:

$$\epsilon = \epsilon_1\left(1+\frac{3f}{1-f}\right) \tag{6.45}$$

On the other hand, a quick glance at Eq. 6.44 reveals that $\mu_p << \mu_1$, as a result Eq. 6.43 becomes:

$$\mu = \mu_1\left(1-\frac{3f}{2+f}\right) \tag{6.46}$$

Eq. 6.45 and Eq. 6.46 clearly show that, in the particular case of metal spheres, the effective permeability of the composite depends only on the filling factor (f) and the permeability (μ_1) of the host medium. This can be more intuitively understood by noticing that the condition $|\theta| >> 1$ can be also expressed, after some manipulations, as $\delta << a$. $\delta = \sqrt{\frac{2}{\sigma\omega\mu_0}}$ is the skin depth of the metal particles and accounts for the ability of a material to repel an AC electric field. If the electromagnetic field barely penetrates the spheres ($\delta << a$) and propagates only through the background matrix, the effective permeability will be dependent only on the ratio of the volume filled by the metal spheres and the host material.

6.4 Simulations

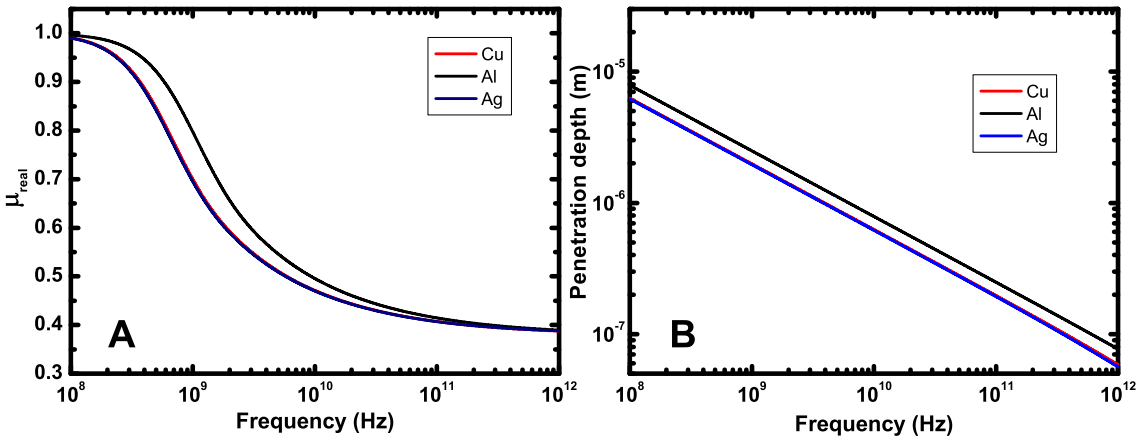

Figure 6.3: (A): Simulated real part of the magnetic permeability of a non magnetic medium loaded with 5μ spherical inclusions made out of copper, silver and aluminum. (B): penetration depth for copper, silver and aluminum.

As pointed out in the introduction, diamagnetism ($\mu < 1$) is a recurrent but rather weak phenomenon in nature, and it is thus important to estimate beforehand how far the permeability of a material loaded with spheres deviates from the $\mu \sim 1$ case. The optical constants of perfect spherical particles made up of three different metals (silver, aluminum and copper) embedded in a medium with $\epsilon = 2.25$ and $\mu = 1$ were theoretically investigated. Since only frequencies much lower than the metal plasma frequency were simulated, the metal spheres permittivity was estimated using the Drude model [63]. Fig. 6.3 shows the real part of μ for spheres having a radius a = 5μm and spacing s = 10μm. It is encouraging to note that around 10GHz both silver and copper spheres exhibit a permeability as low as

$\simeq 0.5$ corresponding to $\chi \simeq -0.5$, much higher in magnitude than any of the values listed in Table 6.1. The two main assumptions of our model ($a >> \frac{\lambda}{\sqrt{\epsilon_1 \mu_1}}$ and $\delta << a$) will be verified later on for the particular choice of parameters (a, s, λ) adopted in the experiments.

6.5 Experiments

Several experiments were carried out to extract the magnetic permeability of different samples mimicking the previously discussed sphere-in-a-host model. The experiments were conceived to achieve two goals: demonstrate the possibility of obtaining pronounced diamagnetic properties, at least in a narrow frequency range; and identify a specific trend in the permeability of our samples when a particular parameter, the sphere diameter in our case, is varied.

6.5.1 Sample preparation

Figure 6.4: 10μm copper sphere sample.

All samples were made up of copper spheres because copper demonstrates a lower permeability in the microwave range, see Fig. 6.3, and it is not excessively expensive. The copper spherical particles (99% purity) were purchased from *Sigma-Aldrich* in three different sizes: 10μm, 75μm and 475μm, see Fig. 6.5. The penetration depth of copper at 10GHz is $\simeq$ 500nm as can be inferred from Fig. 6.3 and, thus, it is much smaller than the sphere radius in all three cases. L-Menthol ($C_{10}H_{20}O$) bought from *Alpha Aesar* was used as a

host material for the spherical inclusions. Menthol, as opposed to other binding materials, exhibits all the required properties for this specific application: it is transparent in the microwave frequency range; it is not magnetic; and it is very easy to manipulate given its low melting point ($43° - 45°$C). In addition, the effective medium approximation ($a << \frac{\lambda}{\sqrt{\epsilon_1 \mu_1}}$) is valid at 10GHz. In fact, since menthol's refractive index is $\simeq 1.5$ in the microwave range, λ at this frequency is $\simeq$ 2cm.

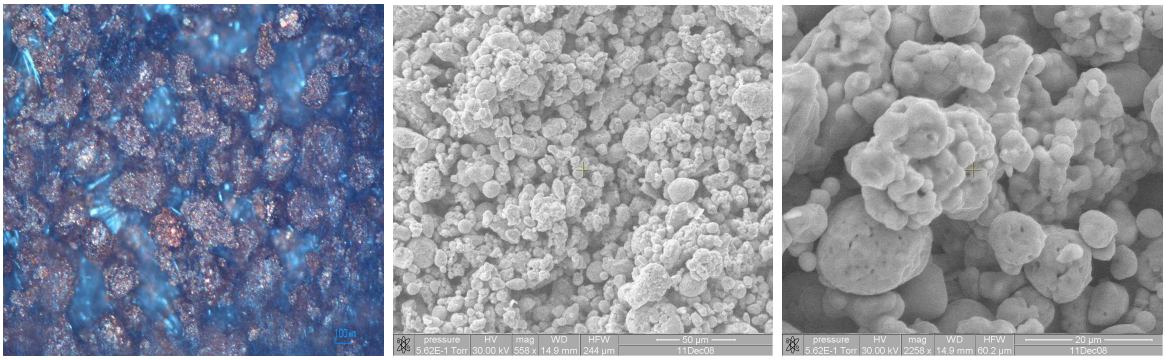

Figure 6.5: From left to right: optical microscope image of a 425μm sphere sample, SEM picture of a 10μm sphere sample with two different magnifications.

All the samples studied in this work were prepared following the same procedure. The menthol crystals were first melted in an oven at 100°C and then mixed with the copper powder keeping a mass ratio of approximately 1 : 5. The composite was left in the oven and stirred repetitively until it became a uniform mixture. The mixture was then poured into an aluminum mold, left at 100°C for about 10 minutes to facilitate the particles' settling, then cooled down at room temperature until it completely solidified. To prevent the sample from sticking to the mold and cracking once it was opened, the mold walls were coated with a release agent before being in contact with the mixture. The samples were roughly 20cm × 21cm × 0.74cm size (Fig 6.4) and presented a surface roughness of less than 500μm.

6.5.2 Experimental setup

The electrical constants were extracted using a *Gaussian Beam Telescope* (see Fig. 6.6), [130, 131]. The setup is composed of four lenses mounted on a rail and two antenna horns manufactured by *Dorado*. The lenses, made out of Teflon (almost transparent in the microwave), were moved relative to each other with mm accuracy by a mechanical driver controlled remotely and were able to focus the beam down to a $\simeq$ 10cm waist spot. The

setup was designed in such a way that the frequency dependent beam waist location varied over a range much smaller than the Rayleigh range [132].

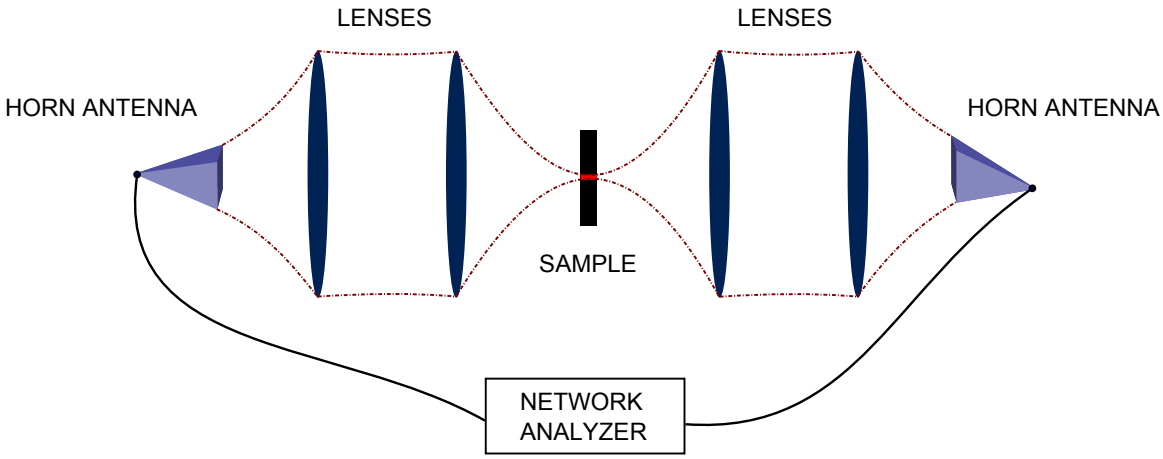

Figure 6.6: Gaussian Beam Telescope setup.

The large sample surface area (20cm $\times$ 21cm) prevented the beam from being clipped and ensured that the incident power was entirely confined within the sample. As has been amply discussed by several authors [133], it is crucial to avoid *Fabry-Perot* resonances to be able to extract meaningful optical parameters. If d is the sample thickness, the *Fabry-Perot* resonances occur at frequency multiples of $c/2nd$ [26], where c is the speed of light in vacuum and n the refractive index of the sample. Given the sample thickness, $d \simeq 7.4$mm, and the effective refractive index of our medium, $n \simeq 2.8 - 3$, the Fabry-Perot resonances are thus safely confined to the edges of the explored frequency range and do not affect significantly our measurements; see Fig. 6.7. The data was acquired via an Agilent Network Analyzer connected to the two horns. Driving one of the two horns, the Network Analyzer launches a sinusoidal signal (7GHz $\div$ 12GHz) toward the sample and collects the fraction of it that is reflected (back to the same horn) and transmitted (to the horn on the other side of the rail). Since both sides of the sample are tested, each measurement provides four variables, commonly known as scattering parameters: S_{11}, S_{12}, S_{21} and S_{22} [134]. To better understand their physical significance the experiment can be modeled using the transmission line formalism, see Fig. 6.8. A material with unknown ϵ_2 and μ_2 is fully characterized by its wave impedance $Z_2 = \sqrt{\frac{\mu_2}{\epsilon_2}}$ and propagation constant $k_2 = \omega\sqrt{\epsilon_2\mu_2}$. When a voltage wave propagating through the medium surrounding the unknown material hits the sample, part

of it is reflected and part transmitted; hence two parameters can be defined: $S_{11} = \frac{V_{refl}}{V_{inc}}$ and $S_{12} = \frac{V_{trans}}{V_{inc}}$.

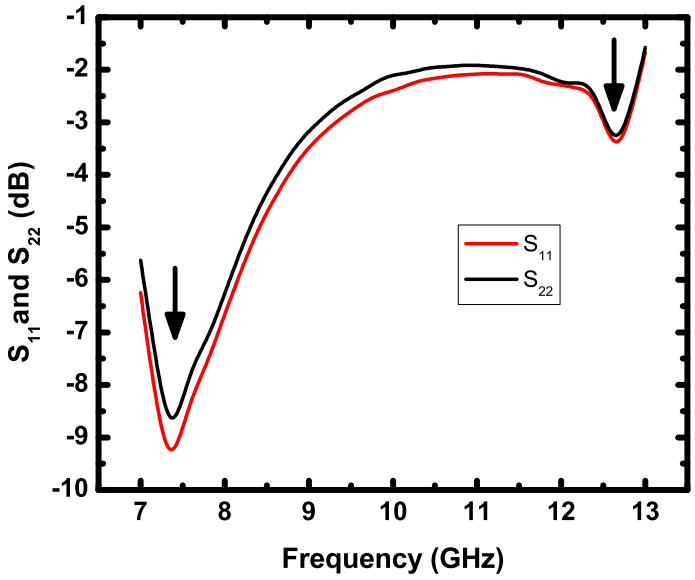

Figure 6.7: Amplitude of the scattering parameters, S_{11} and S_{22}, in the 10μm spheres sample. Two Fabry-Perot resonances are visible at the edges of the explored frequency interval.

S_{21} and S_{22} are the analogues of S_{11} and S_{12} when the incoming wave propagates in the direction opposite to the one indicated in Fig. 6.8. Following a standard network analysis approach, it can be shown that [134]:

$$\begin{aligned} \cos(kd) &= \frac{1 - S_{11}^2 + S_{21}^2}{2S_{21}} \\ Z &= Z_0 \sqrt{\frac{(1+S_{11})^2 - S_{21}^2}{(1-S_{11})^2 - S_{21}^2}} \end{aligned} \tag{6.47}$$

where $Z_0 = 376.73\Omega$ is the free space impedance. k_2 and Z_2 can be found by using the definition of wave impedance and propagation constant:

$$\begin{aligned} k_2 Z_2 &= \omega\sqrt{\epsilon_2\mu_2}\sqrt{\frac{\mu_2}{\epsilon_2}} = \omega\mu_2 \\ \frac{k_2}{Z_2} &= \omega\sqrt{\epsilon_2\mu_2}\sqrt{\frac{\epsilon_2}{\mu_2}} = \omega\epsilon_2 \end{aligned} \tag{6.48}$$

Eq. 6.47 and Eq. 6.48 highlight the connection between the unknown optical constants (ϵ_2

and μ_2) and the scattering parameters provided by the Network Analyzer and have been used to extract the effective parameters of our samples.

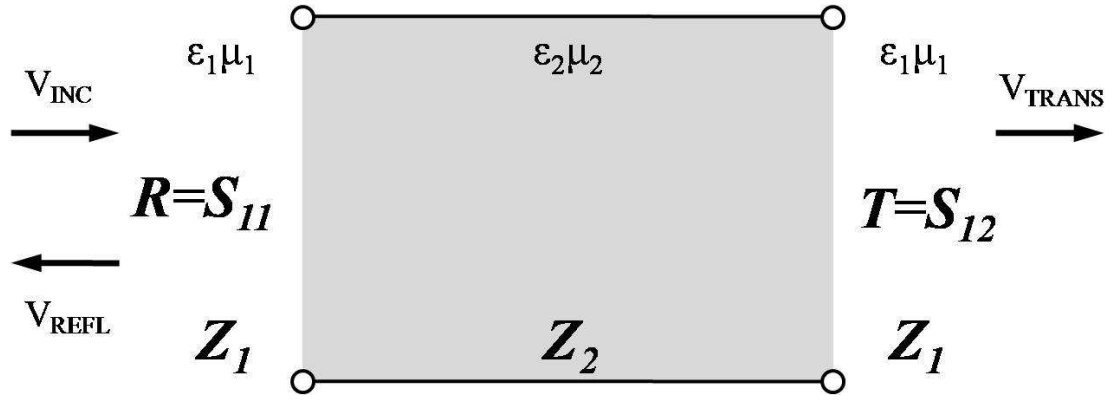

Figure 6.8: Transmission line and scattering parameters.

6.5.3 Experimental results and comparison with the theory

Experimental measurements were taken on three samples differing from each other only by the size of the spherical inclusions, see Fig. 6.5. Before measuring the sample, a perfectly conducting plate and a $\lambda/2$ transmission line were tested to properly calibrate the setup. Fig. 6.9 shows a comparison between experimental data and simulation results. In the simulations, the filling factor was set to $\frac{\pi}{6}$ (close packing) and the host material was assumed to have $\epsilon \simeq 2.5$ and $\mu \simeq 1$ for all the frequencies considered. Two observations are necessary at this point: as anticipated, a very low permeability ($\simeq 0.5$) was achieved; the spheroid size strongly affected the value of μ, specifically, a larger size corresponded to a lower permeability. This last remark is in perfect accordance with the simulations and reflects the μ dependence on θ already illustrated in Eq. 6.43: a larger radius produces a bigger values of θ and, consequently, a lower μ (see the discussion in Sec. 6.3.4). However, a pronounced discrepancy between the simulated and measured permeability is clearly noticeable, especially for the samples containing the smallest spheres. The mismatch between simulations and experimental data can be accounted for by considering that the actual size of the particles was, on average, smaller than the nominal one (see Fig.6.5) and that the density of copper particles in our sample was, in general, smaller than the simulated one. This explains why the measured permeability is higher than expected especially in the sam-

ples made up of smaller particles ($10\mu m$ and $75\mu m$): lighter particles require a longer time than heavier ones to deposit and to arrange in a dense matrix. Another factor that cannot be ignored is that, as evident in Fig. 6.5, the particles making up the samples were not perfectly spherical and, consequently, the theoretical predictions apply only marginally.

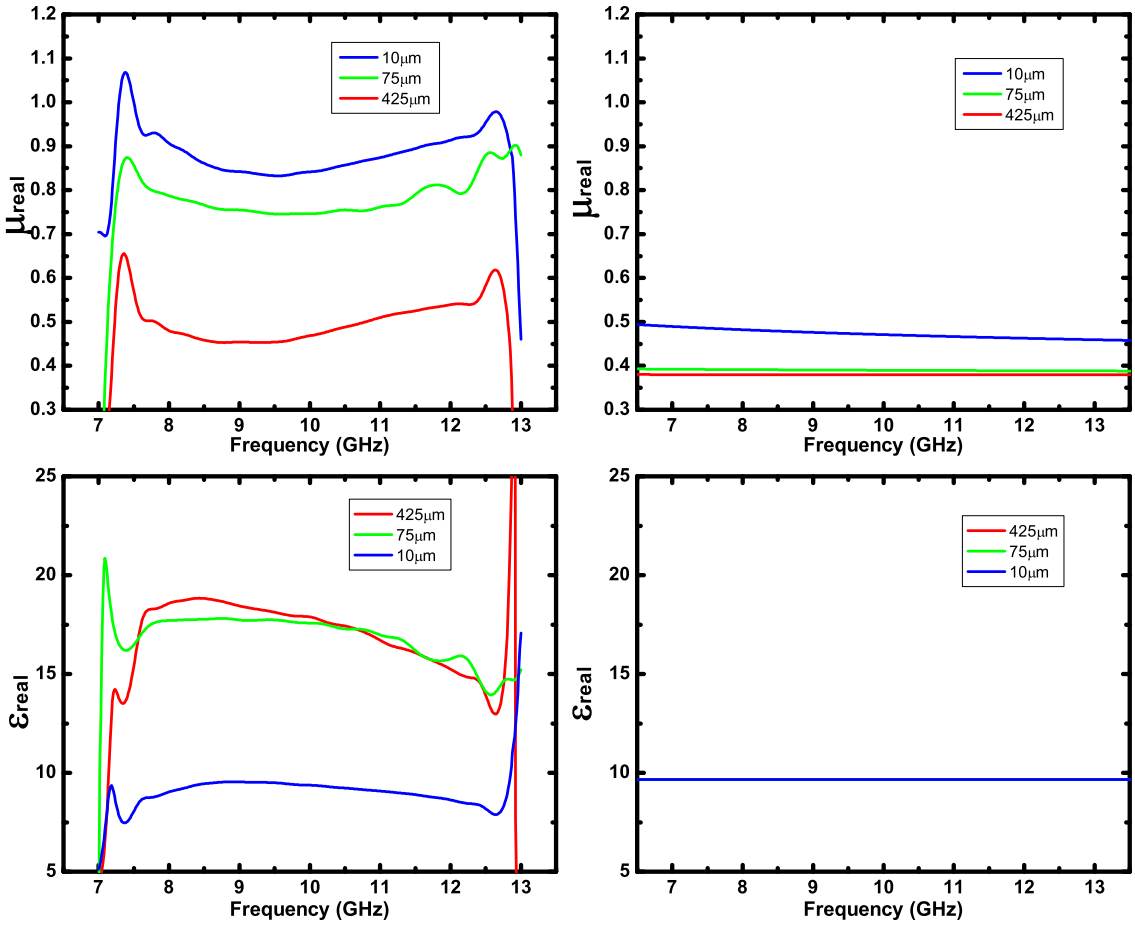

Figure 6.9: Measured (left) and simulated (right) permeability and permittivity for the 10μm, 75μm, 425μm diameter samples.

CHAPTER VII

Conclusions and Future Work

In Chap. IV the interaction of light with vibrational modes was investigated by spontaneous Raman and ISRS experiments carried out in three different semiconductors. The measurements performed on GaAs helped to clarify a highly controversial topic: the excitation of coherent longitudinal phonons. The seemingly contradictory outcomes of different experiments, conducted both in this dissertation and elsewhere [42, 43, 73, 74], were explained by an analysis of the various generation mechanisms of coherent phonons. The better understanding of ISRS in GaAs paves the way for a particularly attractive opportunity. GaAs undoubtedly constitutes an extremely good candidate to validate the two Raman tensors theory and, especially, some of its recent expansions [3]. As opposed to other materials, in (111) GaAs the deformation potential of two substantially different modes (a longitudinal and a transverse one) can be compared. In order to excite two distinct frequencies in ISRS experiments, it will be necessary to prevent the photoinjected carriers from driving the plasmon mode toward its asymptotic frequency, ω_{TO}. This can be accomplished, for instance, by employing a Ti:Sapphire oscillator rather than an amplifier.

The experiments on GaSe highlighted the impact of a polariton mode both on spontaneous Raman and pump probe measurements. The complications introduced by the presence of a spatially non uniform field were discussed especially in regard to the accuracy of the Raman tensor extraction process. The analysis on the temperature dependence of the $A_1^{'}$ and $E^{'}$ deformation potentials can be completed provided that the intensity of the $E^{'}$ field is fully recovered. A spatially resolved ISRS experiment [94] would probably be the most effective approach to achieve this goal.

Raman scattering turned out to be a valuable tool to detect surface plasmons in CdSe. Even though the collected data already provided sufficient evidence of the existence of surface modes, it would be interesting to examine the polariton frequency dependence on the surface wavevector ($\mathbf{k}_{\|}$). This can be accomplished by controlling the laser incident angle on the CdSe crystal as previously shown in some well known studies on GaN [67].

In Chap. V the focus is changed from coherent phonons to squeezed phonon states. Both a classical and quantum mechanical description of double pump experiments led to the discovery of a new phenomenon, named phonon "echo". Even though the echo signal could not be measured experimentally, several suggestions are presented at the end of the chapter to guide future attempts in this direction. Recent studies on $KTaO_3$ [111, 135, 136] indicate that a kHz amplifier is the proper tool to bring the weak echo signal intensity withing the detectable range.

In Chap. VI a high frequency diamagnetic metamaterial is discussed within the framework of Lewin's model [5]. The experimentally extracted optical constants appeared to match to a good extent with the theoretical predictions. The great potential of this novel material could be fully displayed in a levitation experiment [4]. Due to the high value of the magnetic susceptibility ($\chi = -0.5$, SI units), the magnetic field intensity required to lift this composite would be significantly lower than for any other natural material. In pursuing this attempt, special attention should be paid to estimate beforehand the intensity of the Eddy currents induced in the metal inclusions. The heat generated by Joule's effect could easily melt the menthol and, at very high current density, the copper spheres as well.

BIBLIOGRAPHY

BIBLIOGRAPHY

[1] Kuznetsov A.V. and Stanton C.J. Thery of Choerent Phonon Oscillations in Semiconductors. *Phys. Rev. Lett.*, 73(24):3243, December 1994.

[2] Stevens T.E., Khul J., and Merlin R. Coherent Phonon Generation and the Two Stimulated Raman Tensors. *Phys. Rev. B*, 65:144304, March 2002.

[3] Li J., Chen J., Fahy S., Reis D.A., and Merlin R. To be published.

[4] Simon M.D. and Geim A.K. Diamagnetic levitation: Flying frogs and floating magnets. *J. Appl. Phys.*, 87(9):6200, May 2000.

[5] Lewin L. The electrical constants of a material loaded with spherical particles. *Proc. Inst. Electr. Eng.*, 94:65–68, 1946.

[6] Goldstein H., Poole C.P., and Safko J.L. *Classical Mechanics*. Addison-Wesley, 2002.

[7] Kittel C. *Quantum theory of solids*. Wiley & Sons, 1963.

[8] Kittel C. *Introduction to Solid State Physics*. John Wiley and Sons, 8 edition, 2005.

[9] Peierls R.E. *Quantum theory of solids*. Oxford, 1955.

[10] Merzbacher E. *Quantum mechanics*. John Wiley & Sons, 1998.

[11] Heitler W. *The quantum theory of radiation*. Oxford, 1954.

[12] Loudon R. Theory of the First-Order Raman Effect in Crystals. *Proc. R. Soc. Lond. A*, 275:218–232, 1963.

[13] Bir G.L. and Pikus G.E. Theory of the Deformation Potential for Semiconductors with a Complex Band Structure. *Soviet. Phys. Solid State*, 2:2039, 1961.

[14] Sakurai J.J. *Modern Quantum Mechanics*. Addison-Wesley, 1994.

[15] Martin R.M. Theory of the One-Phonon Resonance Raman Effect. *Phys. Rev. B*, 4(10):3676, November 1971.

[16] Martin R.M and Damen T.C. Breakdown of Selection Rules in Resonance Raman Scattering. *Phys. Rev. Lett.*, 26(2):86, January 1971.

[17] Falicov L.M. *Group theory and its physical applications*. University of Chicago Press, 1966.

[18] Loudon R. The Raman Effect in Crystals. *Adv. Phys.*, 50(7):813–864, 2001.

[19] Stevens T.E. *Ultrafast dynamics of low energy elementary excitations in semiconductors*. PhD thesis, University of Michigan, 2000.

[20] Hayes W. and Loudon R. *Scattering of light by crystals*. Dover Pubblications, 1978.

[21] Damen T.C., Porto S.P.S., and Tell B. Raman Effect in Zinc Oxide. *Phys. Rev.*, 142(2):570, February 1966.

[22] Landau L.D. and Lifshitz E.M. *Statistical Physics*. Oxford:Pergamon, 1969.

[23] Levenson M.D. Coherent Raman Spectroscopy. *Physics Today*, May 1977.

[24] Yan Y.-X., Gamble E.B., and Nelson K.A. Impulsive stimulated scattering: General importance in femtosecond laser pulse interactions with matter, and spectroscopic applications. *J. Chem. Phys.*, 83(11):5391, December 1985.

[25] Garrett G.A. *Femtosecond Pulsed Laser Excitation of Coherent and Squeezed Phonon Fields*. PhD thesis, The University of Michigan, 2001.

[26] Born M. and Wolf E. *Principles of Optics: Electromagnetic Theory of Propagation, Interference and Diffraction of Light*. Cambridge University Press, 1999.

[27] Liu Y., Frenkel A., Garrett G.A., Whitaker J.F., Fahy S., Uher C., and Merlin R. Impulsive Light Scattering by Coherent Phonons in $LaAl_3$: Disorder and Boundary Effects. *Phys. Rev. Lett.*, 75(2):334, July 1995.

[28] Garrett G.A., Albrecht T.F., Whitaker J.F., and Merlin R. Coherent THz Phonon Driven by Light Pulses and the Sb problem: What is the Mechanism? *Phys. Rev. Lett.*, 77(17):3661, October 1996.

[29] Trigo M. *Ultrafast dynamics of folded acoustic phonons from semiconductor superlattices*. PhD thesis, University of Michigan, 2008.

[30] Aku-Leh C. *Superconducting gap excitations, acoustic and optical phonons probed with femtosecond time-resolved and Raman spectroscopy*. PhD thesis, University of Michigan, 2005.

[31] Cova S. and Longoni A. *An introduction to signals, noise and measurements*. John Wiley & Sons, Pavia, Italy, 1979.

[32] Newport Corporation, 1791 Deer Avenue, Irvine CA 92606, USA. *RS2000-48-8 Details and Specs*, 2011.

[33] Zappa F. and Zappa R. *Elettronica Digitale*. Progetto Leonardo, 2003.

[34] Horowitz P. and Hill W. *The Art of Electronics*. Cambridge University Press, Cambridge, UK, 2 edition, 1989.

[35] Muller R.S. and Kamins T.I. *Device electronics for integrated circuits*. Wiley, 1977.

[36] Thorlabs Inc., 435 Route 206 Newton, NJ 07860, USA. *FDS100 Silicon Photodiode*, 2011.

[37] Hobbs P.C.D. *Building electro-optical circuits: making it all work*. Wiley, 2 edition, 2009.

[38] Stanford Research System, 1290-D Reamwood Ave, Sunnyvale, CA 94089. *DSP Lock-in amplifier: model SR830*, 1999.

[39] Mendaš I. and Vujković Cvijin P. Waveform of the Amplitude Modulated Laser Light by Means of a Mechanical Chopper. *Appl. Phys. B*, 32:119–122, 1983.

[40] Pfeifer T., Kütt W., and Kurz H. Generation and Detection of Coherent Optical Phonons in Germanium. *Phys. Rev. Lett.*, 69(22):3248, November 1992.

[41] Kaplan W. *Advanced Calculus*. Addison-Wesley, 4 edition, 1952.

[42] Dekorsy T., Pfeifer T., Kütt W., and Kurz H. Subpicosecond carrier transport in GaAs surface-space-charge fields. *Phys. Rev. B*, 47(7):3842, February 1993.

[43] Cho G.C., Kutt W., and Kurz H. Subpicosecond Time-Resolved Coherent-Phonon Oscillations in GaAs. *Phys. Rev. Lett.*, 65(6):764, August 1990.

[44] Fork R.L., Martinez O.E., and Gordon J.P. Negative dispersion using pairs of prisms. *Opt. Lett.*, 9(5):150, May 1984.

[45] Treacy E.B. Optical Pulse Compression with Diffraction Gratings. *IEEE J. Quant. Electron.*, 9(QE-5):454, September 1969.

[46] Merlin R. Generating coherent THz phonons with light pulses. *Solid State Commun.*, 102:207–220, 1997.

[47] Shen Y.R. *The principles of nonlinear optics*. John Wiley & Sons, University of California, Berkeley, 1984.

[48] Diels J.C.M., Fontaine J.J., McMichael I.C., and Simoni F. Control and measurement of ultrashort pulse shapes (in amplitude and phase) with femtosecond accuracy. *Appl. Opt.*, 24(9):1270, May 1985.

[49] Boyd R.W. *Nonlinear optics*. Academic Press, 3 edition, 2009.

[50] Bhattacharya P. *Semiconductor Optoelectronic Devices*. Prentice Hall, 2 edition, 1997.

[51] Goppert-Mayer M. Über Elementarakte mit zwei Quantensprüngen. *Ann. Phys. (Leipz.)*, 9:273, 1931.

[52] Bechtel J.H. and Smith W.L. Two-photon absorption in semiconductors with picosecond laser pulses. *Phys. Rev. B*, 13(8):3515, April 1976.

[53] Hamamatsu Solid State Division, 360 Foothill Road, Bridgewater, NJ 08807. *GaAsP 5645 photodiode datasheet*, 2011.

[54] Sglux GmbH, Ostendstr 25, 12459 Berlin. *Mulitfunctional 2-Channel Amplifier Board*, 2011.

[55] Ranka J.K. and Gaeta A.L. Autocorrelation measurement of 6-fs pulses based on the two-photon-induced photocurrent in a GaAsP photodiode. *Opt. Lett.*, 22(17):1344, September 1997.

[56] Trebino R., Kenneth W.D., Fittinghoff D.N., Sweetser J.N., Krumbügel, and Richman B.A. Measuring ultrashort laser pulses in the time-frequency domain using frequency-resolved optical grating. *Rev. Sci. Intrum.*, 68(9):3277, September 1997.

[57] Altes R.A. Detection, estimation and classification with spectrograms. *J. Acoust. Soc. Am.*, 67:1232, 1980.

[58] Trebino R. *Frequency-Resolved Optical Gating: the Measurements of Ultrashort Laser Pulses*. Kluwer Academic Publishers, 2002.

[59] SWAMP OPTICS, LLC, 6300 Power Ferry Road Suite 600-345 Atlanta, GA 30339-2919. *www.swampoptics.com*, 2011.

[60] Landau L.D., Lifshitz E.M., and Pitaevskii L.P. *Electrodynamics of continuous media*. Elsevier, 2 edition, 1960.

[61] Born M. and Huang K. *Dynamic theory of crystal lattices*. Oxford University Press, 1954.

[62] Mills D. L. Burstein E. Polaritons: the electromagnetic modes of media. *Rep. Prog. Phys.*, 37:817, 1974.

[63] Ashcroft N. W. and Mermin N. D. *Solid State Physics*. Thomson Learning, 1976.

[64] Boohm D. and Pine D. A collecive Description of Collective Interactions: III. Coulomb Interactions in a Degenerate Electron Gas. *Phys. Rev.*, 92:609, 1953.

[65] Raether H. *Surface plasmons on smooth and rough surfaces and on gratings*. Springer-Verlag, 1986.

[66] Henry C. H. and Hopfield J. J. Raman scattering by polaritons. *Phys. Rev. Lett.*, 15(25):964, 1965.

[67] Davydov V. Yu., Subashiev A. V., Cheng T. S., Foxon C. T., Goncharuk I. N., Smirnov A. N., and Zolotareva R.V. Raman scattering by surface polaritons in cubic GaN epitaxial layers. *Solid State Commun.*, 104(7):397, 1997.

[68] Tinkham M. *Group Theory and Quantum Mechanics*. Dover Pubblications, 2003.

[69] Puech P., Carles R., and Fontaine C. Strain effects on optical phonons in $< 111 >$ GaAs layers analyzed by Raman scattering. *J Appl Phys*, 82(9):4493, November 1997.

[70] Barkhuijsen H., De Beer R., Van Bovée W.M.M.J., and Ormondt D. Retrieval of Frequencies, Amplitude, Damping Factors, and Phases from Time-Domain Signals Using a Linear Least-Squares Procedures. *J. Magn. Res.*, 61:465, 1985.

[71] Kütt W.A., Albrecht W., and Kurz H. Generation of Coherent Phonons in Condensed Media. *IEEE J. Quantum Electron.*, 28(10):2434, October 1992.

[72] Dekorsy T., Cho G.C., and Kurz H. *Coherent Phonos in Condensed Media*, volume 76 of *Topics in Applied Physics*. Springer, 2000.

[73] Cho G.C., Dekorsy T., Bakker H.J., Hövel R., and Kurz H. Generation and Relaxation of Coherent Majority Plasmons. *Phys. Rev. Lett.*, 77(19):4062, November 1996.

[74] Pfeifer T., Dekorsy T., Kütt W., and Kurz H. Generation Mechanism for Coherent LO Phonons in Surface-Space-Charge Fields of III-V Compounds. *Appl. Phys. A*, 55:482–488, August 1992.

[75] Neamen D. *Semiconductor physics and devices: basic principles.* Chicago Irwin, 2 edition, 1997.

[76] Kepińka M., Novak M., Kovalyuk Z., and Murri R. Temperature Dependence of Optical Energy Gap of Gallium Selenide. *J. Wide Bandgap Mater.*, 8(3–4):251, 2001.

[77] Yoshida H., Nakashima S., and Mitsuitshi A. Phonon Raman Spectra of Layer Compound GaSe. *Phys. Stat. Sol. (b)*, 59:655, 1073.

[78] Dresselhaus M.S., Dresselhaus G., and Jorio A. *Group thepry: application to the physics of condensed matter.* Springer, 2008.

[79] Jandl S. and Brebner J.L. Lattice dynamics of GaSe. *Phys. Rev. B*, 13(2):686, January 1976.

[80] Mercier A. and Voitchovsky J.P. Raman scattering from GaS_xSe_{1-x}. *Solid State Commun.*, 14:757–762, 2011.

[81] Irwin J.C., Hoff R.M., Clyman B.P., and Bromley R.A. Long wavelength lattice vibrations in GaS and GaSe. *Solid State Commun.*, 13:1531–1536, 1963.

[82] Hoff R.M. and Irwin J.C. Resonant Raman scattering in GaSe. *Phys Rev B*, 10(8):3464–3470, 1974.

[83] Faust W.L. and Henry C.H. Mixing of visible and near-resonance infrared light in GaP. *Phys. Rev. Lett.*, 17(25):1265, December 1966.

[84] Zekeng S., Prevot B., and Schwab C. *Phys. Status Sol. (b)*, 150:65, 1988.

[85] Johnston W.P. and Kaminow I.P. *Phys. Rev.*, 188:1209, 1969.

[86] Brafman S. and Mitra S.S. Raman Effect in Wurtzite- and Zinc-blende-Type ZnS Single Crystals. *Phys. Rev.*, 11(3):931, July 1968.

[87] Thomas D.G. *II-VI Semiconducting comounds.* W. A. Benjamin, 1967.

[88] Flytzanis Chr. Electro-Optic Coefficients in II-V Compounds. *Phys. Rev. Lett.*, 23(23):1336, December 1969.

[89] Frank I. *Vasilov-Cherenkov radiation.* Nauka, Moscow, 1988.

[90] Afasaniev G.N. and Kartavenko V.G. Radiation of a point charge uniformly moving in a dielectric medium. *J. Phys. D: Appl. Phys.*, 31:2760–2776, 1998.

[91] Kleiman D.A. and Auston D.H. Theory of Electrooptic Shock Radiation in Nonlinear Optical Media. *IEEE J Quantum Electron.*, QE-20(8):964, 1984.

[92] Zrelov V.P. *Chrenkov Radiation in High-Energy Physics.* Israel Program for Scientific Translations, Israel, 1970.

[93] Stevens T.E., Wahlstrand J.K., Kuhl J., and Merlin R. Cherenkov Radiation at Speeds Below the Light Threshold: Phonon-Assisted Phase Matching. *Science*, 291:627, 2001.

[94] Wahlstrand J.K. *Impulsive generation of coherent hybrid modes by light pulses.* PhD thesis, University of Michigan, 2005.

[95] Afanasiev G.N., Kartavenko V.G., and Magar E.N. Vasilov-Cherenkov radiation in dispersive medium. *Phys. B*, 113:95, 2011.

[96] Ekimov A.I., Efros Al. L., and Onushchenko A.A. Quantum size effect in semiconductor microcrystals. *Solid State Commun.*, 56:921, 1985.

[97] Norris D.J. and Bawendi M.G. Measurement and assignment of the size-dependent optical spectrum in CdSe quantum dots. *Phys. Rev. B*, 53(24):16338, 1986.

[98] Norris D.J., Efros Al. L., Rosen M., and Bawendi M.G. Size dependence of exciton fine structure in CdSe quantum dots. *Phys. Rev. B*, 53(24):16347, 1996.

[99] Plotnichenko V.G., Mityagin Yu.A., and Vodop'ynov L.K. Investigation of fundamental vibrations in CdSe by Raman scattering and infrared reflection methods. *Sov. Phys. Solid State*, 19(9):1584, September 1977.

[100] Arora A.K. and Ramdas A.K. Resonance Raman scattering from defects in CdS. *Phys. Rev. B*, 35(9):4345, March 1987.

[101] Hermann C. and Yu P.Y. Role of elastic exciton-defect scattering in resonant Raman and resonant Brillouin scattering in CdSe. *Phys. Rev. B*, 21(8):3675, April 1980.

[102] Bube R.H. Temperature Dependence of the Width of the Band Gap in Several Photoconductors. *Phys. Rev.*, 98(2):431, April 1955.

[103] Leite R.C.C. and Porto S.P.S. Enhancement of Raman cross section in CdS due to resonant absorption. *Phys. Rev. Lett.*, 17(1), July 1966.

[104] Leite R.C.C., Scott J.F., and Damen T.C. Multiple-phonon-resonance Raman effect in CdS. *Phys. Rev. Lett.*, 22(15):780, April 1969.

[105] Klein M.V and Porto S.P.S. Multiple-phonon-resonance Raman effect in CdS. *Phys. Rev. Lett.*, 22(15):782, 1969.

[106] Palil E.D. *Handbook of Optical Constants of Solids*. Academic Press, Orlando, Florida, 1985.

[107] Garrett G.A., Rojo A.G., Sood A.K., Whitaker J.F., and Merlin R. Vacuum Squeezing of Solids: Macroscopic Quantum States Driven by Light Pulses. *Science*, 275:1638, March 1997.

[108] Huang K. *Statistical Mechanics*. John Wiley & Sons, 1963.

[109] Bassani F. and Pastori Parravicini G. *Electronic States and Optical Transitions in Solids*. Pergamon Press, 1975.

[110] Neumann T., Borstel G., Scharfschwerdt C., and Neumann M. Electronic structure of $KNbO_3$ and $KTaO_3$. *Phys. Rev. B*, 46(1):623, November 1992.

[111] Matsubara E., Inoue K., and Hanamura E. Dynamic Symmetry Breaking Induced by Ultrashort Laser Pulses in $KTaO_3$. *J. Phys. Soc. Jpn.*, 2(75):24712, February 2006.

[112] Pendry J.B. and Smith D.R. Reversing light with negative refraction. *Phys. Today*, 57:37–43, 2004.

[113] Wegener M. Soukolis C.M., Linden S. Negative refractive index at optical wavelengths. *Science*, 315:47–49, 2007.

[114] Gartstein Y.N. Agranovich V.M. Spatial dispersion and negative refraction of light. *Physics-Usphekhi*, 49:1029–1044, 2006.

[115] Shalaev V.M. Optical negative-index metamaterials. *Nat. Photonics*, 1:41–48, 2007.

[116] Merlin R. Metamaterials and the Landau-Lifshitz permeability argument: Large permittiviy begets high-frequency magnetism. *PNAS*, 106(6):1693–1698, February 2009.

[117] Pendry J.B., Holden A.J., Robbins D.J., and Steward W.J. Magnetism from conductors and enhanced nonlinear phenomena. *IEEE Trans Microwave Theory Tech*, 47:2075–2084, 1999.

[118] Holloway C.L., Kuester E.F., Baker-Jarvis J., and Kabos P. A double negative (DNG) composite medium composed of magnetodielectric spherical particles embedded in a matrix. *IEEE Trans Antennas Propag*, 51:2596, 2003.

[119] Huang C.K., Povinelli M.L., and Joannopoulos J.D. Negative effective permeability in polaritonic photonic crystals. *Appl. Phys. Lett.*, 85:543, 2004.

[120] Mojahedi M. Wheeler M.S., Aitchison J.S. Three-dimensional array of dielectric spheres with an isotropic negative permeability at infrared frequencies. *Phys Rev B*, 72:193103, 2005.

[121] Zhao Q, Kang L, Du B, Zhao H, Xie Q, Huang X, Li B, Zhou J, and Li L. Experimental demonstration of isotropic negative permeability in a three-dimensional dielectric composite. *Phys Rev Lett*, 101:027402, 2008.

[122] Brandt E.H. Levitation in Physics. 243(4889):349–355, 1989.

[123] Geim A.K., Simon M.D., Boamfa M.I., and Heflinger L.O. Magnet levitation at your fingertips. *Nature*, 400:323, July 1999.

[124] Jones T.B. A necessary condition for magnetic levitation. *J. Appl. Phys.*, 50(7):5057, July 1979.

[125] Stratton J.A. *Electromagnetic theory*. McGraw Hill, 1941.

[126] Abramovitz M. and Stegun I.A. *Handbook of mathematical functions*. Dover Pubblications, 1972.

[127] Mie G. Beiträge zur Optik trüber Medien, speziell kolloidaler Metallösungen. *Ann. Phys.*, 330:377–445, 1908.

[128] Jackson J.D. *Classical Electrodynamics*. John Wiley & Sons, 3 edition, 1999.

[129] Smythe W.R. *Static and Dynamic Electricity*. McGraw-Hill Book Company, 2 edition, 1950.

[130] Maguer SL Bourreau D, Peden A. A quasi-optical free-space measurement setup without time-domain gating for material characterization in the w-band. *IEEE Transaction on Instrumentation and Measurement*, 55(6):613–619, December 2006.

[131] Goldsmith P.F. Quasi-Optical techniques. *IEEE Proceedings*, 80(11):1729, November 1992.

[132] Tuovinen J., Hirvonen T.M., and Räisänen A.V. Near-field Analysis of a Thick Lens and Horn Combination: Theory and Measurements. *IEEE Trans. Antennas Propag.*, 40(6):613–619, June 1992.

[133] Baker-Jarvis J., Vanzura E.J., and Kissick W.A. Improved Technique for Determining Complex Permittivity with the Transmission/Reflection Method. *IEEE Transaction on Microwave Theory and Tecniques*, 38(8):1096–1103, August 1990.

[134] Pozar D.M. *Microwave Engineering.* John Wiley & Sons, 3 edition, 2005.

[135] Takahashi J. Parametric amplification of Raman-inactive lattice osciallations induced by two-color cross-beam excitation. *Optics Express*, 14(7):2831, April 2006.

[136] Matsubara E., Inoue K., and Hanamura E. Violation of Raman selection rules induced by two femtosecond laser pulses in $KTaO_3$. *Phys. Rev. B*, 72:134101, 2005.